IN-SITU PERFORMANCE OF SU-FREI BRIDGE BEARINGS

IN-SITU PERFORMANCE OF SU-FREI BRIDGE BEARINGS

Zachary van Galen

B. Eng. Mgmt., EIT

001304061

Masters of Applied Science Thesis

School of Graduate Studies

McMaster University

© Copyright by Zachary van Galen, April 5, 2023

TITLE: IN-SITU PERFORMANCE OF SU-FREI BRIDGE BEARINGS

AUTHOR: Zachary R. van Galen

SUPERVISOR: Dr. Michael J. Tait

NUMBER OF PAGES: 120 Pages (i-xii, 1-108)

Lay Abstract

Concrete and steel bridges deform due to temperature changes, traffic motion, and other factors. To allow these deformations without inducing large forces or damage, bearings are employed between the bridge deck and supports.

One type of bearing consists of alternating layers of rubber and steel: steel strengthens the bearing, while the rubber provides lateral and rotational flexibility. A relatively new type of bearing has been developed and tested that replaces the steel layers with carbon fibre. Recently, several of these new SU-FREI bearings have been installed on actual highway bridges.

The focus of this thesis is on the performance of SU-FREI installed as bridge bearings. The goal was to observe their performance, identify any unexpected behavior, and create recommendations for future consideration whenever SU-FREI are to be used as bridge bearings. Generally, it was found that their performance is satisfactory provided they are designed and used appropriately.

Abstract

Stable Unbonded Fibre Reinforced Elastomeric Isolators (SU-FREI) have been investigated extensively for seismic applications, with over 20 years of literature supporting their use in isolation of structures as an alternative to conventional Steel Reinforced Elastomeric Isolators (SREI). Preliminary investigations have been conducted into their potential use as bridge bearings, where they could provide an alternative to unreinforced and steel reinforced elastomeric bearings. SU-FREI offer a number of potential advantages in this application relative to SREI, including compactness due to thinner reinforcement layers, ease of installation, rotational tolerances, and ease of manufacture. Recently, SU-FREI have been installed under certain highway bridges along the 407 ETR where the previous unreinforced elastomeric bearings had experienced failure. Monitoring has been conducted by Associated Engineering for the 407 ETR Corporation.

Data was collected from this monitoring program and field visits have been conducted to observe the condition of the bearings. The original design process used for the SU-FREI bearings has also been reviewed. The monitoring data was compared against design calculations, and the behavior of the SU-FREI analysed to determine whether they meet performance expectations and are suitable for further use as bridge bearings.

It was found that some SU-FREI had experienced degradation, including the appearance of an unidentified liquid. The causes of deterioration were investigated and postulated to be primarily related to design limitations imposed by the geometry of the bridges, original design calculation assumptions, and installation issues. Where these factors were not present, the SU-FREI bearings were found to have experienced little to no deterioration. Furthermore, it was determined through comparative design calculations that the FREI outperformed equivalent SREI with regard to rotational capacity.

Recommendations have been developed for future deployment of SU-FREI as bridge bearings. Based on the results of initial deployments, larger-scale employment of SU-FREI in this application should be considered.

Acknowledgements

Credit is given to Dr. Michael Tait for his consistent advice and guidance regarding how to proceed through the research process, for consistent help in the development of this report, for highlighting this area of research in the first place, and for the great deal of work he did to make this project possible before I came on board.

I would also like to thank McMaster University Faculty of Engineering, the National Science and Engineering Research Council, and the Ontario Graduate Scholarships program, without whose financial and institutional support this research could not take place.

In addition, the Ontario 407 ETR Corporation and Associated Engineering (with support from BDI inc.) deserve credit for provision of the real-world bearing data upon which this research project is based. Special thanks are given to Mark Torrie and Daniel MacDonald-Lockheart, who have been involved with this project since the beginning.

Thanks go out to my professors and fellow graduate students, many of whom have provided advice, guidance, and innumerable bits of help and support along the way.

Finally, special thanks to my mom and dad, for their emotional support and for patiently listening to far more rants about the performance of rubber-fibre bearings than any untrained individual should ever be subjected to.

Table of Contents

Lay Abstract iii
Abstract iv
Acknowledgements v
Table of Contents vi
Abbreviations and Symbols ix
1 Introduction 1
1.1 Overview of Bridge Bearings 1
1.1.1 General information 1
1.1.2 Non-elastomeric bearings 1
1.1.3 Elastomeric bearings 7
1.2 Development of Fibre Reinforced Elastomeric Isolators 8
1.3 Analysis of FREI 12
1.4 FREI as Bridge Bearings 14
1.5 Research Objectives 15
2 Bearing Installations 16
2.1 General design procedure 16
2.2 German Mills Creek Bridge 28
2.2.1 Site situation 28
2.2.2 Bearing design 29
2.2.3 Notes on Installation 31
2.3 Steeles Avenue Bridge 32
2.3.1 Site situation 32
2.3.2 Bearing design 34
2.3.3 Notes on Installation 36
3 Field observations 38
3.1 German Mills Creek Bridge 38
3.1.1 Site visits 38
3.1.2 Discussion 42
3.2 Steeles Avenue Bridge 44
3.2.1 Inspection Reports 44

3.2.2 Site visit 47
3.2.3 Discussion 52
3.3 Analysis 54
3.3.1 Rotational Capacity 54
3.3.2 Vertical Compression 58
3.3.3 Unidentified liquid 61
4 In-Situ Data 65
4.1 Monitoring System 65
4.2 Data Processing 67
4.2.1 General 67
4.2.2 Trend Data 68
4.2.3 Continuous data 70
4.3 Analysis 75
4.3.1 Continuous Data 75
4.3.2 Trend Data 78
4.3.3 Overall 87
5 Conclusions & Recommendations 90
5.1 Summary 90
5.2 Recommendations 92
5.3 Future Work 93
6 References 94
Appendix A 98
Appendix B 101
Appendix C 103

Figure 1: Steel plate bearing; depiction adapted from Ramberger, 2002. 2
Figure 2: Pot bearing; depiction adapted from Ramberger, 2002 3
Figure 3: Spherical bearing; depiction adapted from Ramberger, 2002 4
Figure 4: Leaf and link bearing; depiction adapted from Ramberger, 2002. 5
Figure 5: Disc bearing; depiction adapted from Ramberger, 2002 6
Figure 6: Double friction pendulum bearing; depiction adapted from Bao et al., 2017 7
Figure 7: Rollover behavior of SU-FREI bearing 12
Figure 8: Stress distribution in reinforcement when the bearing is under compression 23
Figure 9: Stress distribution in reinforcement when the bearing is under bending 24
Figure 10: Aerial view of German Mills creek bearing site; maps data: Google, Image ©2023 Maxar Technologies 29
Figure 11: Aerial view of Steeles Avenue bearing site; Maps Data: Google, Image Landsat/Copernicus 33
Figure 12: Cross-sectional view of Steeles Avenue bridge girder, including bearing positions ... 33
Figure 13: Unreinforced, failed Steeles Avenue bridge bearing 34
Figure 14: Damaged bearing at German Mills. Intersection point of white lines illustrates a change in inclination of the bearing of approximately two degrees, forming a 'bump' directly under the damaged region of the bearing. 39
Figure 15: Location of bearings at German Mills Creek site; maps data: Google, Image Landsat/Copernicus 39
Figure 16: Bearing 1 at German Mills Creek site with location of liquid recovery marked 40
Figure 17: Unidentified black liquid staining tip of ruler 41
Figure 18: Undamaged bearing at German Mills Creek; no liquid visible 41
Figure 19: Undamaged bearing at German Mills Creek; slight bulging which is not indicative of damage 42
Figure 20: Bearing layout at Steeles Avenue as shown in first inspection report ("407W-to-427S Bridge", 2020a) 44
Figure 21: Bearing J2-W with unidentified liquid over the majority of bearing face 49
Figure 22: Bearing J3-W splitting behavior occurring along line of previous delamination 50
Figure 23: Limited delamination observed at bearing J1-W 51
Figure 24: Bulging but undamaged bearing J3-E 52
Figure 25: Sensor locations for Steeles Avenue site bearings (D. MacDonald-Lockhart, Personal Communication, Sept. 15, 2021) 66
Figure 26: Filter functions – low-pass to capture temperature motions (left) and band pass to capture traffic motions (right) 71
Figure 27: Fast Fourier Transform of rotations at bearing J2-E 72
Figure 28: Fast Fourier Transform of vertical displacements at bearing J2-E 72
Figure 29: Fast Fourier Transform of horizontal displacements at bearing J2-E 73
Figure 30: Power spectral density of rotations at bearing J2-E 73
Figure 31: Power spectral density of vertical displacements at bearing J2-E 74

Figure 32: Power spectral density of horizontal displacements at bearing J2-E 74
Figure 33: Horizontal displacement at bearing J2-E on October 10, 2019 – total, temperature, and traffic related motions 75
Figure 34: Vertical displacement at bearing J2-E on October 10, 2019 – total, temperature, and traffic related motions 76
Figure 35: Rotation at bearing J2-E on October 10, 2019 – total, temperature, and traffic related motions 76
Figure 36: Horizontal displacement at bearing J1-W from August 29, 2019 to February 28, 2020 80
Figure 37: Vertical displacement at bearing J1-W from August 29, 2019 to February 28, 2020 . 81
Figure 38: Average rotation at bearing J1-W from August 29, 2019 to February 28, 2020 81
Figure 39: Horizontal displacement at bearing J2-W from August 29, 2019 to February 28, 2020 82
Figure 40: Vertical displacement at bearing J3-W from August 29, 2019 to February 28, 2020 . 83
Figure 41: Average Rotation at bearing J3-W from August 29, 2019 to February 28, 2020 83
Figure 42: Horizontal displacement at bearing J2-E from August 28, 2019 to August 28, 2020.. 85
Figure 43: PSD analysis of horizontal displacement at bearing J2-E from August 28, 2019 to August 28, 2020 86

Table 1: Key loading values for bearings at German Mills Creek site 30
Table 2: Key material properties for bearings at German Mills Creek site 30
Table 3: Key design parameters for bearings at German Mills Creek site 31
Table 4: Key loading values for bearings at Steeles Avenue site 35
Table 5: Key material properties for bearings at Steeles Avenue site 35
Table 6: Key design parameters for bearings at Steeles Avenue site 36
Table 7: Bearing identifiers at Steeles Avenue site 37
Table 8: Summary of Steeles Avenue site bearing conditions at initial and final inspection reports 47
Table 9: Record of unidentified liquid in inspection reports contrasted with field observations 48
Table 10: Key parameters for alternative steel bearing design for German Mills Creek site 55
Table 11: Comparison of key design checks for U-FREI and equivalent SREI bearings designed for German Mills creek site 57
Table 12: Comparison of key design criteria between U-FREI under different loading cases for Steeles Avenue site 59
Table 13: Sensor locations for Steeles Avenue site bearings (D. MacDonald-Lockhart, Personal Communication, Sept. 15, 2021) 66
Table 14: Bearing performance under various loading cases for key design checks. 89

Abbreviations and Symbols

CHBDC: the Canadian Highway Bridge Design Code

CSA: Canadian Standards Association

FFT: Fast Fourier Transform

FREI: Fibre Reinforced Elastomeric Isolator

LVDT: Linear Variable Differential Transformer

PEER: Pacific Earthquake Engineering Research Center

PSD: Power Spectral Density

SLS: Serviceability Limit State

SREI: Steel Reinforced Elastomeric Isolator

SU-FREI: Stable Unbonded Fibre Reinforced Elastomeric Isolator

U-FREI: Unbonded Fibre Reinforced Elastomeric Isolator

ULS: Ultimate Limit State

A = area

a = plan length of bearing (parallel to axis of rotation)

b = plan width of bearing (perpendicular to axis of rotation)

e = coefficient related to bearing geometry; 0, 1, or 2.

E_0 = hardness constant (2.52 MPa for bearings under consideration)

E_b = bending modulus (of internal layer)

E_c = compression modulus (of bearing)

E_f = elastic modulus of the fibre layers

E_α = hardness constant (1090 MPa for bearings under consideration)

G = shear modulus (of elastomer)

j = dimensionless parameter used in calculation of γ_r

k = hardness constant (0.64 for bearings under consideration)

K_{bulk} = bulk modulus (of elastomer)

$K_{e=x}$ = effective bulk modulus of the bearing where the coefficient e has a value of x

k_h = horizontal stiffness (of bearing)

kv = vertical stiffness (of bearing)

m = dimensionless parameter used in calculation of γ_r

n = number of internal elastomer layers in bearing

p = ratio of plan length over plan width

p_c = dimensionless parameter; relevant to approximate E_c calculation.

P_r = dimensionless parameter used in calculation of γ_r

p_s = dimensionless parameter; relevant to approximate γ_c calculation

S = shape factor of bearing

S_{xx} = stress in reinforcing layer

T = total bearing thickness

t_c = total thickness of 'cover' rubber layers

t_{cl} = thickness of an individual 'cover' rubber layer

t_f = total thickness of fibre layers

t_{fl} = thickness of an individual fibre layer

t_i = total thickness of 'internal' rubber layers

t_{il} = thickness of an individual 'internal' rubber layer

t_r = total thickness of rubber (elastomer) layers

t_{sl} = thickness of an individual steel layer

α = dimensionless parameter; relevant to E_c calculation.

B = dimensionless parameter; relevant to E_c calculation.

Γ_c = shear strain due to compression

γ_d = shear strain due to horizontal displacement

γ_r = shear strain due to rotation

Δ_c = deflection due to SLS compression in the vertical direction

ε_c = compressive strain

ζ_n = dimensionless parameter used in calculation of γ_c

ζ_m = dimensionless parameter used in calculation of E_c for SREI

θ = rotation imposed upon the bearing

θ_{all} = allowable rotation that may be imposed upon the bearing

λ = dimensionless parameter; relevant to E_c calculation.

Λ_2 = dimensionless parameter; relevant to γ_c calculation.

Λ_t = dimensionless parameter used in calculation of γ_r

σ_{SLSD} = vertical pressure at serviceability limit state due to dead load

σ_{SLST} = total vertical pressure at serviceability limit state

σ_{ULSD} = vertical pressure at ultimate limit state due to dead load

σ_{ULST} = total vertical pressure at ultimate limit state

1 Introduction

1.1 Overview of Bridge Bearings

1.1.1 General information

Bridge bearings are devices that are used to introduce flexibility between the deck of a bridge and its supports (e.g. piers and abutments). The relatively flexible bearings prevent large stresses within the deck and supports from developing by accommodating deformations that occur from various loads. These movements may include deck expansion or contraction due to temperature, traffic-induced vibrations, and other loading-related motions. In the past, when bridges were primarily made out of stone and timber, the high mass of stone structures and comparative flexibility of timber made bearings unnecessary – but with the advent of steel and concrete based bridge construction, they became vital (Ramberger, 2002). Modern bridges utilize a wide variety of bearing designs, including steel, pot, disc, spherical, leaf and link, and elastomeric bearings. An ideal bearing should be able to accommodate both displacements and rotations and be resistant to weathering and degradation over the life of the structure.

1.1.2 Non-elastomeric bearings

Steel bearings consist of a flat steel plate resting atop a curving one, such that it can tilt freely (Ramberger, 2002). This type of bearing has been in use since the start of the 20th century, and is only able to accommodate rotations: due to frictional forces, any horizontal displacements will result in 'grinding' of the plates against one another, which can result in damage. Furthermore, due to the small contact area between the flat and curving plate (only as large an area as is

created by elastic deformation of the plates under contact stresses), the plates must be thicker than those in other bearing types in order to distribute the force concentrations in the contact area. An example of this type of bearing is shown in Figure 1 (Ramberger, 2002).

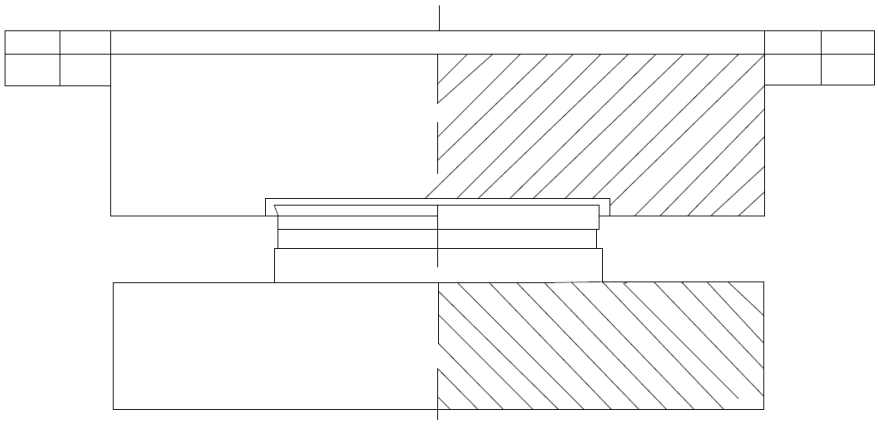

Figure 1: Steel plate bearing; depiction adapted from Ramberger, 2002.

The development of Pot bearings goes back to the 1950s. These bearings consist of a steel pot filled with a rubber disc and capped off with a steel lid. Under large vertical loads the elastomer tends to act like a liquid, allowing the steel lid to smoothly rotate – but like steel bearings, standard pot bearings cannot accommodate horizontal displacements. However, a sliding apparatus may be added to a pot bearing to allow for horizontal displacement, which would consist of a grease-lubricated low-friction disc (often made of polytetrafluoroethylene) and a steel plate over top of the primary bearing apparatus. One major advantage of pot bearings is their high vertical stiffness, which is a result of the confined elastomer being nearly incompressible. An example of the standard type of pot bearing is shown in Figure 2 (Ramberger, 2002).

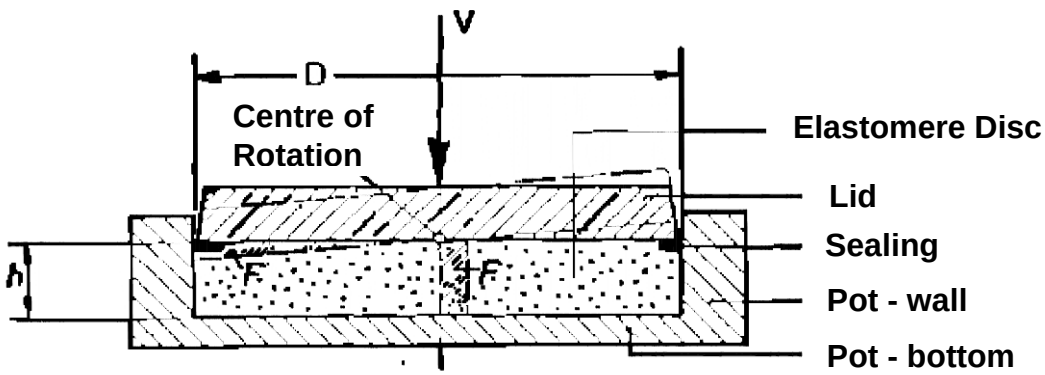

Figure 2: Pot bearing; depiction adapted from Ramberger, 2002

Standard spherical bearings consist of a large steel piece with a flat top and spherically curved bottom located within a steel pan of equal curvature, and a sliding plate above, with each steel element separated by a low-friction sliding layer. Since they include both sliding and rotating elements, they can accommodate both horizontal displacements and rotations – however, the large surface area over which the sliding occurs may cause the bearings to impose reaction moments in response to rotations. An example of this type of bearing is shown in Figure 3 (Ramberger, 2002).

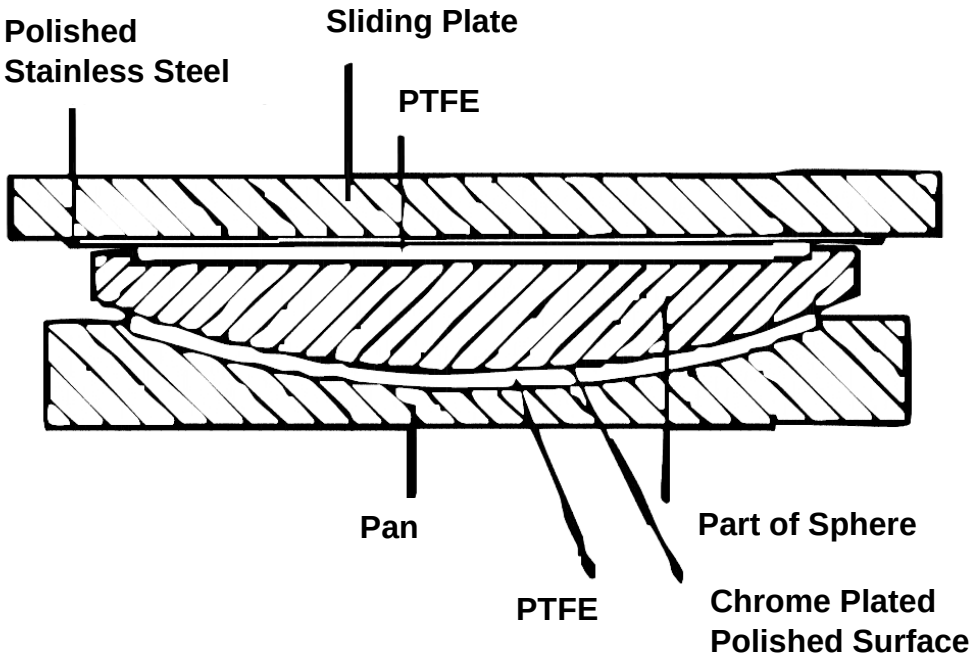

Figure 3: Spherical bearing; depiction adapted from Ramberger, 2002

Leaf and link bearings are specialized designs that are employed where it may be necessary for the bearing to transfer tension forces: all previously discussed designs are only able to transfer compression. A leaf bearing consists of an upper and lower plate, each with a number of 'leafs' connected by a pin, allowing rotation in a single direction. Link bearings are similar, but with pendulums introduced between the top and bottom leafs to allow for horizontal displacements as well as rotations in one direction. There are ways to extend this idea to allow omnidirectional rotation and displacement, but these are not commonly used. An example of this type of bearing is shown in Figure 4 (Ramberger, 2002).

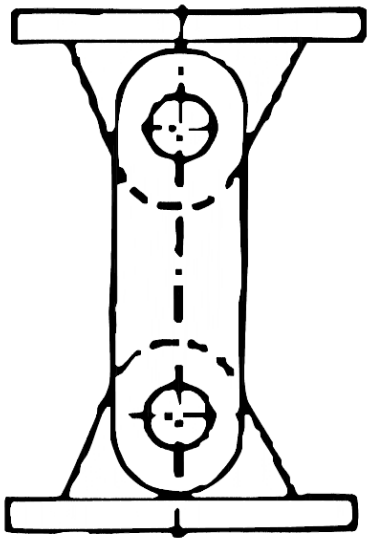

Figure 4: Leaf and link bearing; depiction adapted from Ramberger, 2002.

Disc bearings first came into use in the 1960s, and like pot bearings, use an elastomeric disc to transfer the vertical loads. Unlike a pot bearing, the elastomer in a disc bearing is not confined. They accommodate rotations in a similar manner to pot bearings, while transferring vertical forces with the help of a shear-restriction device. In this bearing type, rotations can cause the load axis to shift away from the center of the bearing, which must be considered. An example of this type of bearing is shown in Figure 5 (Ramberger, 2002).

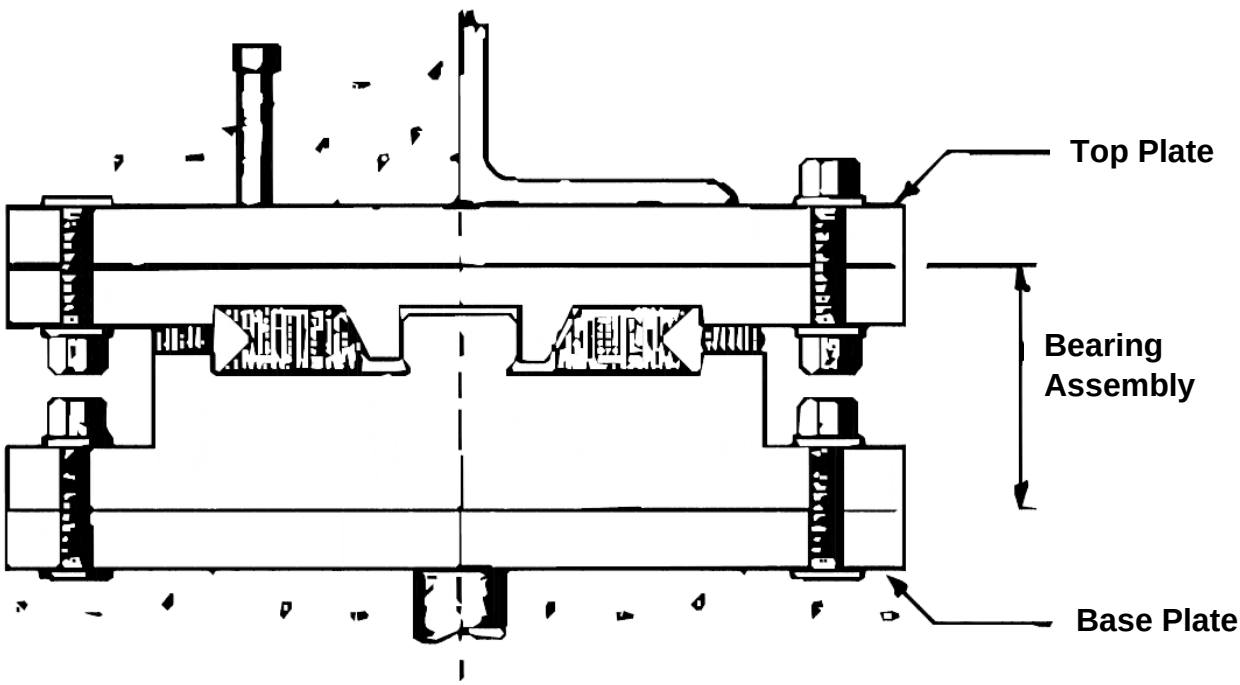

Figure 5: Disc bearing; depiction adapted from Ramberger, 2002

Friction pendulum bearings, also called pendulum sliding bearings, involve one or two concave plates with one or two sliding elements between them (Bao et al., 2017). These sliding elements may be stacked vertically, and are configured in such a way as to allow the top sliding element to rotate relative to the bottom one. These bearings are capable of accommodating horizontal displacement along one or more axes, as well as rotations. In order to prevent the slider from falling off the plates under large displacements, the plates are typically surrounded by a raised rim. A friction pendulum bearing with two concave plates and two sliding elements is referred to as an articulated double pendulum sliding bearing – articulated, referring to the two separate sliding pieces, and double pendulum, referring to the two concave surfaces. An example of this type of bearing is shown in Figure 6. (Bao et al., 2017). It is also possible to use a three-element

single pendulum bearing as the sliding element within a larger double pendulum bearing, with appropriately shaped concave plates. This is referred to as a triple pendulum bearing.

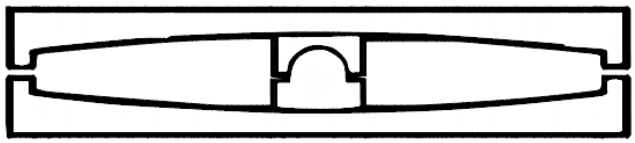

Figure 6: Double friction pendulum bearing; depiction adapted from Bao et al., 2017

1.1.3 Elastomeric bearings

In concept, elastomeric bearings are the least mechanically complex form of bearing: they consist of a single block of elastomer, typically circular or rectangular (Ramberger, 2002) in plan. These bearings are flexible, allowing for both horizontal displacements and rotations. Because the elastomer is relatively thick and unconfined, under vertical loads the bearing tends to 'bulge', leading to large vertical displacements.

To limit vertical displacements and permit higher vertical loading, elastomeric bearings can be reinforced with steel plates, which confine the elastomer and limit its bulging. This is particularly important when the bearing is relatively thick – however, for thinner bearings, unreinforced designs are still in widespread use (Goodco Z-tech, 2010). The most common method of reinforcing elastomeric bearings is by using thin steel plates – a technology also in widespread use in elastomeric isolators for base isolation of structures (Foster, 2011). However, there are potential drawbacks to such an approach. If a steel reinforced bearing becomes damaged, or if a defect in construction exposes the steel reinforcement, it can become vulnerable to corrosion.

As a result, steel reinforcing plates in this type of bearing must be entirely covered by the elastomer ("407W-to-427S Bridge", 2020a).

The Canadian Highway Bridge Design Code (CHBDC) 2019 provides requirements for the design of elastomeric bearings. Current code provisions are written considering the use of unreinforced or steel-reinforced elastomeric bearings, and the requirements and equations are reflective of this. For example, specific guidance is given for thickness of steel plates to be used, but none for any alternate reinforcing material. However, the code does allow for alternate reinforcing material to be used. The requirement is laid out in clause 4.10.10.2 which states, in part: "Reinforcement whose properties are adversely affected when exposed to water, cold or hot temperatures or other environmental effects, shall not be permitted". As carbon fiber does not corrode and has relatively low sensitivity to temperature, it meets this requirement. While some clauses are written considering only steel-reinforced bearings, others – including clauses 4.10.10.3, 11.6.6.2, and 11.6.6.3 – remain applicable.

1.2 Development of Fibre Reinforced Elastomeric Isolators

One of the first dedicated studies to examine if it was possible to replace traditional steel reinforcing plates with carbon fibre layers in elastomeric isolators was conducted by Kelly (1999) at UC Berkeley. Kelly was one of the earliest researchers to establish the possibility of using fibre reinforced elastomeric isolators (FREI) that could provide equivalent performance to steel reinforced elastomeric isolators (SREI). This work was expanded on in a Pacific Earthquake Engineering Research Center (PEER) report by Tsai and Kelly (2001). Here, as in as in the initial paper, FREI were primarily considered as a replacement identical in application to SREI, including

bonding the upper and lower surfaces of the isolator to the supports. This initial work was theory based, with a focus on developing mathematical models to predict the behavior of FREI, including equations for compressive and bending stiffness considering rectangular, circular, and infinite strip geometries.

Kelly and Takhirov (2001, 2002) conducted experimental studies on FREI to confirm predictions from earlier theoretical models that fibre reinforcement could effectively replace steel plates. They tested circular and rectangular geometries, with the rectangular samples being used to assess the behavior of strip isolators. Although some issues were encountered with the testing due to poor quality of the materials employed, it was generally found that FREI could present an alternative to SREI, particularly for low-cost applications. Research at this stage largely focused on the idea that FREI could be made in a cost-effective manner suitable for deployment in developing countries, where the budget for more traditional seismic isolation systems was not available.

Another experimental study on FREI was conducted by Moon et al. (2002). This study confirmed that the horizontal and vertical stiffness provided by fibre reinforcement were comparable to those of similar SREI. An additional contribution was made by Tsai and Kelly (2002), who developed a number of approximate equations for FREI stiffness which were found to agree with the previously derived theoretical equations. It should be noted that all of this initial research was conducted primarily for application to the seismic design (base isolation) of buildings, and as such, focused exclusively on the ability of FREI to replace SREI for seismic isolation applications. Most early experimental studies also focused primarily on circular or strip isolators.

Subsequently, Toopchi-Nezhad et al. (2008) investigated unbonded FREI, defined as having no direct mechanical connection between the isolator and the support surfaces. This research work also focused on square isolators, a further departure from previous investigations. U-FREI having different aspect ratio (ratio of width to total height) values were tested under cyclic loading, and it was found that U-FREI having an aspect ratio of 2.9 exhibited a stable rollover behavior under large lateral deformations while maintaining positive tangential stiffness, leading to them being defined as Stable Unbonded FREI (SU-FREI). This behavior was found to increase their effectiveness as seismic isolators due to reduced lateral stiffness during rollover. It was noted that U-FREI having an aspect ratio of 1.9 did not exhibit this behavior.

Toopchi-Nezhad (2008) expanded on this research by examining the vertical and lateral stiffness and effective damping of SU-FREI through a combination of theoretical analysis and laboratory testing of full and quarter-scale isolators, including shake table tests. While damping was found to be dependent on vertical pressure and rate of lateral displacement, among other factors, vertical and horizontal stiffness were found to be significantly less dependent on the details of the applied loading. Rollover behavior of SU-FREI was also further described, and it was noted that lack of bonding eliminated externally applied vertical tension, reducing damage to the isolators at large lateral displacements.

Kelly & Konstantinidis (2009) performed a theoretical assessment of U-FREI to determine if friction was sufficient to hold the bearings in place to address concerns of slippage. It was found that in some cases bearing slippage could be significant, but typically not enough of an impediment to invalidate the use of unbonded isolators. They did, however, conclude that

unbonded bearings were most suitable for use where performance objectives were lower than those of traditional bearings. A further study conducted by Russo and Pauletta (2012) determined that sliding instability is primarily a concern where compressive stresses are quite low, generally less than 0.5 MPa.

When taken together, these early papers highlighted a series of advantages of U-FREI that could make them an attractive alternative to SREI. First, U-FREI could potentially be created in a single large sheet and then cut to size (for example, cut to size and shape using a water-jet), potentially making them significantly cheaper to manufacture than traditional SREI. Second, the rollover behavior previously noted prevented tension forces from developing within the bearing, eliminating concerns of tensile failure. Third, the U-FREI were compact and lightweight compared to traditional bearings, as they did not require end plates and their carbon fibre layers were thinner than steel reinforcing layers – meaning the thickness of rubber could be larger proportional to the total height of the bearing. Fourth, the lack of bonded thick steel end plates could allow for quicker and easier installation of these bearings, saving time and labor.

Continued investigations into the hysteretic behavior of FREI confirmed that they remained stable (with acceptable aspect ratio) throughout the previously discussed rollover behavior, including up to the point of failure (De Raaf et al. 2011). It was also observed that at large lateral displacements, the initial stiffness reduction during rollover is reversed as the original vertical side faces of the bearing make contact with the top and bottom supports. This behavior is illustrated in Figure 7, and has been considered a positive feature of SU-FREI as the increased

stiffness occurring after this limits further lateral motion and provides a natural level of maximum displacement the isolator can be designed for.

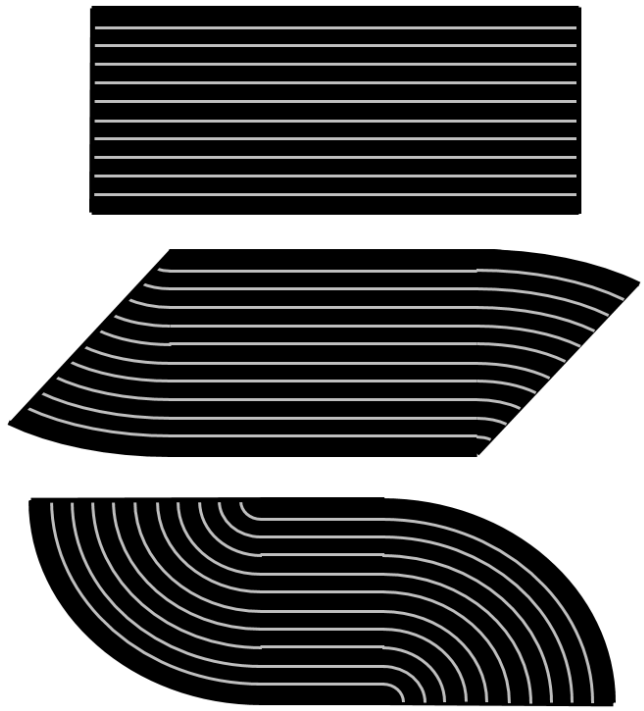

Figure 7: Rollover behavior of SU-FREI bearing

1.3 Analysis of FREI

Tsai and Kelly (2001) investigated bonded FREI and developed equations for compressive and bending stiffness. Finite element analysis has also been employed, as a study by Toopchi-Nezhad et al. (2011) created finite element models for comparative analysis of SU-FREI with bonded FREI. These models found that SU-FREI offered superior seismic performance while experiencing substantially reduced stresses compared to their bonded counterparts as no moment develops.

Numerous studies have been conducted during the early 2010s, however, these largely focused on further refining finite element and empirical equations describing SU-FREI behavior for seismic applications (Van Engelen et al., 2012; Osgooei et al., 2013; Van Engelen & Kelly, 2014).

In 2013, Angeli et al. performed theoretical and finite element analyses on rectangular FREI including the effects of both reinforcement an elastomer extensibility. This modelling exercise produced equations to determine deformations, stiffnesses, and stresses using Fourier series for rectangular FREI under bending and compression.

A similar approach was subsequently applied by Kelly and Van Engelen (2015a, 2015b) to produce a series of theoretically-derived equations governing the behavior of rectangular FREI. Methods to calculate the compression modulus, shear strain due to compression, and stress in the fibre reinforcement, among other quantities were presented. By contrast with the earlier work by Angeli et al., these formulas were generally more streamlined and more directly addressed key design parameters. They were also successful in condensing some equations which had required double-summation solutions to require only a single summation. As a result, these equations form the backbone of current theoretically-derived calculation of design parameters for FREI in bridge bearing applications.

While the previously discussed work provides insight into the behavior of FREI and allows for in-depth calculation, finite element analyses are time consuming and computationally intensive, and theoretically derived equations could be cumbersome to apply in typical engineering practice or in a design code. This was addressed by Van Engelen et al. (2016), who developed simplified approximate formulae for compression and bending modulus, as well as maximum shear strain

due to compression and rotation, of various FREI geometries, including circular, square, and rectangular isolators. These approximations were created with the intention that they could form the basis for inclusion of FREI into design codes and standards. The same authors later extended this work to include rectangular FREI (Van Engelen et al, 2017).

1.4 FREI as Bridge Bearings

Al-Anany (2016) and Al-Anany and Tait (2017a) investigated the use of SU-FREI in bridges. The primary focus of this work was on the seismic isolation of bridges, however specific investigations were also conducted to determine the viability of FREI as bridge bearings outside of seismic applications (Al-Anany & Tait, 2017b). This initial work included assessing the performance SU-FREI under rotational deformations through both finite element modelling and experiment-based analysis, as the rotations experienced by bridge bearings are different from those experienced in the seismic isolation of buildings.

Through these studies, it was found that U-FREI studied were capable of sustaining rotations of up to 0.03 radians without damage. This was partially because, when subjected to large rotations under low vertical loading, U-FREI have a tendency to 'lift off' on one edge where a bonded bearing would instead develop tensile forces. While this did introduce nonlinearity into the rotational stiffness behavior of U-FREI, it was found that U-FREI provided far superior performance to equivalent bonded FREI, with significantly lower stresses in the elastomer, in the reinforcement, and at the elastomer-reinforcement interface. It was also found that rotational and vertical loads have minor to negligible impact on the lateral response of U-FREI. All of this

behavior was found to be consistent with equations previously developed by Kelly and Van Engelen (2015a), and Tsai and Kelly (2001).

It was additionally found that U-FREI provide adequate vertical stiffness for use as bridge bearings, and that static lateral offsets of up to 1.5 times the total rubber thickness have negligible impact on the vertical stiffness. This is significantly over the 0.5 times total rubber thickness lateral displacement permitted for bridge bearings at SLS under design codes at the time the work was done, and remains well over the 0.7 that is permitted at SLS in the 2019 version of CHBDC. Overall, it was found that U-FREI could theoretically be implemented as bridge bearings.

1.5 Research Objectives

To date, full-scale installation of FREI to assess their in-situ performance as bridge bearings has not been reported on in the literature. This research focuses on quantitative and qualitative evaluation of FREI installed on two bridges along the 407 ETR ("407W-to-427S Bridge", 2020a).

This thesis aims to assess the performance of these isolators to date, determine the cause of any significant failures, and ultimately assess whether the work done to date supports the further use of FREI as bridge bearings. This is accomplished by comparing the initial bearing design calculations and performance expectations against conditions encountered in-situ, as shown in previous inspection reports, by first-hand observations, and through analysis of sensor data. Additionally, any unexplained deviations from expected performance will be postulated upon, and suggestions made as to what additional testing would be required to explain these observations.

2 Bearing Installations

2.1 General design procedure

Prior to discussion of the specific bearing installations, it is important to establish the generalized procedure by which the FREI can be designed.

For many of the basic preliminary calculations, a design guide for Goodco Z-Tech elastomeric bearing products can be referred to (Goodco Z-Tech, 2010). This guide considers code requirements along with general design best practices and first principles equations, such as for pressure, and is an appropriate selection for these FREI as Goodco Z-Tech was the company contracted to produce the FREI for this study. The basic design is then evaluated using equations based on first-principles for FREI, as well as the work of Van Engelen et al. (2017), Angeli et al. (2013), and Kelly & Van Engelen (2015a, 2015b), who laid out theoretical and practical frameworks for calculation of various critical design parameters for rectangular SU-FREI.

The design process begins by inputting the expected loads for the bridge and picking a set of bearing geometric and material parameters – constrained by the bridge geometry within which the bearings must fit and material availability. The shape factor for the bearing is calculated as shown in Equation 1,

$$S = \frac{ab}{2t_{il}(a+b)} \quad (1)$$

along with a number of derived geometric parameters, such as aspect ratio. In this context a is the bearing length, b is the bearing width, t_{il} is the thickness of an internal rubber layer, and S is

the shape factor. According to CHBDC 2019, the shape factor must be greater than 1.25 for each internal layer of elastomer.

A check is also performed to ensure the bearings do not exceed allowable vertical pressures for SLS and ULS conditions: 4.5 and 7 MPa for SLS and ULS, respectively under dead load only, and 7 and 10 MPa for SLS and ULS, respectively under total loading. For ULS dead load specifically, the allowable load may be lower: it is limited to the lesser of 7 MPa, or the value produced by Equation 2.

$$Maximum\ Pressure \leq 0.22S^2 \quad (2)$$

Additionally, the horizontal stiffness is calculated as shown in Equation 3

$$k_h = G\frac{A}{t_r} \quad (3)$$

where G is the elastomer shear modulus, A is the plan area of the bearing, and t_r is the total thickness of all rubber layers. Notably, this neglects the contribution of the fibre layers – this is acceptable as they generally compose 5% or less of the total bearing thickness, and would have a much higher shear modulus than the elastomer layers.

After horizontal stiffness the compression modulus must be calculated, as it is an important parameter for subsequent calculations. This is done using Equations 4 through 7 from Kelly and Van Engelen (2015)

$$E_c = 96GS^2(2+2p)^2 \sum_{n=1,3,5\ldots}^{\infty} \frac{1}{((\alpha^2+\beta^2)(2+2p)^2+n^2\pi^2)(n^2\pi^2)}\left(1-\frac{\tanh(\lambda)}{\lambda}\right) \quad (4)$$

$$\lambda = \sqrt{\frac{(\alpha^2 + \beta^2)(2 + 2p)^2 + n^2\pi^2}{2p}} \quad (5)$$

$$\alpha = \sqrt{\frac{24GS^2 t_{il}}{E_f t_{fl}}} \quad (6)$$

$$\beta = \sqrt{\frac{12GS^2}{K_{bulk}}} \quad (7)$$

where E_c is the compression modulus, p is the ratio of plan length over plan width, E_f is the elastic modulus of the fibre layers, t_{fl} is the thickness of an individual fibre layer, K_{bulk} is the bulk modulus of the elastomer, and α, β, and λ are dimensionless parameters.

It should be noted that for Equation 4, and all future equations with summations in this report, only the first 500 terms of the summation were applied. Additional terms past this point have been observed to have negligible effect on the results with less than 0.1% variation. In addition, a second calculation for the same quantity was conducted using the approximate formula derived by Van Engelen et al. in 2017, displayed in Equations 8 and 9.

$$E_{c\ (approx.)} = \frac{1}{\frac{1}{4p_c GS^2} + \frac{7}{5K_{bulk}} + \frac{14t_{il}}{5E_f t_{fl}}} \quad (8)$$

$$p_c = \frac{2.96p^2 + 4.01p + 0.47}{2.97p^2 - 0.14p + 1.59} \quad (9)$$

The level of agreement between these values provides a check to ensure calculations were performed correctly. Once the compression modulus, E_c, has been determined, vertical stiffness of the bearing can be calculated using Equation 10

$$k_v = E_c \frac{A}{t_r} \quad (10)$$

where k_v is the vertical stiffness. Given this value and the loading conditions specified earlier in the design process, calculation of vertical deflection or compressive strain can be determined for each loading case. According to the manufacturer's product guide, in order for the bearing design to be considered acceptable, it must satisfy Equation 11 under total load at SLS (Canam bridges, 2010)

$$\frac{\Delta_c}{t_{il}} \leq 0.07 \quad (11)$$

where Δ_c is the deflection of the bearing due to vertical compression. This was based on requirements from CHBDC, which were outlined in clause 11.6.6.4 of the 2014 version (the most current version, at the time the first calculations for this project were carried out). Alternatively, the manufacturer's product guide provides an approximate method to calculate the vertical deflection, displayed in Equation 12

$$\Delta_{c\ (approx.)} = t_i \left(\frac{\sigma_{SLST}}{E_0(1 + 2kS^2)} + \frac{\sigma_{SLST}}{E_\alpha} \right) + 1.4 t_c \left(\frac{\sigma_{SLST}}{E_0(1 + 2kS^2)} + \frac{\sigma_{SLST}}{E_\alpha} \right) \quad (12)$$

where t_i is the total thickness of internal rubber layers, σ_{SLST} is vertical compressive stress under SLS, E_0 is a hardness constant with a value of 2.52 MPa for bearings under consideration in this report, k is a hardness constant with a value of 0.64 for bearings under consideration in this report, E_α is a hardness constant with a value of 1090 MPa for bearings under consideration in this report, and t_c is the total thickness of rubber cover layers. As before, this method may be used as a check against the theoretical calculations. It may also provide a more conservative

value, which could be carried forwards if one wished to be more conservative in design – however, in this investigation, the theoretically calculated values were relied upon.

Subsequently, the allowable rotation for the bearing can be computed. Bearing rotation is a quantity imposed by the bridge structure, and for a given bearing, must not exceed the value shown given by Equation 13 (Goodco Z-Tech, 2010)

$$\theta_{all} = \frac{\Delta_c}{\frac{b}{2}} \quad (13)$$

where θ_{all} is the allowable rotation in radians. This check ensures that one end of the bearing will not lift off from its' supports under rotation. As a result, an exceedance here is less concerning for a U-FREI than for a SREI, since the unbonded and flexible nature of the bearing allows it to lift off without developing tension in the elastomer. Nonetheless, if this value is exceeded, the bearing design should be revised to further limit vertical deflection or reduce bearing footprint.

The next calculation that to be performed is to determine the stress in the fibre reinforcement under total ULS loading. Given the compressive strain under this loading case, Equation 14 may be used

$$S_{xx} = 2E_f\varepsilon_c \sum_{n=1,3,5\ldots}^{\infty} \frac{\alpha^2}{\alpha^2+\beta^2+n^2\pi^2}\frac{1}{n\pi}\left(1-\frac{\cosh(\lambda\eta)}{\cosh(\lambda)}\right)\sin(n\pi\zeta) \quad (14)$$

where S_{xx} is the stress in the reinforcement, and ε_c is the compressive strain. The values of ζ and η indicate the location on the bearing where the stress is being calculated. The original derivation, presented by Kelly and Van Engelen (2015a), can be used to find the stress at any point on the bearing. The values ζ and η at 0.5 and 0, respectively, indicate a point in the exact center of the

bearing, which is the location of maximum stress under a compressive load. Once calculated, the stress in the reinforcement can then be directly compared with the tensile strength (in terms of stress) of the fibre reinforcement: if the applied stress is greater than the tensile strength, the bearing design is considered unacceptable under ULS. It is noted that this calculation is based on compressive strain, which may be calculated as the loading divided over elastic modulus and area.

The final major check that must be completed for design is laid out in clause 4.10.10.3 of CHBDC 2019, which limits total shear strain under combined compression, γ_c, horizontal displacement, γ_d, and rotation, γ_r, to 5.5 under ultimate limit states as shown in Equation 15.

$$\gamma_c + \gamma_d + \gamma_r \leq 5.5 \quad (15)$$

Most remaining calculations in this design procedure involve the determination of these shear strains. These calculations necessarily deviate from those contained in the code due to the differences between FREI bearings and other types of elastomeric bearings.

Theoretical calculations for shear strain due to compression may be completed via Equations 16 through 19 (Kelly & Van Engelen, 2015b; Van Engelen et al., 2017)

$$\gamma_c = 24\varepsilon_c S \frac{1+p}{p} \sum_{n=1,3,5\ldots}^{\infty} \left(\frac{1}{\zeta_n n\pi} \tanh(\zeta_n)\, sin\left(\frac{n\pi}{2}\right) \right) \quad (16)$$

$$\zeta_n = \sqrt{\frac{{\lambda_2}^2(1+p)^2 + \frac{n^2\pi^2}{4}}{p^2}} \quad (17)$$

$$\lambda_2 = \sqrt{\frac{12GS^2}{K_{e=2}}} \qquad (18)$$

$$K_e = \frac{1}{\left(\frac{1}{K_{bulk}} + \frac{et_{il}}{E_f t_{fl}}\right)} \qquad (19)$$

where K_e is the effective bulk modulus of the bearing for a given value of e, e is a bearing geometry coefficient equal to 2 for all bearings considered in this report, and both λ_2 and ζ_n are dimensionless parameters. Van Engelen et al. offer an approximate procedure that may be used to verify these calculations, as shown in Equations 20 and 21

$$\gamma_{c\,(approximate)} = \varepsilon_c \left(\frac{1}{6p_s S} + \ 0.945\frac{GS}{K_e}\right)^{-1} \qquad (20)$$

$$p_s = \frac{1.42p^2 + 0.78p + 1.64}{1.43p^2 - 0.77p + 2.18} \qquad (21)$$

where p_s is a dimensionless parameter. It should be noted that Equation 21 represents only one of two possible case scenarios presented in the original paper, however, it was the relevant scenario for all bearings designed as part of this work. For further details, Van Engelen et al. (2017) may be referred to.

The next major calculation step is to determine the bending modulus, which may be calculated via Equations 22, 18, and 19 (Angeli et al, 2013; Van Engelen et al., 2017)

$$E_b = \frac{576GS^2}{\pi^4}(1+p)^2 \sum_{q=1,2,3\ldots}^{\infty} \sum_{r=1,3,5\ldots}^{\infty} \frac{1}{r^2q^2} \frac{1}{(pq\pi)^2 + \left(\frac{r\pi}{2}\right)^2 + \lambda_2(1+p)^2} \qquad (22)$$

Where E_b is the bending modulus for an internal elastomer layer. Van Engelen et al. (2017) offer an approximate procedure that may be used to verify these calculations, as shown in Equations 23 and 24,

$$E_{b\ (approximate)} = \frac{1}{\frac{1}{\frac{4}{5}p_b G S^2} + \frac{8}{5K_{bulk}} + \frac{16t_{il}}{5E_f t_{fl}}} \qquad (23)$$

$$p_b = \frac{1.16p^2 + 1.49p + 2.44}{1.10p^2 + 0.23p + 0.49} \qquad (24)$$

where p_b is a dimensionless parameter. The bending modulus was not directly used to determine the shear strain, however it can produce stresses in the reinforcement which would theoretically have to be added to those produced by compression to determine the full stress distribution. However, in practice, stress in the reinforcement is maximum at the center of the bearings under compression as shown in Figure 8, while bending produces zero stress at the bearing center and maximum stresses at a midpoint between the center and edges as shown in Figure 9.

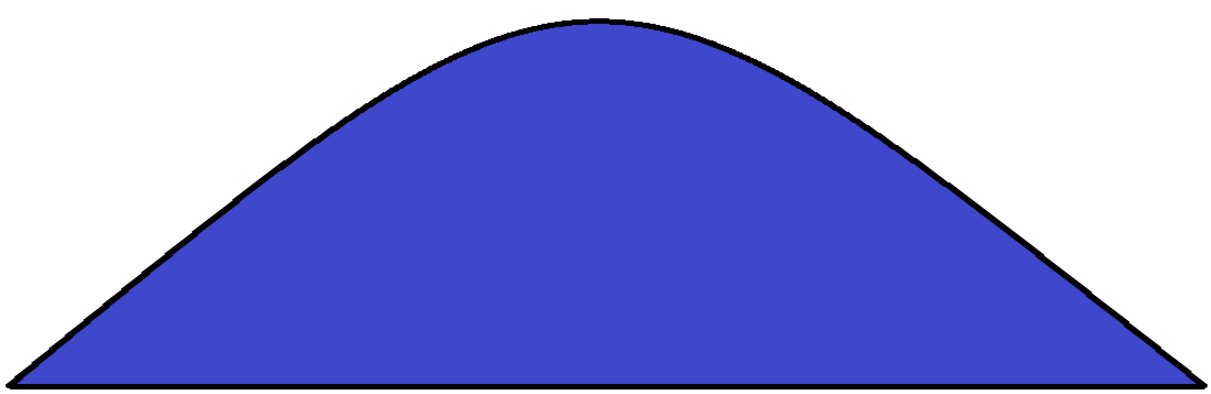

Figure 8: Stress distribution in reinforcement when the bearing is under compression

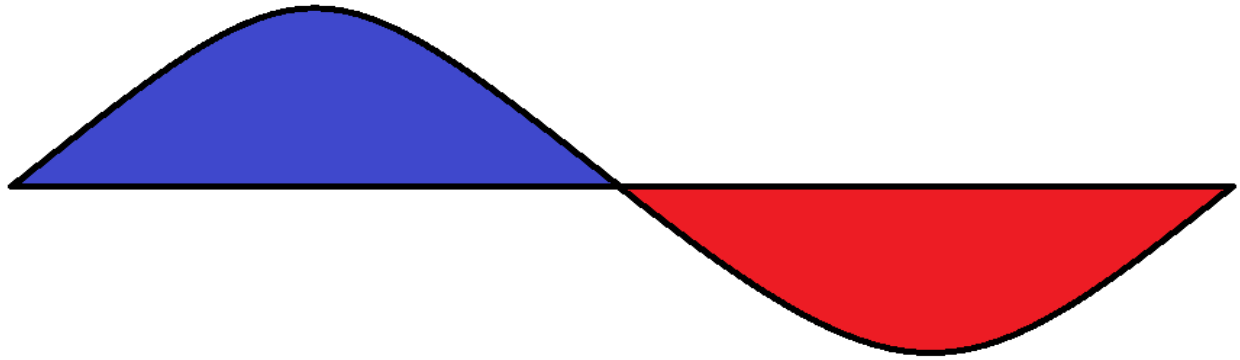

Figure 9: Stress distribution in reinforcement when the bearing is under bending

The shear strain due to rotation is calculated using Equation 25, which was originally determined by Van Engelen et al. (2017). This equation is derived from Equation 22 for bending modulus, and similarly depends on Equations 18 and 19. It should be noted that the angle θ is a value imposed by the bridge structure, not calculated through the bearing design process.

$$\frac{\gamma_r}{\frac{\theta}{n}} = \frac{192S^2}{\pi} \sum_{q=1,2,3\ldots}^{\infty} \sum_{r=1,3,5\ldots}^{\infty} \frac{1}{r} \frac{\sin\left(\frac{r\pi}{2}\right)}{(q\pi)^2 + \left(\frac{r\pi}{2}\right)^2 + \lambda_2} \qquad (25)$$

where γ_r is shear strain due to rotation, θ is the imposed rotation in radians, and n is the number of internal elastomer layers.

An approximate procedure is applied to confirm the value for shear strain due to rotation, as laid out by Van Engelen et al. (2017) and shown in Equations 26 through 30

$$\frac{\gamma_r}{\frac{\theta}{n}} = \begin{cases} 2p_r S^2 (1 + 0.05913 p_r \lambda^2)^{-1} & if\ \lambda < \lambda_t \\ S^2 \left(\frac{m}{\lambda} + \frac{j - m\lambda_t}{\lambda^2}\right) & if\ \lambda \geq \lambda_t \end{cases} \qquad (26)$$

$$j = 2p_r {\lambda_t}^2 (1 + 0.05913 p_r {\lambda_t}^2)^{-1} \qquad (27)$$

$$\lambda_t = 0.6912\sqrt{\frac{12}{p_r}} \qquad (28)$$

$$p_r = \frac{2.92}{p} + 0.86 \qquad (29)$$

$$m = 6\frac{1+p}{p} \qquad (30)$$

where m, p_r, λ_t, and j are all dimensionless parameters. The final quantity, shear strain due to horizontal displacement, may be calculated as the expected SLS horizontal displacement, which is a design parameter for the bearing, divided by the combined thickness of the internal rubber layers. This is a more conservative calculation method, as compared with including the cover layers at the top and bottom of the bearing. Shear strain due to horizontal displacement is limited by the Canadian Standards Association (CSA), as outlined in CHBDC clause 11.6.6.3.1 of S6-19, to not exceed 0.7 for laminated elastomeric bearings (CSA, 2019): if it does exceed that value, the design must be revised.

Provided the checks associated with Equations 11, 13, 14, and 15 have been satisfied, along with all other aforementioned checks, the original bearing design is considered suitable for the loading for which it was designed. It should be noted that due to geometric limitations imposed by the existing structures for which bearings were installed in this project, in some cases it was not possible to satisfy the design requirements with any reinforced elastomeric bearing. Through the rest of the report, these situations will be identified as they arise.

While there are additional checks existing in section 11.6 of the CHBDC (2019), these checks were not deemed necessary for the bearings considered in this report. Furthermore, at the time the

project was initiated, a number of these checks were not required. Prior to CSA S6-19, the guidance concerning elastomeric isolators was more limited. None of the below requirements existed in their current form in CSA S6-14, and where analogous requirements existed, no equations were included by which to judge compliance (CSA, 2014). Therefore, given their lack of relevance to the situation at hand, retroactive incorporation of these checks into the design procedure was deemed to be unwarranted.

In CHBDC clause 11.6.6.2, in addition to the shape factor equation, guidelines are set out for preventing buckling. However, previous investigations by De Raaf (2009) have found that U-FREI are “highly resistant to buckling failure”, with tested samples having critical buckling loads 8 to 11 times greater than their design loads as the unbonded boundary conditions lead to higher buckling capacity. As a result, this check was considered to be unnecessary for U-FREI.

In CHBDC clause 11.6.6.3.2, an equation is given for assessing bearing performance based on total shear strain and SLS loading conditions. This check is applicable to U-FREI, however it is analogous to the total shear strain check provided by clause 4.10.10.3, which exists in both S6-19 and S6-14. It was not included as a part of the general design calculations because of this redundancy. However, where useful as a tool to further assess bearing behavior, it was employed on a case-by-case basis.

In CHBDC clause 11.6.6.6, checks are set out to determine whether bonding for the bearings is required. As this investigation was specifically to assess the behavior of U-FREI, and because part of the requirements were for the new bearings to be unbonded and therefore easy to retrofit

onto the existing structure, this clause could not be practically applied without compromising the central goal of the project.

In CHBDC clause 11.6.6.8, requirements are set out to prevent liftoff under permanent loading conditions. However, as was demonstrated by Al-Anany (2016), the stress and strain states for U-FREI after liftoff are less than those in equivalent bonded isolators. Furthermore, rotation of isolators is typically controlled by the geometry of the bridge. The isolators considered in this report were retrofit into existing bridges, with predetermined height and limitations on plan dimensions. As a result, the measures which could have been used to prevent liftoff are curtailed. Finally, a liftoff-related limitation on rotations based on the 2014 version of the design code had been included, serving a similar purpose. For the sake of consistency, the already-implemented check was continued rather than supplementing or altering it partway through the project.

2.2 German Mills Creek Bridge

2.2.1 Site situation

As previously discussed, FREI were installed on two bridges along the 407 ETR. The first of these sites was the bridge across German Mills Creek in Markham, Ontario, as seen in Figure 10 below (Google, n.d.). This bridge was originally constructed in 1995 and widened in 2005 to add additional lanes. Today, it consists of two parallel spans each supported on 13 precast concrete girders, 3 of which were added in the 2005 widening (van Galen & Torrie, 2022). Originally, each girder was resting on a single unreinforced elastomeric bearing on the eastern abutment (van Galen et al., 2022). The 6 girders associated with the widening had all encountered problems with their associated bearings: significant bulging and deformations of the bearings had been noted, most likely due to a combination of overloading and surface imperfections or other inconsistencies in the supports upon which they were resting (M. Torrie, personal communication, Sept. 5, 2022). It was therefore decided that these 6 bearings would be replaced with FREI.

Figure 10: Aerial view of German Mills creek bearing site; maps data: Google, Image ©2023 Maxar Technologies

2.2.2 Bearing design

The design of FREI bearings for the German Mills creek site was conducted in general accordance with the design procedure as previously outlined. Key loading quantities for the design procedure are shown in Table 1. It is noted that the imposed displacements and rotations were only known under SLS: no further detail was provided for the design. Therefore, where strict reading of code provisions would call for ULS displacements and rotations, the SLS values were used: this was a known limitation in the initial design process. Key material properties, generally determined by the materials offered by the manufacturer within reasonable economic and other practicality-based constraints, are also displayed in Table 2.

Loading Quantity	*Value*
SLS Dead Load	1100 kN
SLS Total Load	1550 kN
ULS Dead Load	1485 kN
ULS Total Load	2170 kN
SLS Horizontal Displacement	3 mm
SLS Rotation	0.264 degrees

Table 1: Key loading values for bearings at German Mills Creek site

Material Property	*Value*
Tensile Strength of Fibre	4,900 MPa
Shear Modulus of Elastomer	0.81 MPa
Shear Modulus of Fibre	230,000 MPa
Bulk Modulus of Elastomer	1,090 MPa
Hardness Constant E_0	2.52 MPa
Hardness Constant E_α	1,090 MPa
Hardness Constant k	0.64

Table 2: Key material properties for bearings at German Mills Creek site

In addition, the maximum size of bearings at the German Mills site was limited to 20 mm in height, and a maximum width of 450 mm and length of 550 mm, as demanded by the geometry of the supports. As a result, it was found that the allowable rotation was less than the rotation the bearing would need to support as per Equation 13. Furthermore, the total shear strain could not be limited to 5.5 as required by Equation 15 without changing the bearing dimensions beyond what was possible for the bridge support geometry, or in a way that would lead to violation of limits on vertical bearing pressures. This was primarily due to shear strain from rotation, which

exceeded 6.15. The final design parameters, considered the best compromise solution given the imposed restrictions, are displayed in Table 3 below. Note that only the parameters required to define the bearing are listed, along with the exterior dimensions of the bearing. The total shear strain was found to be 7.66, while the rotation was approximately 2.6 times higher than the calculated allowable rotation based on Equation 13. It is noted, however, that one of the reasons FREI are being considered as bridge bearings is because experimental test results have indicated they may offer superior performance to traditional SREI under large rotations. A comparative analysis between FREI and SREI under this scenario will be shown in Section 3.3.1.

Design Parameter	*Value*
Cover Layer Thickness	5 mm
Reinforcement Layer Thickness	0.51 mm
Reinforcement Layer Number	2
Elastomer Layer Thickness	8.98 mm
Elastomer Layer Number	1
Plan Length of Bearing	550 mm
Plan Width of Bearing	450 mm
Total Bearing Thickness	20 mm

Table 3: Key design parameters for bearings at German Mills Creek site

2.2.3 Notes on Installation

Installation of the bearings was conducted on April 9, 2021, while exact temperature at time of installation was not recorded (M. Torrie, personal communication, Sept. 11, 2022). It was decided that the bearings would be installed in a different fashion on the westbound versus the eastbound bridge, for experimental purposes. On the westbound bridge, the bearing supports

were smoothed out and specially fitted for the new bearings. On the eastbound bridge, the supports were left in their existing condition, in an effort to determine how sensitive the bearings would be to surface imperfections or other irregularities in the supports (van Galen & Torrie, 2022).

During installation of the bearings a loud and unexpected sound was noted, postulated to be caused by a failure in the bearing, occurring as the southernmost FREI bearing on the eastbound lanes as the jacking was removed and the bearing loaded. While no external failure of the bearing was visible at the time, auditory evidence suggested that a raised bump or other irregularity in the support geometry had created a sufficient load concentration to damage some of the carbon fibre reinforcement in the bearing (van Galen & Torrie, 2022). The bearing was left in place. Due to this noted damage upon installation, further examination of this bearing will provide insight into the ability of FREI to continue functioning despite being damaged, and its resistance to further deterioration under that condition.

2.3 Steeles Avenue Bridge

2.3.1 Site situation

The second site at which FREI bearings were installed was the bridge along the ramp from the 407 Westbound lanes to the 427 Southbound lanes which crosses over Steeles Avenue in Etobicoke, Ontario, as seen in Figure 11 below (Google, n.d.). This bridge was originally constructed in 1990 and consists of a single span supported by 3 steel tub girders. A cross-section of one such girder is shown in Figure 12 below ("407W-to-427S Bridge", 2020a).

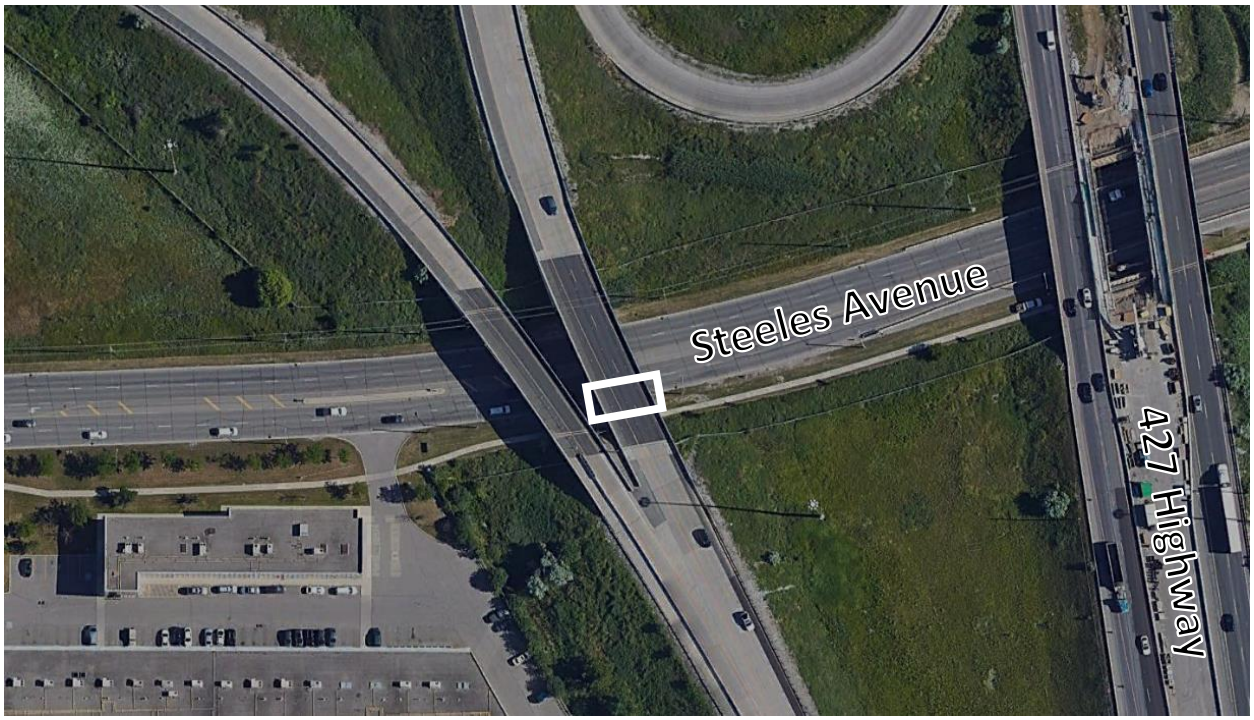

Figure 11: Aerial view of Steeles Avenue bearing site; Maps Data: Google, Image Landsat/Copernicus

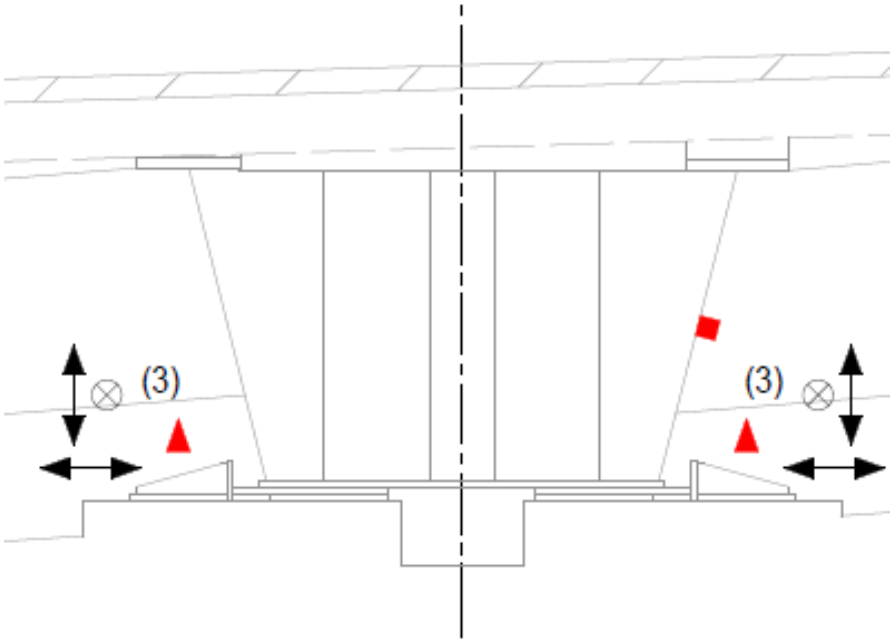

Figure 12: Cross-sectional view of Steeles Avenue bridge girder, including bearing positions

Originally, each girder was resting on a pair of unreinforced elastomeric bearings on the southern abutment – one on the eastern side of each girder, and one on the west. Of the total 6 bearings, all were in poor condition and 4 were recorded as having failed, with large-scale deformations including rubber flowing out from under the shoe plates and a characteristic undulating shape. The condition of the eastern bearing of the western girder is shown in Figure 13 ("407W-to-427S Bridge", 2020a). It was therefore decided that all 6 of these bearings would be replaced with FREI.

Figure 13: Unreinforced, failed Steeles Avenue bridge bearing

2.3.2 Bearing design

The design of FREI bearings for the Steeles Avenue site was conducted in general accordance with the design procedure as previously outlined. Key loading quantities for the design procedure are shown in Table 4. It is noted that the imposed displacements and rotations were only known under SLS: no further detail was provided for the design. Therefore, where strict reading of code provisions would call for ULS displacements and rotations, the SLS values were used: this is a known limitation of the design process. Key material properties, generally determined by the

materials offered by the manufacturer within reasonable economic and other practicality-based constraints, are also displayed in Table 5.

Loading Quantity	*Value*
SLS Dead Load	510 kN
SLS Total Load	975 kN
ULS Dead Load	630 kN
ULS Total Load	1515 kN
SLS Horizontal Displacement	2 mm
SLS Rotation	0.4 degrees

Table 4: Key loading values for bearings at Steeles Avenue site

Material Property	*Value*
Tensile Strength of Fibre	4,900 MPa
Shear Modulus of Elastomer	0.81 MPa
Shear Modulus of Fibre	230,000 MPa
Bulk Modulus of Elastomer	1,090 MPa
Hardness Constant E_0	2.52 MPa
Hardness Constant E_α	1,090 MPa
Hardness Constant k	0.64

Table 5: Key material properties for bearings at Steeles Avenue site

In addition, the maximum size of bearings at the Steeles Avenue site was restricted to 40 mm in height, and a maximum of 350 mm in width and 450 mm in length, as limited by the geometry of the supports. Although these bearings could be designed without any major exceedance of the described checks, these limitations forced a design with regard to vertical displacement that had no margin for error: Equation 11, which demands that vertical deflection be less than 7% of the

total height of rubber, is satisfied if the manufacturer-approved approximate method of calculating vertical deflection as displayed in Equation 12 is used, with the calculated vertical deflection being approximately 4% less than the allowable. However, using the theoretical method of calculating vertical deflection based on compression modulus, the calculated vertical deflection is greater than the allowable by approximately 1%. The final design parameters, considered the best compromise solution given the imperfect installation conditions, are displayed in Table 6 below. Note that only the parameters required to define the bearing are listed, along with its' exterior dimensions. The final design is considered acceptable, but it is noted that vertical displacement is the most critical design parameter, in the sense that its' related checks are closest to failure.

Design Parameter	*Value*
Cover Layer Thickness	5 mm
Reinforcement Layer Thickness	0.51 mm
Reinforcement Layer Number	3
Elastomer Layer Thickness	14.235 mm
Elastomer Layer Number	2
Plan Length of Bearing	450 mm
Plan Width of Bearing	350 mm
Total Bearing Thickness	40 mm

Table 6: Key design parameters for bearings at Steeles Avenue site

2.3.3 Notes on Installation

The bearings were installed on July 12th, 2019 with an ambient temperature of approximately 21 degrees Celsius. Prior to installation, all bearing seats were reconstructed with concrete being

removed to a depth of 115 millimetres from the pre-existing bearing seat level, and new bevelled shoe plates with guide bars being added. However, it was noted during the initial inspection that those guide bars on the north edge of the bearings, which would have run perpendicular to the span of the bridge, were missing ("407W-to-427S Bridge", 2020a).

Bearings were assigned identifying numbers, for ease of reference both in future inspection reports and in data collection and analysis. These identifiers are displayed in Table 7 below.

ID Number	*Girder*	*Bearing*
J1-E	East	East
J1-W	East	West
J2-E	Center	East
J2-W	Center	West
J3-E	West	East
J3-W	West	West

Table 7: Bearing identifiers at Steeles Avenue site

3 Field observations

3.1 German Mills Creek Bridge

3.1.1 Site visits

A site visit was conducted on June 22, 2022, 439 days after the bearings were initially installed. The temperature was approximately 35 degrees Celsius, according to historical weather data from the organization Time and Date for nearby Thornhill (timeanddate.com). At that time, it was observed that 5 of the 6 bearings displayed minimal or no bulging and no signs of debonding between the fibre and rubber elements.

The exception to this was the southernmost FREI bearing on the eastbound bridge, as highlighted in Figure 15 (Google, n.d.). This bearing will be referred to as Bearing #1, in accordance with the numbering in Figure 15. As previously noted, this bearing had produced a loud and unexpected noise during installation, due to an irregularity in the support. While this bearing displayed minimal bulging along most edges, one specific area showed noticeable bulging. At this location, a slick, black, glossy substance was adhering to the surface of the bearing, as shown in Figure 14. It was distributed in a way that appeared that it had, at some point in the past, escaped from the fiber layers and seeped down the surface of the bearing. However, if this was continuing to occur, it was so slow as to make progress unnoticeable to the naked eye. It was also noted that a deformity existed in the lower support at this location, as shown in Figure 14.

Figure 14: Damaged bearing at German Mills. Intersection point of white lines illustrates a change in inclination of the bearing of approximately two degrees, forming a 'bump' directly under the damaged region of the bearing.

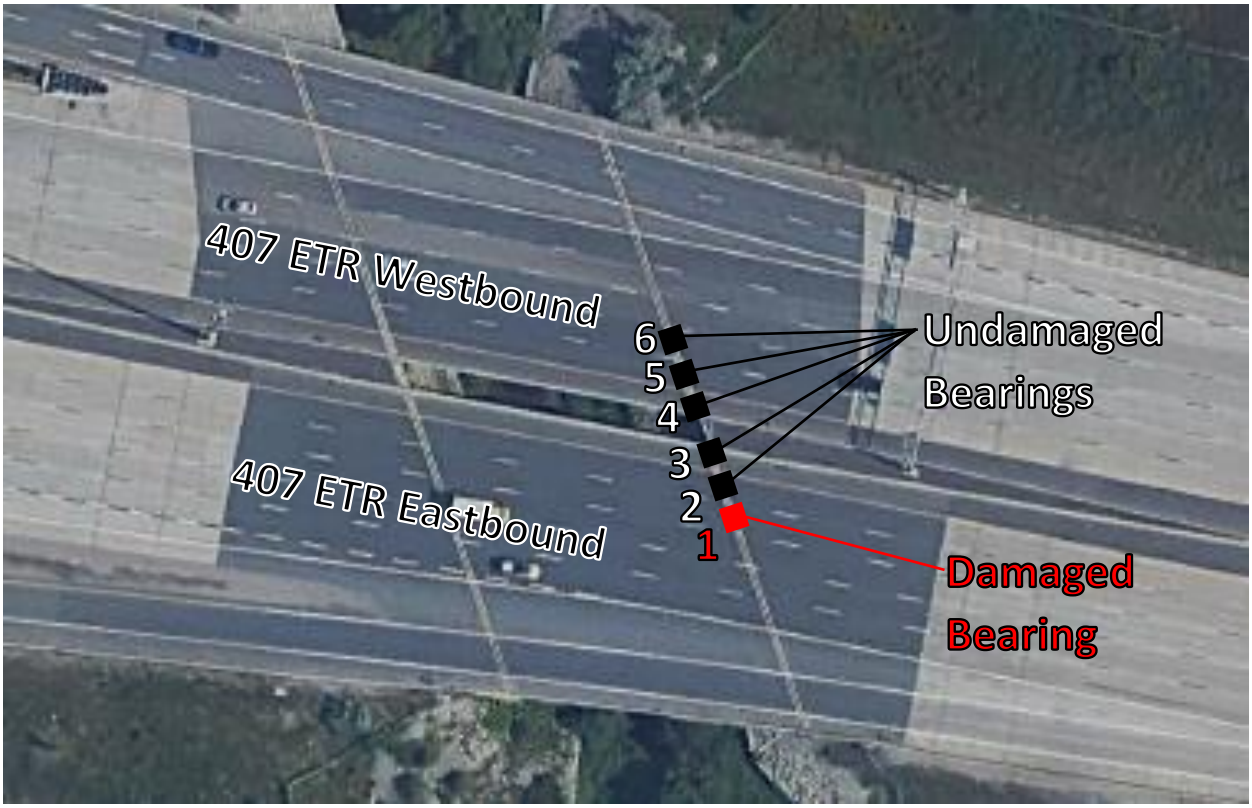

Figure 15: Location of bearings at German Mills Creek site; maps data: Google, Image Landsat/Copernicus

As the initial site visit suggested no clear explanation for this liquid, a second site visit was scheduled for July 23, 2022, in order to gain additional insight. The site visit was conducted near noon, and the temperature was approximately 30 degrees Celsius, according to historical weather data from the organization Time and Date for nearby Thornhill (timeanddate.com).

During this second site visit it was first confirmed that bearings 2 through 6 remained in the same condition noted upon the previous inspection, then a closer inspection was made of bearing 1.

It was found that the previously noted liquid had largely solidified, the material now solid and slightly springy to the touch. However, still-fluid liquid was observed at a second location along the same side of the bearing. A small amount was scraped off onto the tip of a wooden ruler, as shown in Figure 16 and Figure 17. It was observed that the liquid was black in colour, had a low viscosity, and was shiny, with very little odor. Over the next few hours it was absorbed into the tip of the ruler, staining it black.

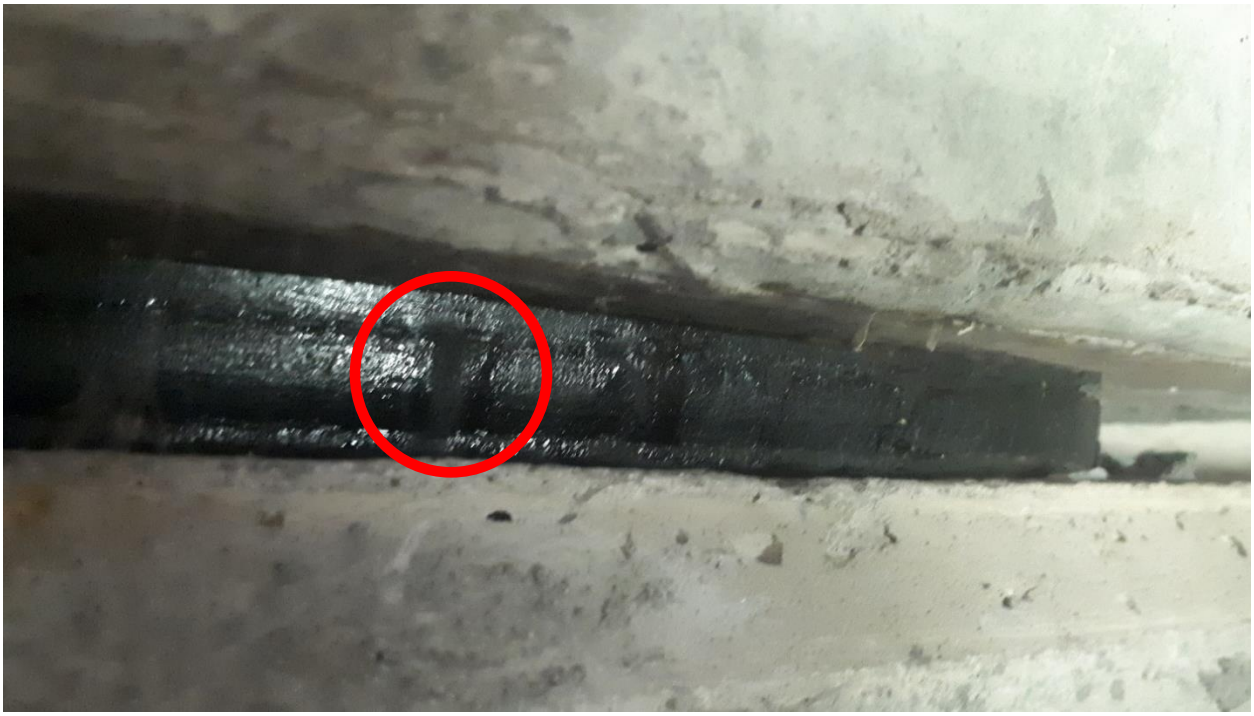

Figure 16: Bearing 1 at German Mills Creek site with location of liquid recovery marked

Figure 17: Unidentified black liquid staining tip of ruler

Aside from this single bearing, all other bearings showed no signs of damage or deterioration. An example of such an undamaged bearing, the northernmost bearing on the eastbound bridge is displayed in Figure 18 and Figure 19. As can be seen, the bearing does not have any visible liquid on it. While there is some minor bulging around the sides, it is noticeably less pronounced than that in the damaged bearing.

Figure 18: Undamaged bearing at German Mills Creek; no liquid visible

Figure 19: Undamaged bearing at German Mills Creek; slight bulging which is not indicative of damage

3.1.2 Discussion

As previously noted, no deterioration or other issues have been observed in bearings 2 through 6 since the time of installation. The only bearing in which any unusual behavior was observed is the one that had been damaged during installation. However, even this bearing had not displayed any delamination or other visible external damage. While the unidentified liquid was unexpected, the relatively small volumes involved and the lack of damage to nearby bearings mean that until and unless further deterioration is observed, it may be assumed that the bearing is continuing to resist the vertical pressures placed upon it and allow for lateral and rotational movements despite its' initial damage.

No conclusive explanation for the unidentified liquid was determined, however, it was postulated that there was an association with damage, as bearing 1 was known to have also been the only bearing damaged internally during installation. It was also postulated that temperature may be a factor, as the site visits were both conducted on relatively hot days, and the latter site visit

confirmed that some of the liquid had not yet solidified. In order to further characterize this behavior, further observations taken at Steeles Avenue were required.

3.2 Steeles Avenue Bridge

3.2.1 Inspection Reports

Four inspection reports were created for the Steeles avenue site. The first of these was based on a site visit carried out during August of 2019, approximately one month after installation. Subsequent site visits for the next three inspection reports occurred during October 2019, April 2021, and December 2021. The bearing layout is displayed in Figure 20 ("407W-to-427S Bridge", 2020a).

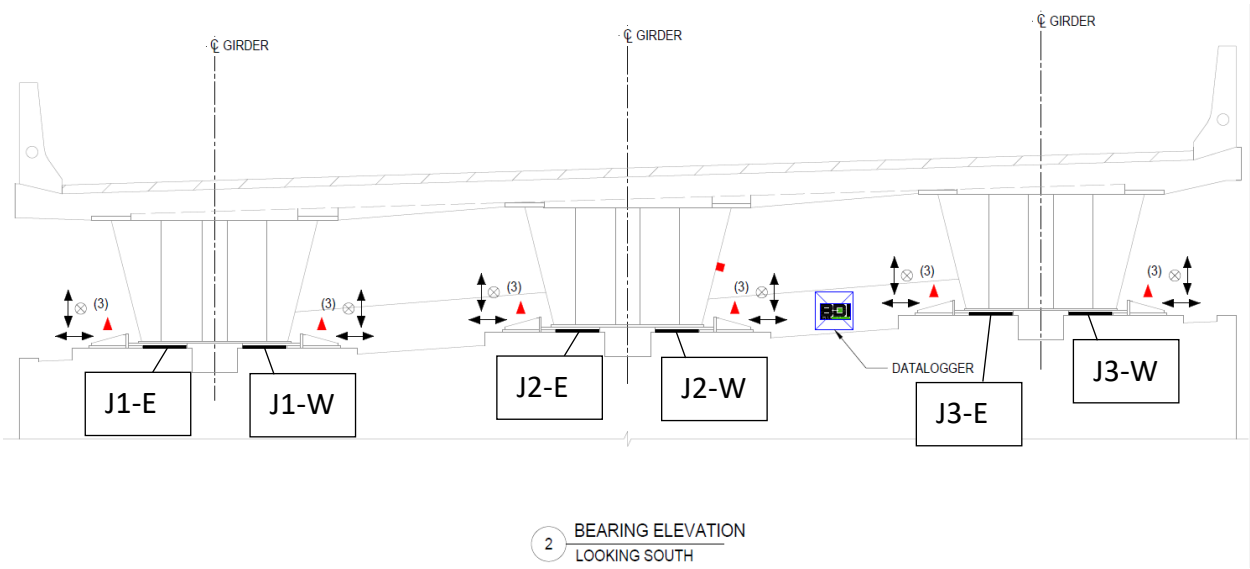

Figure 20: Bearing layout at Steeles Avenue as shown in first inspection report ("407W-to-427S Bridge", 2020a)

The first inspection report noted an issue with the bearing installation in the form of unequal loading: at both the center and west girders (J2 and J3), it was observed that the western bearing was bulging to a noticeably greater extent than the eastern bearing ("407W-to-427S Bridge", 2020a). This suggests that bearing J2-W and J3-W were under vertical loads significantly greater than their design load almost immediately upon installation. If a single bearing were taking the load for an entire girder, the loads could have been as much as doubled. This is particularly severe

due to the relatively low height of the bearings (40mm), which limits their total compressibility in the vertical direction. Based on these observations, any deterioration in bearings J2-W and J3-W consistent with vertical pressures exceeding design specifications should not be considered a failure of the FREI, but of the specific installation conditions at the Steeles Avenue site. From the point where unequal loading was noted, deterioration of the overloaded bearings was to be expected. The details of how the design calculations predict the bearing would behave under overloaded conditions, and how that compares with actual observations, will be discussed in detail.

The second inspection report, based on a site visit in October of 2019, revealed the first degradation of the bearings. Bearings J1-E, J2-W, and J3-W had all suffered delamination between the rubber and fibre layers, visible as increased bulging not confined by the reinforcing layers ("407W-to-427S Bridge", 2020b). The most heavily impacted area was the east face of bearing J3-W. These delamination events were associated with increased bulging in the undamaged bearings (J1-W, J2-E, and J3-E), suggesting that delamination had allowed the damaged bearings to further compress under vertical load, which then increased the load on bearings J1-E, J2-W, and J3-W. In addition to this degradation, bearing J3-W was noted to have shifted or 'walked' 9 mm to the north, resulting in a slight (approx. 2%) reduction in contact surface with the girder above. This may have increased stress concentrations, however it is likely a minor effect compared with the previously noted unequal load distribution.

The third inspection report was based on a site visit in April of 2021. In between the previous inspection and the current one, additional bars were added to the bearing mounts with the

intention of restraining further northward shifts such as that experienced by bearing J3-W. This had the effect of reducing bearing visibility and preventing any precise measurements of further shifts ("407W-to-427S Bridge", 2021a). Relatively little additional bearing degradation had taken place since the previous round of observations, with bearings J1-E and J2-W remaining in a very similar condition to that recorded previously. The previously undamaged bearings exhibited only slight increases in bulging, consistent with taking on a larger portion of the vertical load due to the previously noted deterioration of their paired bearings. However, the report indicated that the west and east faces of bearing J3-W were "splitting". Further explanation was not provided, nor were images illustrating this behavior included. As a result, a site visit was required to further characterize this behavior.

The fourth inspection report, based on a site visit conducted in December of 2021, was generally consistent with a worsening of previously noted deterioration. Minor increases in loss of layer adhesion were noted on bearings J1-E, J2-W, and J3-W, with only very minor changes in the level of bulging on the other bearings. However, on bearing J2-W, a new phenomenon was observed: a large black stain had formed on the northern shoe plate, and small amounts of unknown black liquid were recorded on the face of the bearing itself ("407W-to-427S Bridge", 2021b). The report made no further comment, however, it was noted that this may be the same liquid previously noted during the site visits to German Mills. Closer examination of any such liquid was therefore prioritized for a future site visit. The condition of the bearings based on the noted observations in these inspection reports, up to the time of inspection report four, is summarized in Table 8 below.

Bearing	*Initial inspection condition*	*Final inspection condition*
J1-E	Approximately proportional bulging.	Delamination between rubber and fibre layers at north face of bearing.
J1-W	Approximately proportional bulging.	Increased bulging; no damage.
J2-E	Appears unloaded; no bulging.	Increased bulging; no damage.
J2-W	Appears overloaded, significant bulging.	Delamination between rubber and fibre layers at north face of bearing. Black liquid leaking from bearing, staining shoe plate.
J3-E	Appears unloaded; no bulging.	Increased bulging; no damage.
J3-W	Appears overloaded, significant bulging.	Delamination between rubber and fibre layers at east and west faces of bearing. "Splitting" of elastomer on multiple faces. "Walking" northwards; at least 9mm.

Table 8: Summary of Steeles Avenue site bearing conditions at initial and final inspection reports

Based on these observations, bearing J1-E was likely more heavily loaded than bearing J1-W, but not to the extent where a major difference in initial bulging was observed. This would explain why bearing J1-E deteriorated, while bearing J1-W did not.

3.2.2 Site visit

To supplement the inspection reports, a site visit was conducted at the Steeles Avenue site on August 4, 2022. The temperature was approximately 27 degrees Celsius, according to historical weather data from the organization Time and Date for nearby Thornhill (timeanddate.com). It was observed that the condition of the bearings was generally consistent with the trends previously observed in the inspection reports, with some slight additional deterioration of the

bearings consistent with previous observations. However, it was found that previous inspection reports had potentially overlooked or understated the extent to which the unidentified black liquid was present on the bearings. A summary of liquid observed on these bearings, as observed during the August 4 site visit, is shown in Table 9.

Bearing	*Previously noted liquid*	*Liquid as observed on August 4*
J1-E	None remarked on	Liquid coverage observed on multiple sides.
J1-W	None remarked on	No leakage observed.
J2-E	None remarked on	No leakage observed.
J2-W	Black liquid stain noted on north side of bearing and shoe plate.	Liquid coverage observed on multiple sides, original stain had partially faded and second, fresher stain had formed.
J3-E	None remarked on	No leakage observed.
J3-W	None remarked on	Liquid coverage observed on multiple sides.

Table 9: Record of unidentified liquid in inspection reports contrasted with field observations

Based on the discrepancy between site visit observations and those recorded in the previous inspection report, a careful review was made of the photos taken during previous rounds of inspection, and inquiries made. It was found that the photos taken during the third and fourth previous inspections showed evidence of the liquid on bearings J1-E, J2-W, and J3-W – all the bearings currently exhibiting leakage. It is postulated that this leakage had been overlooked because it was quite extensive, covering almost the entire face of the bearings to the point where it was difficult to discern the original texture of the material. An example of this, as seen on bearing J2-W, is shown in Figure 21. Notably, while the stain on the left is partially faded, the one on the right is more sharply defined and was not visible in photos taken during previous inspection reports. This indicates that the liquid has appeared at different times on this bearing.

Figure 21: Bearing J2-W with unidentified liquid over the majority of bearing face

Aside from the leaking, the bearings generally conformed to previous observations – however, additional details were noted during the site visit which were not reflected in the inspection reports. The first of these was the manner in which splitting of bearing J3-W had occurred. The 'splitting' of the rubber elastomer mentioned in the inspection reports was observed to be occurring at the locations where the reinforcement had previously been bonded, prior to delamination. This is shown in Figure 22. It appears that where delamination had occurred, a grid of holes had been left in the elastomer where the fibre had torn out of the bulging area, perforating it along that horizontal plane. This defined the line along which splitting which would later occur, as further bulging pulled the elastomer apart and stressed the perforated area beyond its' capacity in tension.

Figure 22: Bearing J3-W splitting behavior occurring along line of previous delamination

Additionally, bearing J1-W, previously undamaged, was noted to have initial signs of delamination along the western face as shown in Figure 23. This was noteworthy, as it is the first instance of both bearings on a given girder displaying signs of deterioration. It is postulated that as bearing J1-E deteriorated, it became more compressible, causing a majority of the vertical load to be transferred to bearing J1-W and leading to delamination. This would be a reversal of the initial conditions, where bearing J1-E appeared to be under greater vertical load – however, if the compressibility of bearing J1-E was sufficiently impacted by the deterioration it had undergone, it is a plausible outcome.

Figure 23: Limited delamination observed at bearing J1-W

Although four of the bearings exhibited damage at the time of the site visit, two of the bearings remained in good condition. Bearing J3-E, which experienced no deterioration, is displayed in Figure 24. As discussed, there is visible bulging due to compressive stress, but no delamination or other damage has taken place as a result of it. It displays none of the characteristic glistening typically associated with leakage, nor was any staining observed on the supports.

Figure 24: Bulging but undamaged bearing J3-E

3.2.3 Discussion

In general, the bearings at Steeles avenue exhibit some deterioration since the time of installation. This deterioration is attributable to imbalances in loading of the bearings. As previously noted, this is an issue with the manner of bearing installation and the specific conditions of the bridge in question rather than a design issue with the FREI. It is noted that much of this is related to the fact that two bearings support each girder, creating the potential for them to do be unequally loaded. These situations should be avoided in future installations of FREI, unless such difficulties can be conclusively ruled out.

Aside from this, it is worth examining what might have led to the unequal loading. According to OPSS.PROV 922, the governing standard for installation of such bearings in Ontario: "The top of the bearing shall be set at the theoretical elevation specified in the Contract Documents, within the following tolerances: Concrete deck and precast I-type girders ± 5 mm… Steel plate girders 0 to + 3.0 mm… Steel and precast concrete box girders 0 to + 2.0 mm" (Ontario Provincial Standards

Specification, 2020). The standard also provides that "For elastomeric bearings, the finish of the concrete surface shall be smooth and not vary greater than 1 mm along a straightedge placed in any direction across an area that extends at least 25 mm beyond the outside limits of the bearing."

At the Steeles Avenue site, the concrete seats for each bearing were separate, and the girders were steel tubs – a variant of box girders, but one that a contractor could have interpreted as a steel plate girder instead. As a result, it is possible that points on the bearing seats varied by as much as 5 millimetres: up to three millimetres from the general tolerance, plus up to two millimeters of variation from the tolerance within each bearing seat. In this case, because the bearings were only 40 millimetres tall, a 5 millimetre error amounts to 12.5% of the total bearing height. While it is unlikely all errors would have been additive in this manner, the point highlighted by this comparison is that relatively short FREI bearings, when paired on a girder, may require tighter tolerances than those given as standard in OPSS specifications.

Aside from the question of cause, the behavior of the bearings over time under this unequal loading is noteworthy. Despite significant overloading leading to damage, bearing deterioration generally slowed over time rather than accelerating, and they continued to function despite their deteriorated condition. This is desirable behavior, as it suggests that minor damage to FREI will not lead to a situation where the bearing continues to experience additional deterioration at an accelerating pace until it fails. This was already suggested by the behavior of the damaged bearing at German Mills, but the Steels Avenue observations confirm this.

A concern is the unidentified liquid observed on the bearings, postulated to be escaping from them. As this behavior was observed at both sites and does not have an obvious explanation, it will be addressed in detail in Section 3.3.3, Unidentified Liquid.

3.3 Analysis

3.3.1 Rotational Capacity

Given that the FREI bearings installed at the German Mills site were expected to exceed code rotational limits, it is worth examining them in direct comparison to SREI to illustrate why they were considered as a preferable option for this site. Design of these alternative SREI bearings was limited by the dimensional constraint of 20 millimetres height which had to be observed at this site, and the plan dimensions were set as 450 millimetres in width and 550 millimetres in length to match the U-FREI bearing. In addition, S16-19 clause 11.6.6.4 requires that the steel reinforcing layers be at least 3 millimetres thick – this was taken as an exact value. Furthermore, in compliance with CHBDC clause 11.6.6.5.2, elastomeric cover of the steel layers on the top and bottom had to be a minimum of 3 millimetres thick – this was increased to 4 millimetres to account for fabrication tolerances (CSA, 2019). In accordance with the same standard, cover on the side surfaces was assumed to be 6 millimetres.

These constraints when taken together define a bearing design. As a result, no other geometric considerations (such as shape factor) could be taken into account. The final parameters for a SREI bearing designed for the German Mills site are shown in Table 10. The material properties of the elastomer were taken as identical to those used for the FREI bearings, while the yield strength of

the steel reinforcement was taken to be 230 MPa in accordance with clause 11.6.1.5 of S6-19 (CSA, 2019), with the elastic modulus assumed to be a typical value of 200 GPa.

Design Parameter	*Value*
Cover Layer Thickness	4 mm
Reinforcement Layer Thickness	3 mm
Reinforcement Layer Number	2
Elastomer Layer Thickness	6 mm
Elastomer Layer Number	1
Plan Length of Bearing	550 mm
Plan Width of Bearing	450 mm
Total Bearing Thickness	20 mm

Table 10: Key parameters for alternative steel bearing design for German Mills Creek site

Given this set of geometric and material parameters, design calculations were carried out in general accordance with those conducted for FREI as previously discussed, with only a few alterations. The first alteration was regarding calculation of compression modulus, which was accomplished using Equations 31 and 32

$$E_c = \frac{384}{\pi^4} G S^2 (1+p)^2 \sum_{m=1,3,5\ldots}^{\infty} \frac{1}{m^4 {\zeta_m}^2} \left(1 - \frac{2p}{m\pi\zeta_m} \tanh\left(\frac{m\pi\zeta_m}{2p}\right)\right) \qquad (31)$$

$$\zeta_m = \sqrt{1 + \frac{48 G S^2 (1+p)^2}{\mathrm{K_{bulk}}(m\pi)}} \qquad (32)$$

where ζ_m is a dimensionless constant. These equations are different from those relied upon previously because of the differences in the bearings. Equations 31 and 32 were developed for

use on rectangular SREI, not FREI (Kelly & Konstantinidis, 2011). The second major difference was that calculations of reinforcement stress were performed according to clause 11.6.6.4 of S6-19, which applies to steel reinforcement – the relevant calculation is shown in Equation 33

$$S_{xx} = \frac{3t_{il}\sigma_{\mathrm{ULST}}}{t_{sl}} \qquad (33)$$

where σ_{ULST} is vertical compressive stress under ULS. It is noted that this calculation was adapted from the original clause to apply to ULS rather than SLS. The third major difference was that calculations of shear strain due to rotation were performed according to clause 11.6.6.3.4 of S6-19, as well as clause 4.10.10.3: both were considered, and the differences noted. The relevant calculations are shown in Equations 34 and 35, respectively

$$\gamma_r = 0.5\left(\frac{b-12}{t_{il}}\right)^2 \frac{\theta}{n} \qquad (34)$$

$$\gamma_r = 0.55\frac{b^2\theta^2}{t_{il}t_r} \qquad (35)$$

where n is the number of internal rubber layers. The fourth and final major difference was the calculations of shear strain due to compression were performed according to clause 4.10.10.3 of S6-19 - the relevant calculation is shown in Equation 36.

$$\gamma_c = \frac{\sigma_{\mathrm{ULST}}}{GS} \qquad (36)$$

The above method was chosen as a reasonable compromise between simplicity and direct comparability with previous calculations: as this is primarily an exercise in comparing calculated performance between SREI and FREI, and as such the calculation methodology was maintained.

It is noted that, even within a direct reading of CSA S6-19, there are often multiple subtly different forms of a given equation – as was the case for calculation of shear strain due to rotation. In the specific case of shear strain due to rotation, both forms were applied because the extreme limitation on bearing height at German Mills makes the differences, which would ordinarily be minor, far more impactful than they would otherwise be due to the greater fraction of total rubber height taken up by the cover layers on top and bottom of the bearing.

This analysis found no new failures or near-critical parameters in any checks the FREI bearing had passed. However, there was a significant difference in the magnitude of the exceedances to the rotational checks. When comparing the imposed to allowable rotation: rather than exceeding by a factor of 2.62 as had been the case with the FREI bearing, the SREI bearing exceeded by a factor of 5.25, driven by a significantly smaller vertical displacement due to compression. Additionally, where the FREI had a total shear strain of 7.66 (compared to the limit of 5.5), the degree of exceedance in the SREI was dependant on the clause of CHBDC used for reference: using the rotational shear strain equation based on clause 4.10.10.3 the total was 7.13, while using the rotational shear strain equation based on clause 11.6.6.3.4, the total was 13.3. In both cases, all but 1.0 of that total was driven by rotational shear strain. These values are summarized in Table 11.

Design Parameter	*U-FREI Bearing*	*SREI Equivalent Bearing*
Imposed/Allowable Rotation	2.6	5.2
Imposed /Allowable Total Shear Strain	1.3 (Case 1 equivalent) 1.4 (Case 2 equivalent)	1.3 (Case 1) 2.4 (Case 2)

Table 11: Comparison of key design checks for U-FREI and equivalent SREI bearings designed for German Mills creek site

These differences in magnitude of exceedances, combined with the observation that no bearing degradation has been identified in 5 of the 6 bearings at German Mills, highlight the extent to which FREI can outperform SREI as bridge bearings when subjected to large rotations. Equivalent SREI fail the relevant rotation check and total shear strain check based on the more modern definitions of CHBDC clause 11.6.6.3.4 by far greater margins than FREI.

No major inferences concerning rotation could be made based on field observations at Steeles Avenue.

3.3.2 Vertical Compression

At the Steeles Avenue site, it was noted based on initial inspection that some of the bearings appeared to be carrying the load of an entire girder rather than only half, where the second bearing remained virtually unloaded. This was speculated to be the primary cause of damage to bearings at Steeles Avenue. Using the design procedure as previously outlined, a scenario was run to determine the impact of such a dramatically increased load on key design parameters. As was previously noted, the controlling parameter for design of the Steeles Avenue bearings – that is; the parameter closest to exceedance criteria – was vertical displacement, which was found to be 1% greater than the calculated allowable value based on theoretically derived equations.

In order to estimate the impact of a single bearing holding the loads from an entire girder (as opposed to sharing it between two bearings), the vertical loads at SLS and ULS were doubled. Then, the design procedure calculations laid out previously were repeated to determine how this dramatic increase to loading impacted the bearing design parameters. It was found that this caused the bearing to fail a wide array of design checks. Pressures at every single loading case

exceeded their manufacturer-recommended limits. The vertical deflection exceeded allowable values by 102%, based on theoretical equations. In addition, the check for total shear strain was exceeded with a value of 5.86 where the maximum allowed by CSA S6-19 is 5.5, driven primarily by shear strain due to compression which contributed 4.58 of that value.

One of the few checks that passed by a considerable margin was related to stress in the reinforcement, where allowable load was still less than half of maximum.

Design Parameter (Imposed/Allowable)	*Baseline Loading Case*	*Double Loading Case*
Vertical Deflection	1.01	2.02
Total Shear Strain	0.65	1.07
SLS Dead Load	0.72	1.44
ULS Total Load	0.96	1.92
Reinforcement Stress	0.23	0.46
Rotation	0.30	0.15

Table 12: Comparison of key design criteria between U-FREI under different loading cases for Steeles Avenue site

The observed failures in the Steeles Avenue bearings are generally consistent with what would be suggested by the aforementioned calculations. Under large vertical deflections Poisson's ratio suggests that significant bulging will occur, in line with what was observed during site visits. Rubber layers were being prevented from further bulging by the confinement of the fibre layers, as such, it is postulated that the failures began with delamination between the rubber and fibre layers at the points of greatest stress. The failures then expanded to larger and larger scale delamination. In the extreme case the delaminated areas began to undergo further splitting as a

result of bulging-induced tensile stress concentration, where the pulling out of the fibre layer had left perforations in the rubber. There were no signs of failure of the fibre layers themselves.

Since the design procedure as previously discussed was not based on the most modern versions of the highway bridge design code (CSA S6-19), the most critical mode of failure – vertical compression – was also examined under the requirements of the most modern code version for the sake of completeness. Rather than limiting compressive deflection as a proportion of bearing height, the way the design procedure and CSA S6-14 did, the modern code limits the contribution to total shear strain of compression from dead load to a maximum of 3.0 at SLS. In clause 11.6.6.3.2, it also introduces a modified total shear strain check limiting total shear strain at SLS which was not present in prior versions: the total shear strain is limited to 5.0 rather than 5.5, and a factor of safety of 1.75 is introduced for the shear strain due to live load (CSA, 2019).

A variant of the design calculations was run for the Steeles Avenue bridge bearings, using the updated formulae from current codes for both the baseline and double-loading case. Unfortunately, some compromises had to be made: no information was available concerning the relative contribution of dead and live loads to the imposed rotation, θ. Only the total value was available. As a result, all rotation was assumed to be 100% due to live loads and 100% accounted for by SLS, since this is the most conservative assumption. Analogous assumptions were also made for imposed horizontal deflection, for similar reasons.

It was found that using the updated code provisions, neither loading case exceeded the maximum value of 3.0 for SLS shear strain due to dead load only: even for the case where a single bearing was taking the load for an entire girder, the value was only 1.54. However, due to the increased

factors on live load, the total shear strain under the double load case was 6.25 – 25% higher than the maximum provided for. This compares to a total shear strain value of 4.25 under the baseline loading case; which satisfies the code maximum of 5.0. It is noted that this was calculated using the most conservative assumptions possible.

These results may help to explain the timing of the bearing failure. Although the compressive load on the bearings could have been as much as double that calculated, they did not fail immediately when the bridge was loaded onto them – rather, they began to fail between the first and second inspection reports, between 1 and 4 months after installation. As per the previously discussed calculation, the bearings satisfied the requirement for maximum shear strain due to compressive dead load under SLS, even under a double loading condition. However, the bearings did not pass the total shear strain check with factored live loads under the double loading condition, which suggests that failure would occur over time as the bridge was subjected to traffic, temperature shifts, and other live loads.

No major inferences concerning vertical deflection could be made based on field observations at German Mills.

3.3.3 Unidentified liquid

In order to determine the causes and potential impacts of the unidentified liquid apparently seeping from the bearings, a number of key observations were made about the location and timing this behavior observed.

First, it was noted that all observed liquid appeared on bearings that had already suffered some degree of damage, specifically in that order. At German Mills a single bearing was noted as having

been damaged during installation, and that bearing was the only one observed to leak. At Steeles Avenue, careful observation of photos taken from early inspection reports showed that signs of damage appeared before the liquid was observed in all cases of damaged bearings. Further, as of the most recent site visit, the three most heavily damaged bearings all had evidence of liquid – however, a fourth bearing which had recently begun to exhibit delamination had no liquid. Neither of the undamaged bearings displayed any evidence of the liquid at all. This observation establishes that the leakage is not the primary cause of damage to the bearings.

Second, it was noted during which time intervals the liquid first appeared at Steeles Avenue. The first photographic evidence of the liquid occurred between the 2nd and 3rd inspection reports; between October 2019 and April 2021, while the first stain appeared between April and December 2021 ("407W-to-427S Bridge", 2021b). A second round of staining occurred between December 2021 and August 2022, and was observed during the site visit. Notably, all of these time intervals include the summer months, but not all of them include the winter months. The significance of that will be more apparent when discussing the fourth observation.

Third, it was noted that the liquid does not always remain liquid once it exits the bearing, instead solidifying. At German Mills, during the second site visit, it was observed that the liquid which had not been observed during the first site visit was still in liquid state, and was easily scraped off using the tip of a ruler. However, the older liquid had re-solidified, having a rubbery texture.

Fourth, it was noted that during the visits to the German Mills site, the temperature was very warm – 35 and 30 degrees Celsius, respectively. This, combined with the third observation, firmly

establishes that fresh liquid was appearing in the summer heat, rather than as a reaction to road salts or other chemicals which would be associated with the winter months.

Based on all of the above observations, it may be reasonably postulated that the observed liquid appears specifically when an already-damaged bearing is exposed to hot summer temperatures. These temperatures liquefy some material within the bearing, causing it to seep to the surface through the perforations left in the elastomer when the reinforcement either is damaged or delaminates from the surrounding material.

In an effort to determine what the unidentified liquid may be a brief examination of the existing literature concerning elastomer degradation was made. Based on a review of bin Samsuri (2010), most of the common methods of elastomer degradation could not result in a pattern of liquid such as the one observed in the manner it appeared. Oxidation or ozone attack would result in cracking of the elastomer, which was not observed. Heat-related failure of conventional NR rubber vulcanizates is stated to only become a concern at temperatures above 60 degrees Celsius, well beyond what the bearings experience. Oil absorption would have resulted in the fluid being identified prior to damage.

The only common method of damage that could conceivably produce this behavior based on the provided descriptions is water absorption, however, the descriptions are sufficiently ambiguous that this cannot be confirmed. Furthermore, water absorption is discussed primarily in the context of prolonged immersion, making it difficult to assess how this behavior would apply in the context of a non-immersed bearing. Finally, nothing about water absorption as a theory would explain why only previously damaged bearings were affected. Thus, while it cannot be

ruled out, it is not considered a likely explanation. However, there was mention in this text of an additional phenomenon known as wax blooming which merited further examination.

According to Nah and Thomas (1980), wax blooming can be identified by a thin layer of wax appearing on the surface of vulcanized rubber which has previously been impregnated with wax. It occurs when the temperature of the rubber falls during cooling after vulcanization, as the solubility of the wax within rubber is reduced at lower temperatures. This leads to wax supersaturation, and to it precipitating out. Field observations of the unidentified liquid do not match this description of wax blooming: the leakage seems to occur under higher temperatures rather than lower, and occurs irregularly at specific locations rather than creating a uniform layer over the rubber.

Given that the liquid's presence cannot be explained as conventional wax blooming or by most common methods of elastomer degradation, it is instead postulated that the liquid is associated with the bonding of the elastomer to the carbon fibre. This would suggest that while the liquid may not be the primary cause of damage, it may accelerate the delamination process once it has begun. However, this remains unconfirmed, as testing and identification of the leaking material was not available for this project. The precise details of the manufacturer's process and the formulation of the bonding agents were also unavailable. As a result, this is the limit of what could be determined about the observed liquid given available information.

4 In-Situ Data

4.1 Monitoring System

A number of sensors were installed at the Steeles Avenue site, including three Linear Variable Differential Transformer (LVDT) sensors at each of the six bearings, arranged as pictured in Figure 25 (D. MacDonald-Lockhart, Personal Communication, Sept. 15, 2021). The LVDT sensors measure displacement at a single point, in a single direction. Horizontal displacements could be read directly from the longitudinal sensor. Distances between the sensors and the edges of the girder shoe plate were measured and recorded for each sensor. Key measurements for these calculations are displayed in Table 13, where H indicates horizontal distance from the edge of the girder, and L indicates longitudinal distance to the face of the shoe plate, which itself has a length of 440 millimetres (D. MacDonald-Lockhart, Personal Communication, Sept. 15, 2021). For further information on bearing position and sensor layout, refer to Figure 20 in Section 3.2.1.

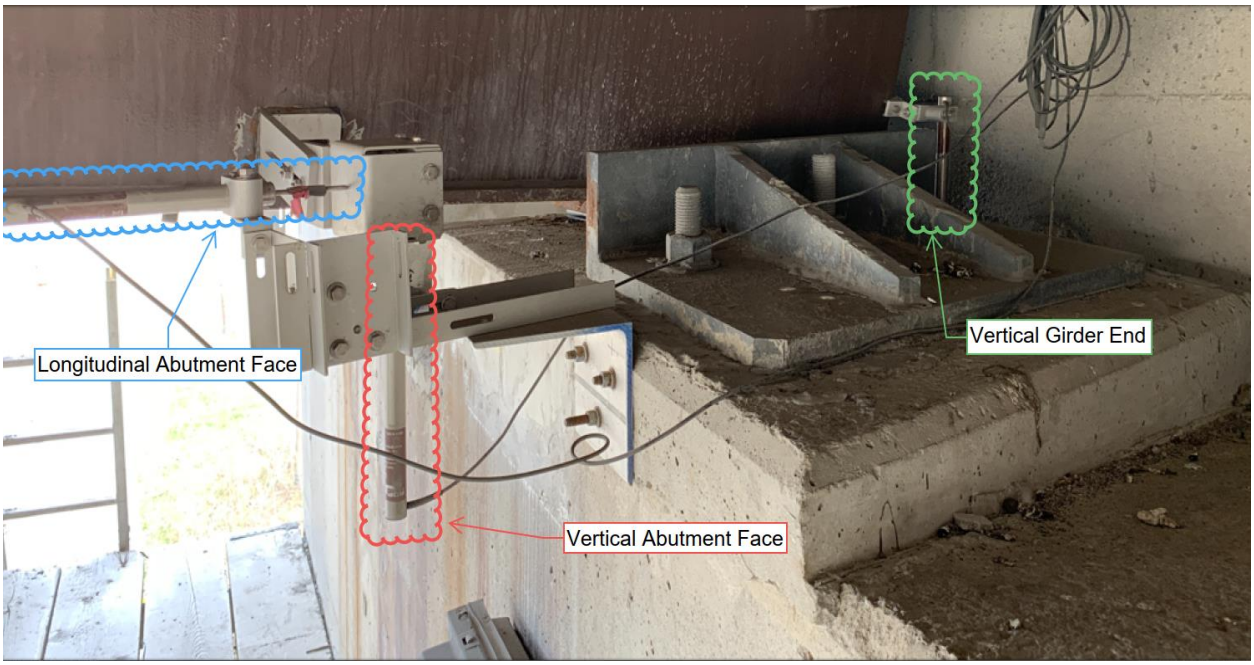

Figure 25: Sensor locations for Steeles Avenue site bearings (D. MacDonald-Lockhart, Personal Communication, Sept. 15, 2021)

	LVDT Orientation$_{Location}$					
Bearing	**Longitudinal**		**Vertical$_{interior}$**		**Vertical$_{exterior}$**	
	H	**L**	**H**	**L**	**H**	**L**
J1-E	205	370	205	350	55	25
J1-W	205	660	205	620	80	35
J2-E	170	400	170	365	55	30
J2-W	N/A		180	605	85	30
J3-E	165	390	165	345	55	10
J3-W	175	625	175	600	65	30

Table 13: Sensor locations for Steeles Avenue site bearings (D. MacDonald-Lockhart, Personal Communication, Sept. 15, 2021)

The system was installed between July and August of 2019, with reliable sensor data commencing at the end of August 2019 and continuing until September 2020. While the monitoring system

remained in place beyond September 2020, no further data could be obtained. Furthermore, as will be discussed later, a number of sensors had already gone offline by that time, indicating only a noise signal. It is noted that the monitoring system came online only after the bearings had been placed and loaded, and that initial deflections for the bearings were not recorded. As a result, these readings could not be used to estimate initial deformations or stresses in the bearings. However, they could be used to evaluate assumptions about the displacement of the bridge: if the variation in a given displacement parameter over the course of a year is substantially greater than that used in initial design calculations, this would indicate that the bearing experienced loads not accounted for during the design process. Identifying such unaccounted-for loading could give insight into why the bearings performed as they did. The data could also be used to assess the relative impact of traffic-related vibrations as compared to temperature fluctuation.

Sensors operated with a sampling rate off 100 Hz, and readings were recorded by the data acquisition system. The data acquisition system also collected 'trend' data from each sensor: the maximum, minimum, and average reading over each 5-minute time interval. This data was useful for analysis over longer time periods.

4.2 Data Processing

4.2.1 General

Data from the monitoring system was obtained in TDMS file format, which required the third-party program ConvertTDMS (Humphreys 2022) in order to convert the data to read into Matlab for further processing. Once the data had been input, additional processing was conducted to

remove extraneous metadata, perform necessary unit conversions to put all data into appropriate SI units, and append the data sequentially so that the contents of multiple files could be processed as a continuous data stream.

In addition, the mean values for all displacement quantities were set to zero over the time period under consideration. This was done as the initial displacement values for the sensors were not recorded, as previously discussed. It is noted that this step means the results from examining two different but overlapping time periods were not directly comparable – this limitation must be borne in mind for future analyses. Any data for which this process was not applied, or was applied differently, will be noted.

Once the initial sensor data had been processed in this manner, vertical displacements and rotations were calculated. Since the bearings were approximately centered under the shoe plate, which had known dimensions, the two vertical sensors could be used to calculate vertical displacement of the bearing based on an averaged value, taking into account the distance of each sensor from center of the shoe plate. Furthermore, the difference in vertical displacement between the two vertical sensors can be used to calculate rotation of the bearing. Since the component quantities had mean values of zero, these composite quantities also had mean values of zero.

4.2.2 Trend Data

In dealing with trend data, several additional data processing steps were necessary to account for the long timeframes under examination and vast number of files to be processed. A process was developed to address anomalous variations in file size and format, sensors temporarily

ceasing to function, which resulted in periods of 'noise', and random 'spikes' where a single data point was unrealistically high or low, postulated to be associated with power surges or similar interruptions in the data acquisition system. In the rare case that an error in or interruption to the data acquisition system resulted in a truncated or otherwise nonstandard data file, that file was discarded.

Periods of sensor inactivity, which appeared as periods of near-constant readings with only minor noise variation, were addressed by searching for sequences of data points that reside within a narrow range of parameters and setting all such data points to zero – as well as any calculated quantities determined from such data points. This made it easier to determine, in graphical form, when a sensor's data was invalid. It was found that 21 consecutive data points, ten to either side of a central value, was the minimum number required to ensure that this condition was not triggered by data produced by an active sensor. This indicated that brief interruptions to the sensor data would not trigger this condition, however, an interruption of an hour or two was considered negligible when entire months of data were being processed. Finally, individual outlier data points were identified via comparison to the previous data point based on slope, and subject to a number of preconditions to ensure that previously filtered-out noise signals and other multiple-point anomalies did not result in processing errors. The exact tolerance varied between sensor locations and was determined by examining the data over the course of a single 24-hour period and setting the tolerance for a given sensor to three times the largest variation observed between valid data points: that is, if two consecutive points had a difference greater than that between the lowest and highest data point during the sampled 24-hour period, it was assumed to be erroneous. While data may range more widely on some days than others, given

the limits to maximum vehicle weight and the long timescale of temperature-related motions, it was considered unlikely that this would remove any significant number of valid data points. Additionally, a counting function was implemented to identify the number of data points removed in this manner – any anomalously high value returned by this function was investigated further, to ensure that valid data was not being erroneously discarded.

4.2.3 Continuous data

As continuous data was examined over much shorter timeframes than trend data, the data did not generally need the same level of processing for anomalous files, outlier data points, or sections of noise due to signal interruptions. However, additional data processing was used to separate out the traffic-related motions from those related to temperature based on frequency.

In order to accomplish this, a set of Fast Fourier Transform (FFT) and Power Spectral Density (PSD) analyses was used to identify frequencies of interest using Welch's method (Mathworks, 2021).

In general, it was found that several peaks existed in the 0.1-25 Hz range, which were postulated to be associated with dynamic excitation. In addition, there was a noted response occurring at a frequency of less than 0.01 Hz, which was postulated to be associated with temperature effect throughout the day. It was also noted that the frequency content of all signals fell off at frequencies above 33 Hz, which was the result of the anti-aliasing filter. Specifically, the data acquisition equipment applied an 8 pole Butterworth filter with a point of either 60Hz – 3db, or 250Hz – 3db, depending on the sensor in question. In addition to this, the data processing software used in the acquisition system applied a digital low-pass filter at 50 Hz. (M. Torrie, Personal Communication, September 2021).

Based on this analysis, low pass and band pass filtering was conducted on the data. It was found that a low pass filter threshold of 0.03 Hz was most effective in capturing the temperature-related motions, while a band pass filter between 0.03 and 4 Hz was able to capture traffic-related induced motions. An examination of several data channels on various days found that more than 90% of all traffic-related motions, in terms of amplitude, are accounted for within that range. These filter functions are displayed in Figure 26. This is also visible on the FFT and PSD plots, where the peaks below 4 Hz rise in excess of a full order of magnitude beyond those which exist beyond 4 Hz, as can be seen in Figure 27 through 32.

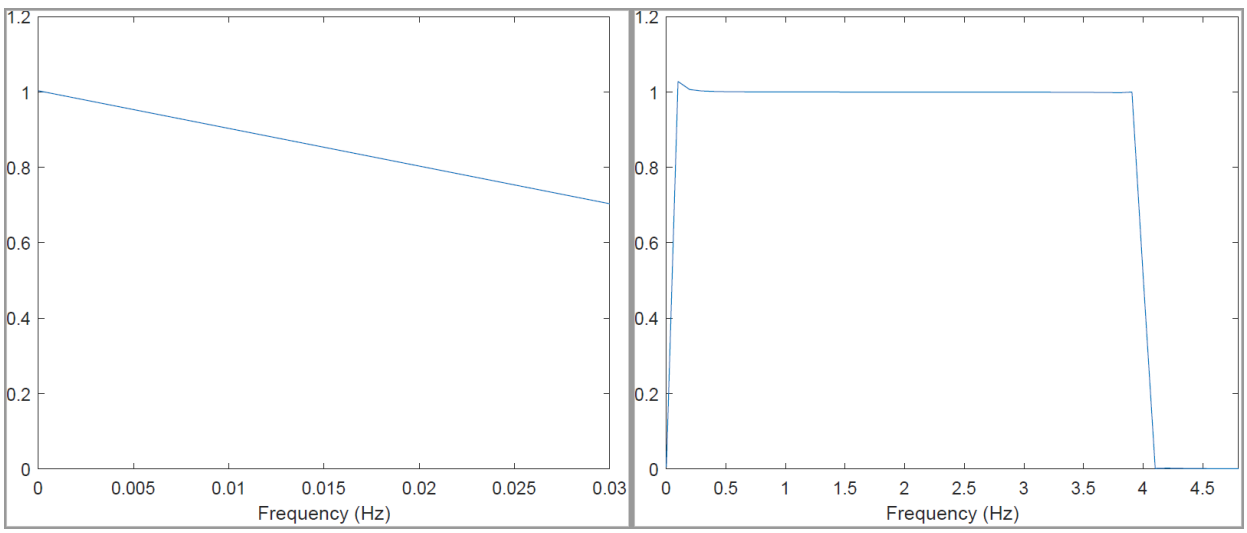

Figure 26: Filter functions – low-pass to capture temperature motions (left) and band pass to capture traffic motions (right)

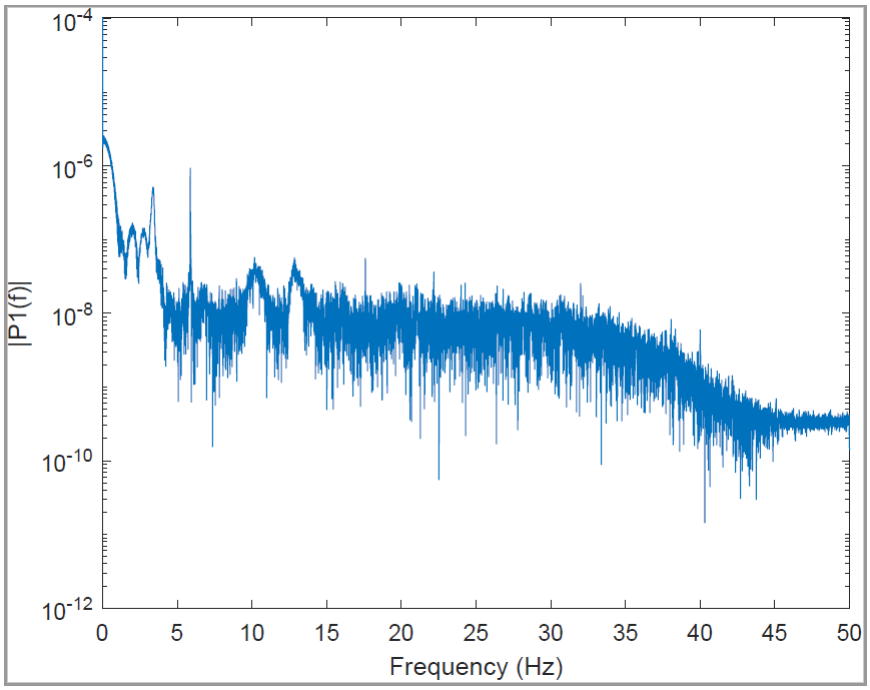

Figure 27: Fast Fourier Transform of rotations at bearing J2-E

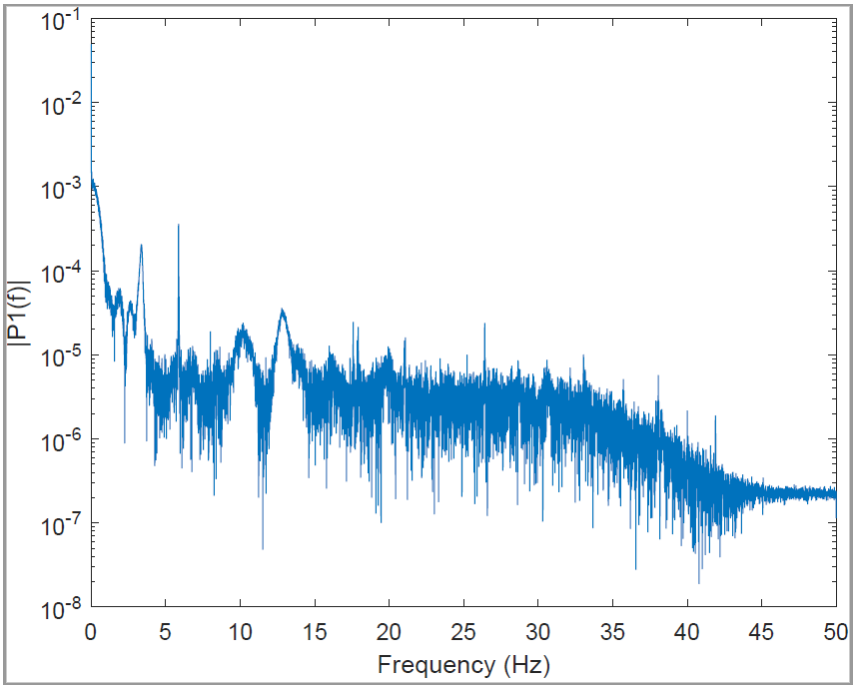

Figure 28: Fast Fourier Transform of vertical displacements at bearing J2-E

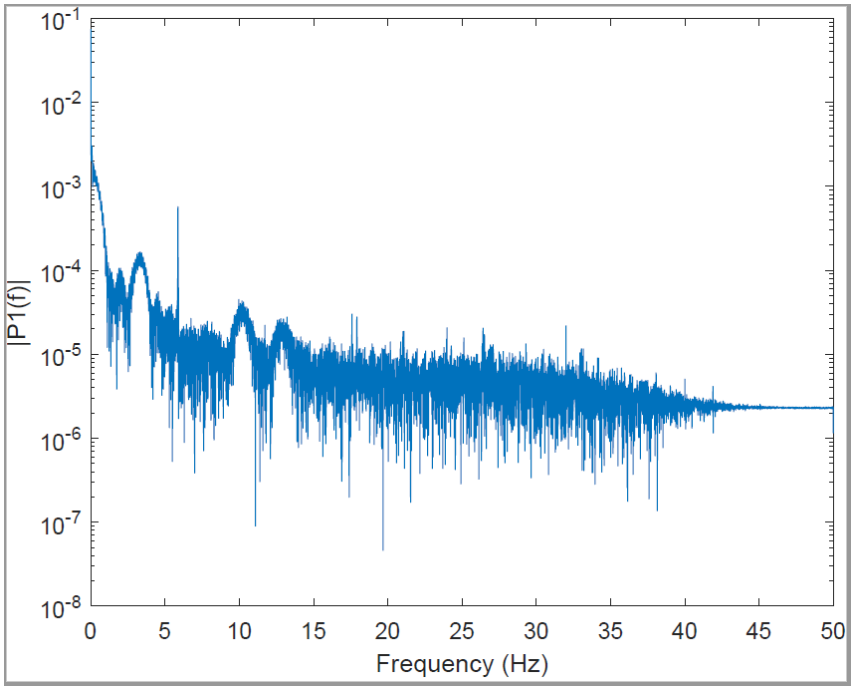

Figure 29: Fast Fourier Transform of horizontal displacements at bearing J2-E

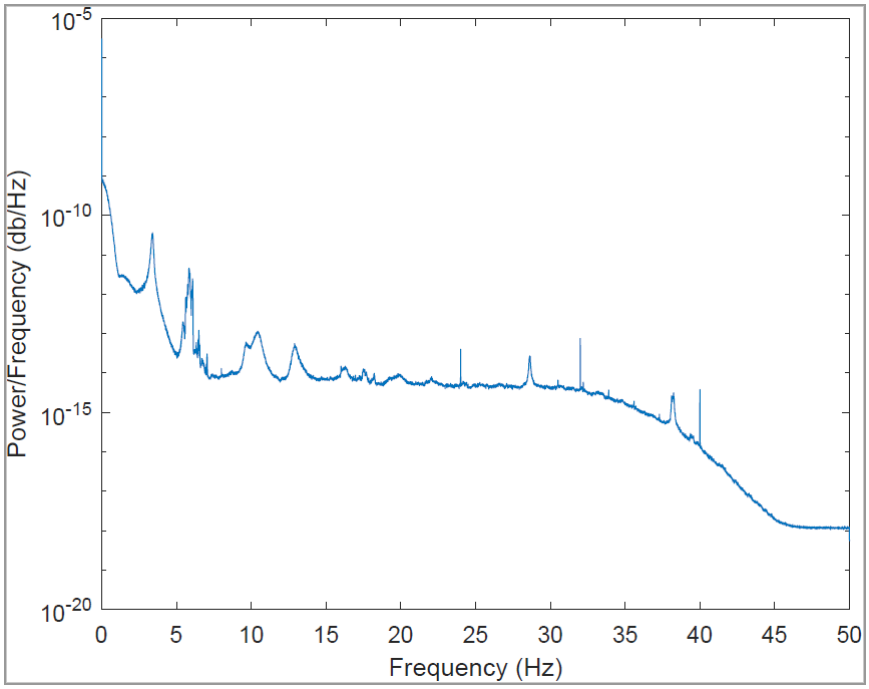

Figure 30: Power spectral density of rotations at bearing J2-E

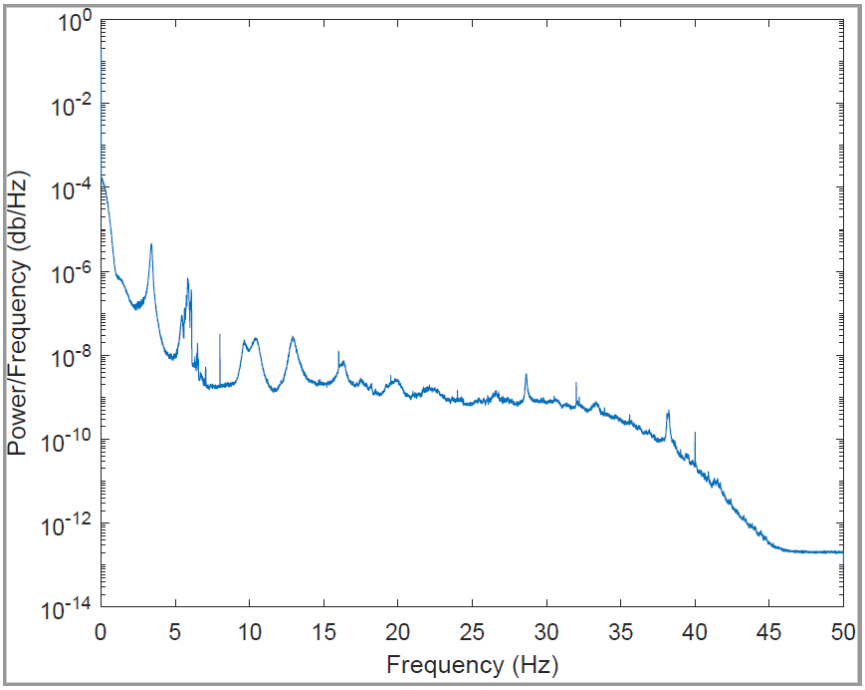

Figure 31: Power spectral density of vertical displacements at bearing J2-E

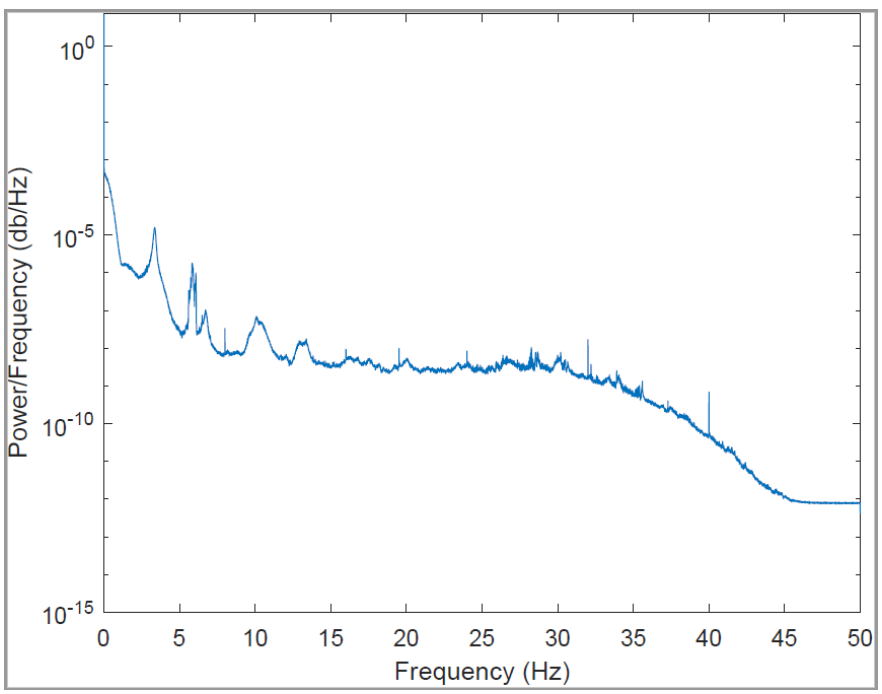

Figure 32: Power spectral density of horizontal displacements at bearing J2-E

4.3 Analysis

4.3.1 Continuous Data

In order to gain insight into the temperature and traffic dependency of various data quantities, an in-depth analysis was run for the continuous data obtained from October 10, 2019. Figures 33 through 35 show the variation in horizontal displacement, vertical displacement, and rotation for bearing J2-E, divided into traffic-related and temperature-related motions using frequency analysis as previously described. As was the case in the trend data section, while the analysis will discuss what was found for bearing J2-E specifically, all graphs examined show similar results (unless otherwise noted).

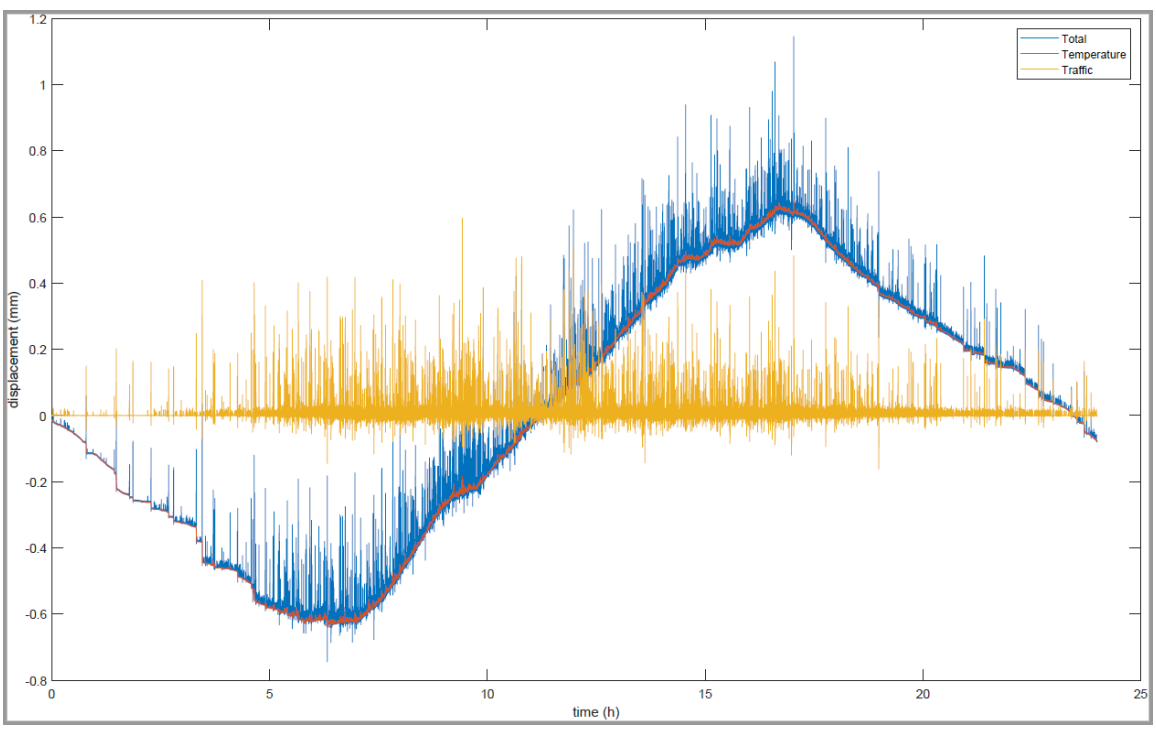

Figure 33: Horizontal displacement at bearing J2-E on October 10, 2019 – total, temperature, and traffic related motions

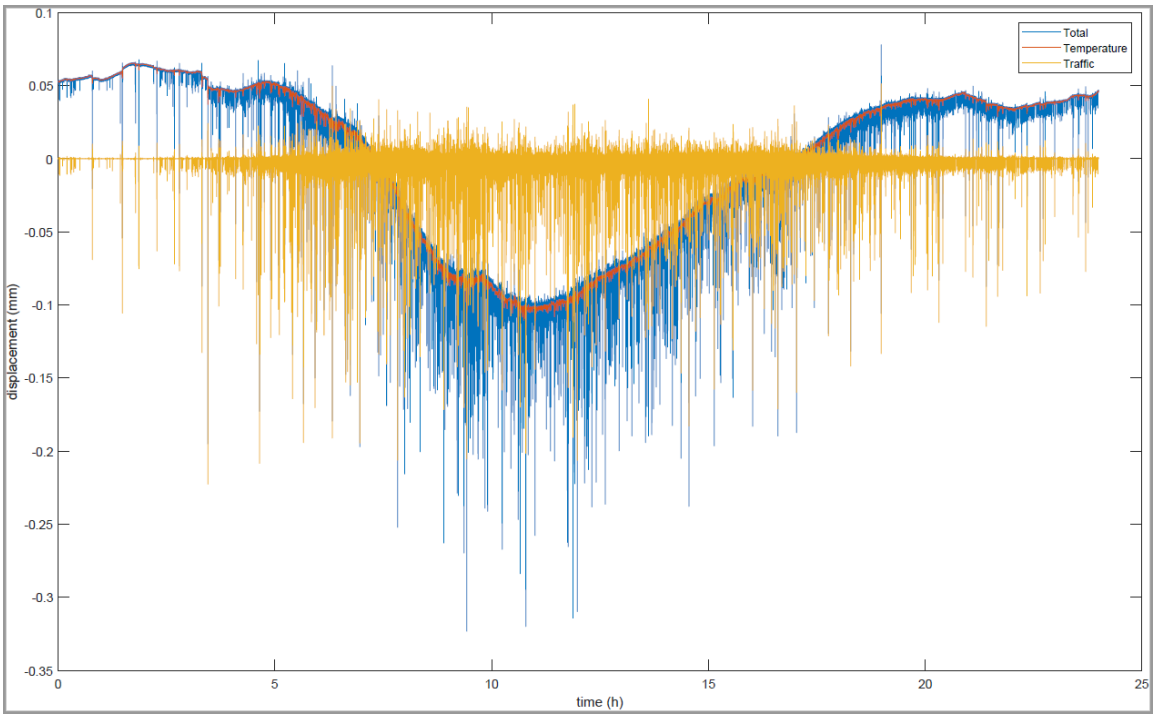

Figure 34: Vertical displacement at bearing J2-E on October 10, 2019 – total, temperature, and traffic related motions

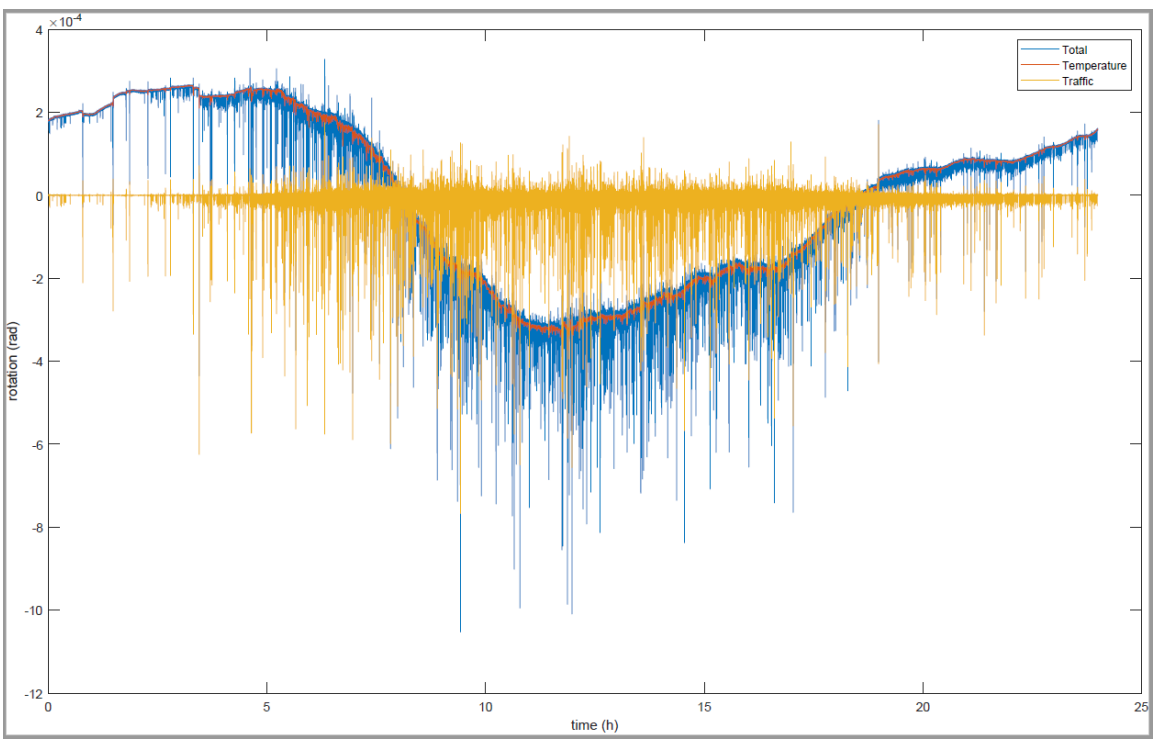

Figure 35: Rotation at bearing J2-E on October 10, 2019 – total, temperature, and traffic related motions

As shown in these figures, the horizontal displacement is less impacted by traffic-related motions relative to those related to temperature, while vertical displacement is more impacted. Specifically, on the day examined, traffic related motions account for a range of approximately 0.78 mm for horizontal displacement, 0.28 mm for vertical displacement, and 9.0×10^{-4} radians for rotation. The largest spikes in traffic related motion are assumed to be controlled by heavy trucks crossing the bridge, and the weight of such vehicles was not expected to be seasonally dependant. Temperature, meanwhile, accounted for ranges of approximately 1.25 mm for horizontal displacement, 0.16 mm for vertical displacement, and 5.5×10^{-4} radians for rotation. This, however, would be more variable between seasons – the data for a single day cannot be taken as representative for seasonal temperature effects.

Of particular note is the degree to which peaks in one direction (positive or negative) can be greater than those found in the opposite direction when examining traffic-related motions, particularly for vertical and horizontal displacement. This has implications when examining the design calculations related to these quantities, which will be done when discussing trend data. The most significant values are the portion of the traffic-related vertical displacement range accounted for by upward motion, which is approximately 0.05 mm, and the portion of the traffic-related horizontal displacement range accounted for by motion in the negative direction, which is approximately 0.16 mm.

4.3.2 Trend Data

A primary question that could be addressed using trend data was whether the loading estimates used in bearing design calculations, in particular applied displacements or rotations, were reflective of the actual motions undergone by the bridge structure. As previously discussed, the bearing design for Steeles Avenue was conducted considering a horizontal displacement of 2 mm and a rotation of 0.4 degrees (0.007 rad) at SLS, and that these quantities were assumed to also be indicative of ULS since no further data was available. Furthermore, design calculations indicated that a vertical displacement of approximately 2.0 mm was to be expected at ultimate limit state. Further calculations, carried out under the assumption of doubled vertical loading, predicted as much as 4.0 mm of vertical displacement.

In comparing these values to those seen in monitoring data, it was assumed that the provided horizontal displacement and rotation values indicate a range to either side of the mean quantity – that is; that a 2 mm displacement tolerance indicated a range from -2 to 2, or of 4 mm total. It was noted that the portion of vertical displacement related to dead load would remain fixed, while the portion related to live load would vary over time. As such, variation in the loading is indicative only of the live loads. To determine a reasonable range of variation for vertical displacement, calculations were performed to determine what the displacement would be under various loading cases. Under only SLS dead loads, the expected vertical displacement would be 0.7 mm, or 1.4 mm if double-loaded. Under SLS dead and live loads, the expected vertical displacement would be 1.3 mm, or 2.6 mm if double-loaded.

Based on the aforementioned values for vertical displacement under SLS dead, SLS total, and ULS total loads, it is postulated that the range of vertical displacement for a bearing would be approximately 0.6 mm if single-loaded with potential outliers of up to 1.3 mm if SLS loading conditions were exceeded, or approximately 1.2 mm if fully double-loaded with potential outliers of up to 2.7 mm if SLS loading conditions were exceeded. However, it is acknowledged that vibrations due to traffic loading may create uplift forces, counteracting part of the dead load imposed upon the bridge. As determined previously, approximately 0.05 mm of traffic-related vertical displacement was upward on a given sample day. Therefore, vertical displacement ranges approximately 0.05 mm greater than those previously calculated based on pure addition of loads may occur. It is also noted that if all of the dead load were to rest on a single bearing, this does not necessarily imply that all of the live load would also rest on that bearing – therefore, a vertical displacement range in line with the single-loaded case would not be in contradiction with the idea that bearing deterioration was caused by one bearing in a pair being more heavily loaded than the other. However, a vertical displacement range in line with a full double-load case would be confirmation of this scenario.

The primary run of trend data used for analysis extended from August 28, 2019 to February 29, 2020. This time interval was chosen based on several factors: the need to capture as wide of a temperature variation as possible, the desire to have a relatively long stream of uninterrupted data, and a preference for time intervals earlier in the monitoring period because sensors tended to go offline or otherwise become unreliable over time, rendering certain data channels unusable. The time interval in question covered a temperature variation of approximately 40 degrees Celsius (from 23° to -18°) over six months. Two bearings (J1-W and J2-E) had fully useable

data for all sensors throughout the entire monitoring period, with some additional sensors functioning continuously for other bearings. The full graphs for bearing J1-W are shown in Figures 36 through 38. Graphs for bearing J2-E during this monitoring period are displayed in Appendix A. They are similar to those for bearing J1-W, and all observations made with respect to the bearing J1-W graphs also apply to those for bearing J2-E.

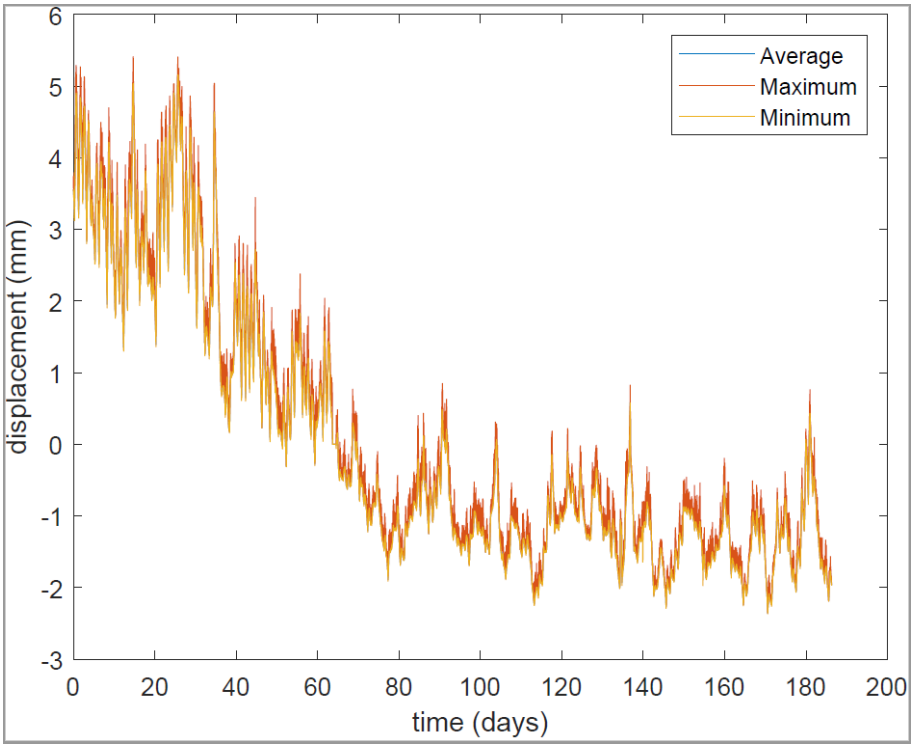

Figure 36: Horizontal displacement at bearing J1-W from August 29, 2019 to February 28, 2020

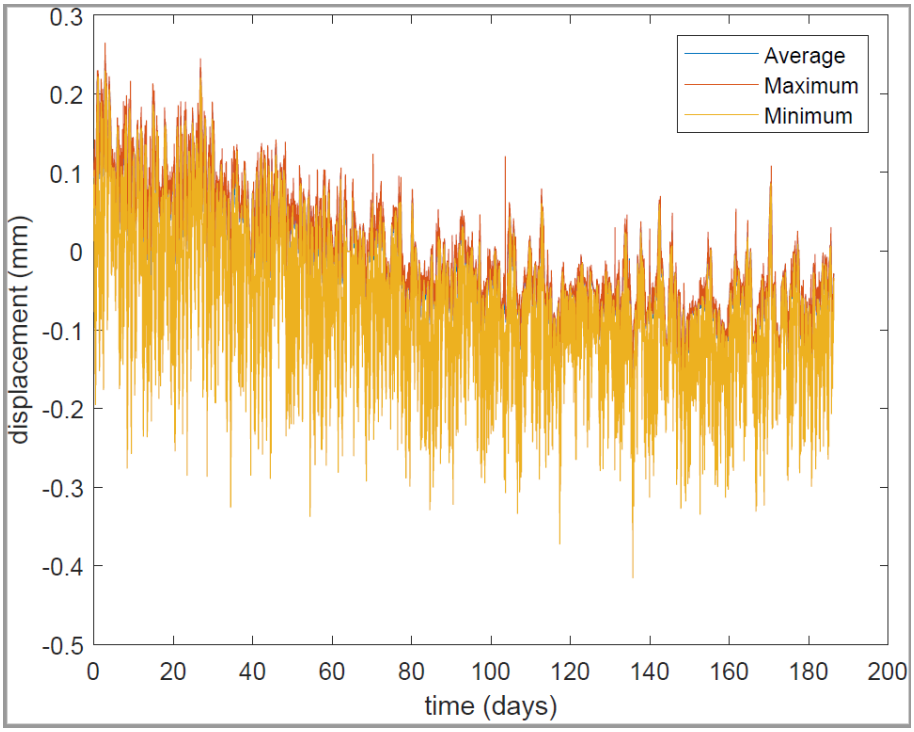

Figure 37: Vertical displacement at bearing J1-W from August 29, 2019 to February 28, 2020

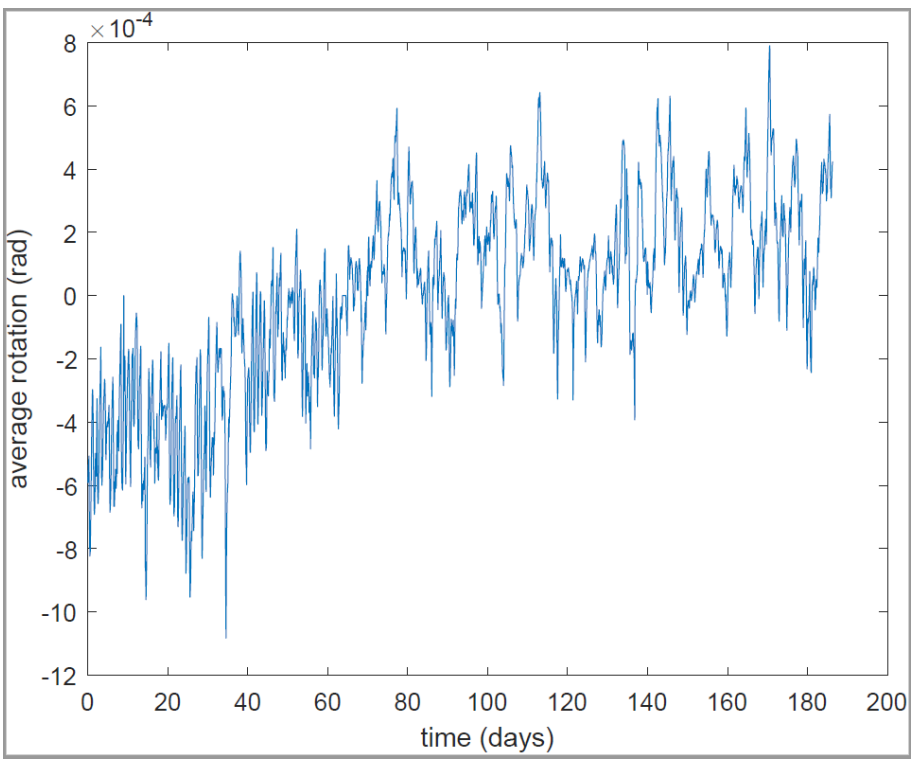

Figure 38: Average rotation at bearing J1-W from August 29, 2019 to February 28, 2020

It was observed that over the period in question, the two bearings for which full data was available experienced a horizontal displacement range of approximately 7.5 mm, a rotational range of approximately 0.002 radians (with slightly more variance between the bearings than the other quantities), and a vertical displacement range of approximately 0.68 mm. However, it is noted that bearings J1-W and J2-E exhibited no damage as of the final inspection report, while their 'partner bearings' were damaged – as such, these readings may be reflective of a relatively under-loaded bearing. For comparison, a set of graphs were selected from among the functioning sensors on visibly overloaded bearings: horizontal displacement from bearing J2-W, and vertical displacement and rotation from bearing J3-W. These are displayed in Figures 39 through 41. As these graphs show, the recorded displacements and rotations of visibly overloaded bearings do not substantially differ from those which are under reduced loading.

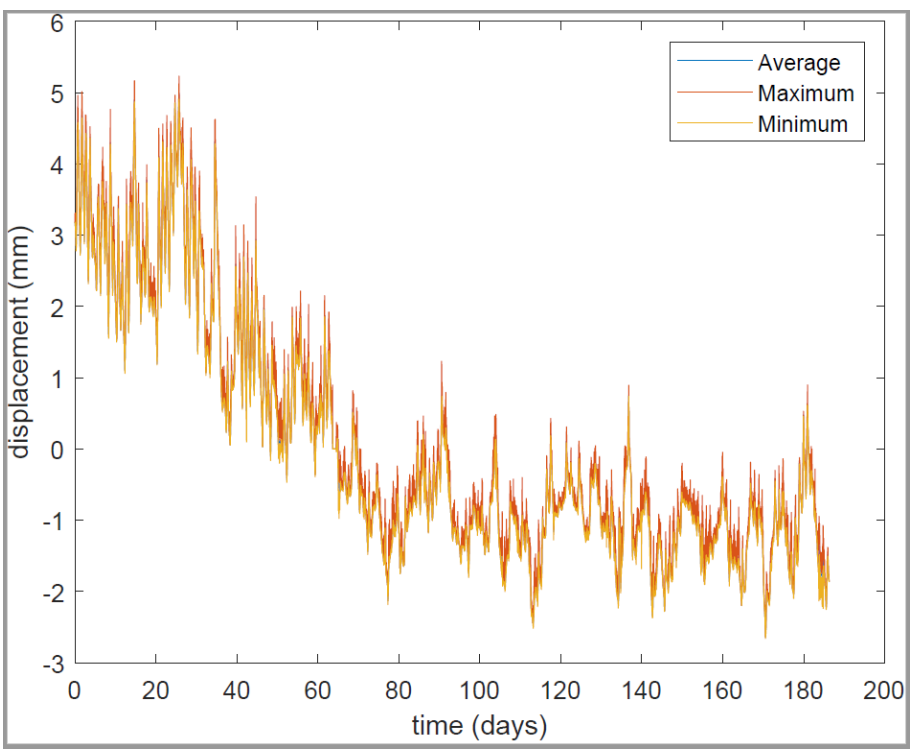

Figure 39: Horizontal displacement at bearing J2-W from August 29, 2019 to February 28, 2020

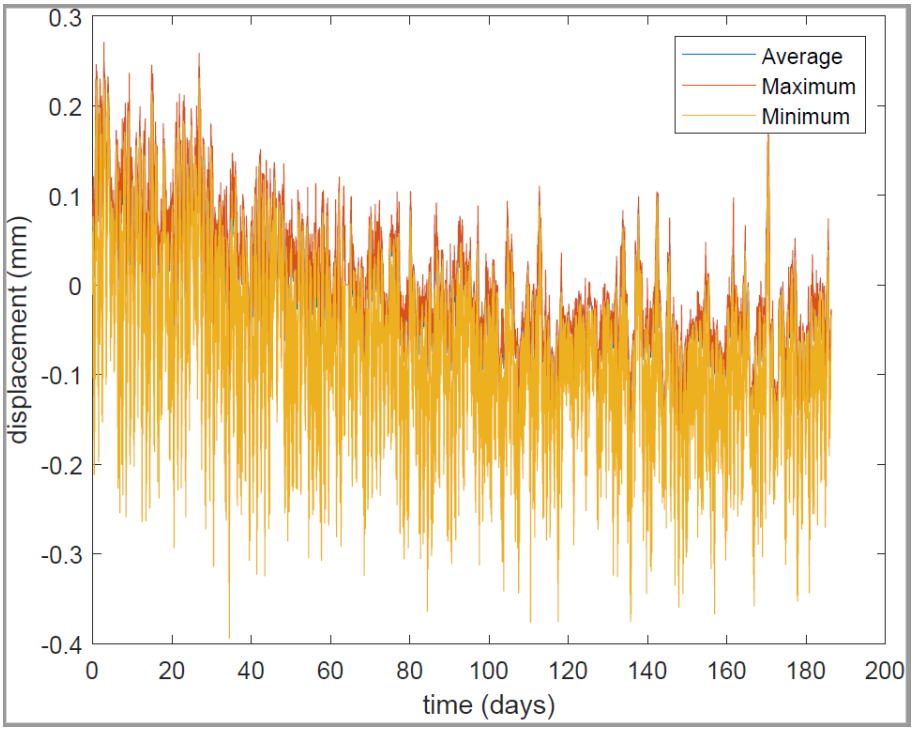

Figure 40: Vertical displacement at bearing J3-W from August 29, 2019 to February 28, 2020

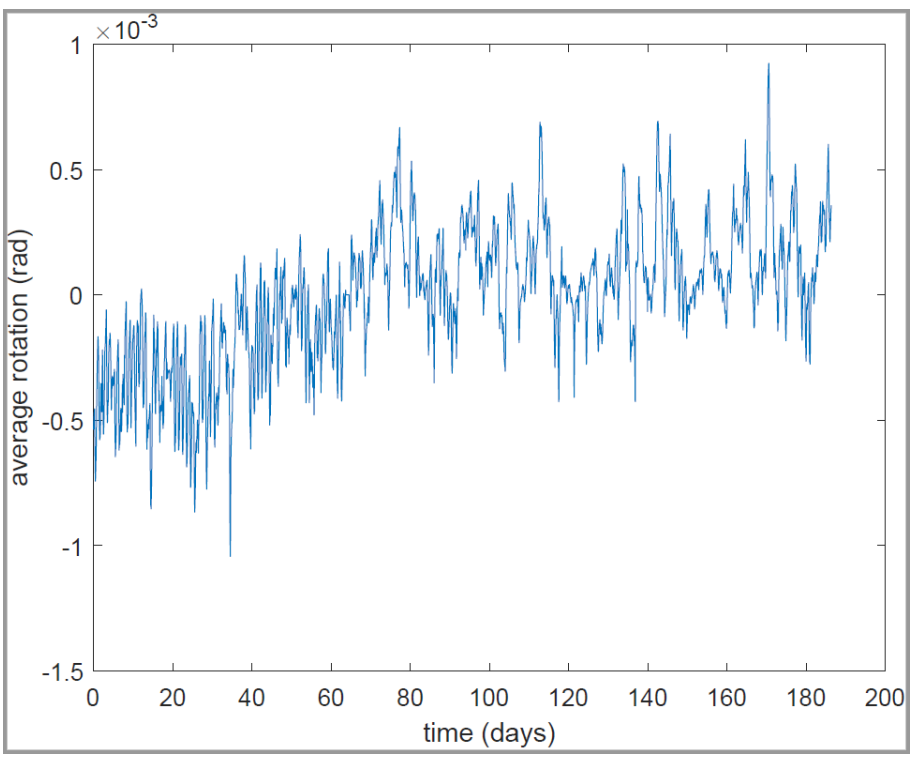

Figure 41: Average Rotation at bearing J3-W from August 29, 2019 to February 28, 2020

It is noted that all graphs show a gradual trend over the course of the monitoring period: in the positive direction for rotation, and in the negative direction for horizontal and vertical displacement. The time period under consideration shows the transition from summer to winter temperatures, which was postulated to be responsible for the trends observed. A second, longer time period was examined to confirm this, extending from August 28, 2019 to August 28, 2020. Full graphs for bearing J2-E during this monitoring period are displayed in Appendix B - it is noted that fewer sensors were functional over this longer time period, such that only the sensors at bearing J2-E produced usable data throughout the monitoring period. This is the reason it was not used for the prior analysis. It is also noted that all sensors went offline for a short time in June, around day 295. These graphs confirm that the observed trends are seasonal, as a time period covering the transition from winter to summer temperatures shows the opposite trends. An example of this is shown in Figure 42, which displays horizontal displacement at bearing J2-E.

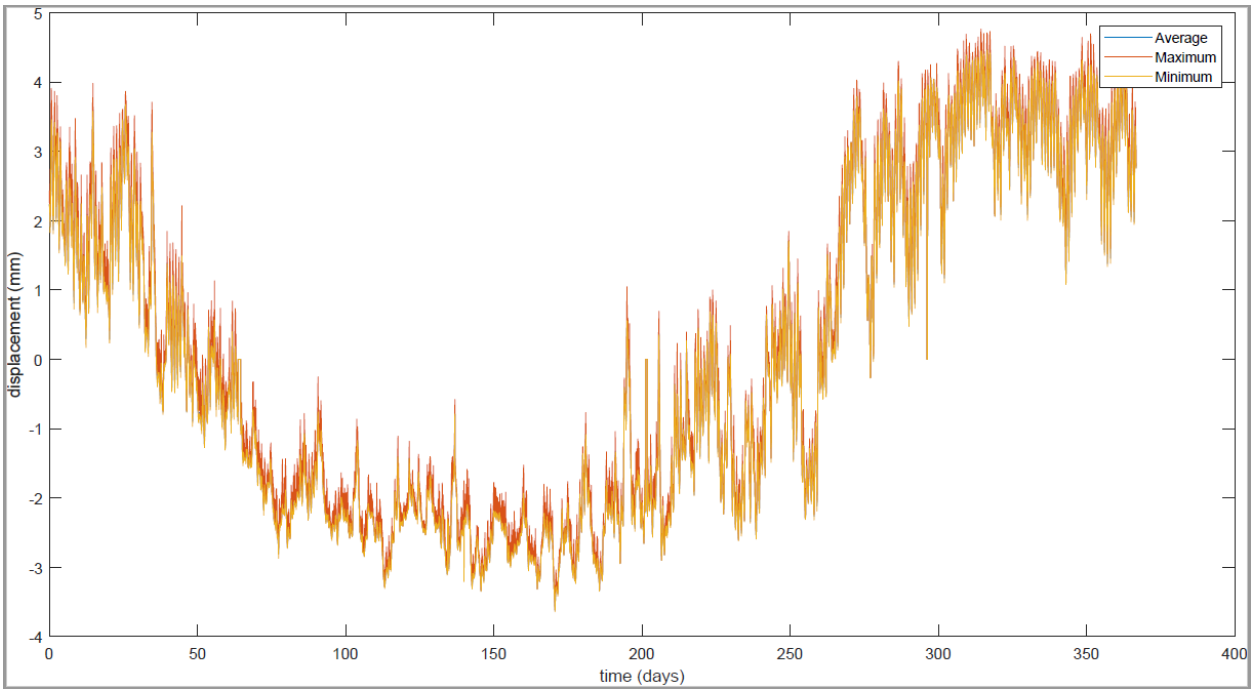

Figure 42: Horizontal displacement at bearing J2-E from August 28, 2019 to August 28, 2020

To further examine what influences long-period motions in the trend data, trend data for bearing J2-E was subjected to Fast Fourier Transform (FFT) and Power Spectral Density (PSD) analysis to identify frequency peaks. The first 100 points of a power spectral density for horizontal displacement at bearing J2-E is displayed in Figure 43. The later points were removed for visual clarity, as the primary motions under examination – daily, and annual – are extremely long-period. These graphs clearly show daily changes as a peak at approximately 1 day. While further peaks exist at higher frequencies, all are less than 5% of the magnitude. All remaining FFT and

PSD plots for bearing J2-E, displaying the first 100 points only, are included in Appendix C.

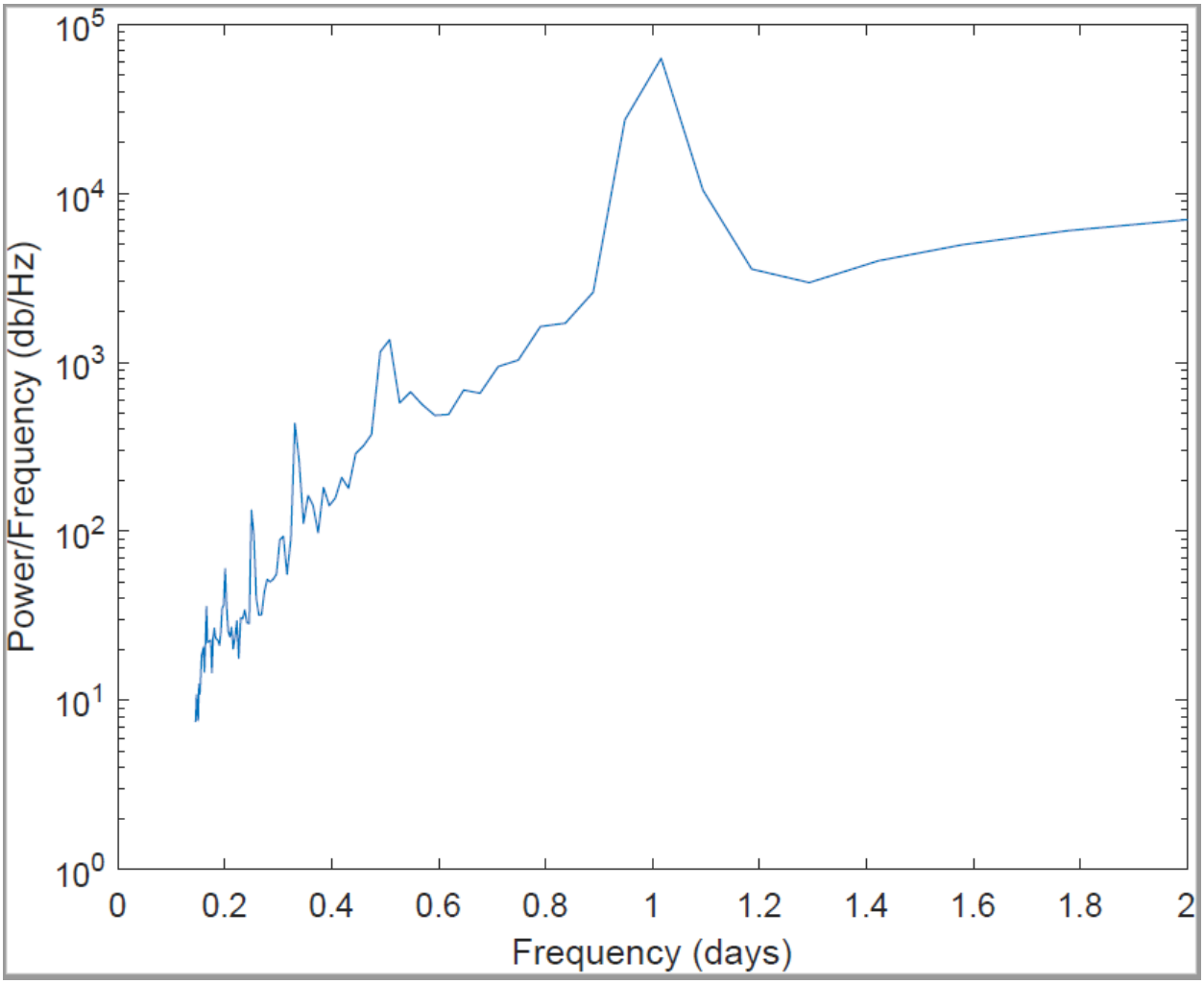

Figure 43: PSD analysis of horizontal displacement at bearing J2-E from August 28, 2019 to August 28, 2020

The variation in vertical displacement is relatively close to expectations: an observed range of 0.68 mm, where 0.6 mm was the expectation under SLS with an allowance of 0.05 mm due to traffic-related uplift, is within 5% of expectation. As this is in line with the SLS case, it would seem that although the dead load may have been unbalanced between bearings, the live load was divided fairly evenly.

Contrasting vertical displacement, the rotations and horizontal displacements recorded differ significantly from to the input design values: 7.5 mm horizontal displacement range far exceeds the ±2 mm used in the design process, and the observed 0.002 radian range for rotations is significantly less than the 0.007 radian range specified. Additional rotations for fabrication and tolerance may account for this discrepancy, as could permanent rotations imposed upon the bearing at the time of installation. It is furthermore noted that installation was conducted in the summer, under ambient temperatures of approximately 21° Celsius. This suggests that displacements due to seasonal variation would not be not equal in both directions.

4.3.3 Overall

In order to evaluate the impact of the previously discussed deviations from expected displacements, a new loading case was run for the Steeles Avenue design calculations. For this iteration, because there was no known inaccuracy in the assumed rotation, it was left unchanged. The assumed horizontal displacement was changed to 7mm, which was found to be the horizontal displacement due to temperature drop below installation temperature summed with the traffic contribution in that same direction.

It was noted that, across all observations made of the recorded data, the bearings experienced very similar displacement changes over the monitoring period. However, as previously described, monitoring data showed only the changes in displacements: initial displacements were not recorded. This would suggest that initial loading, consisting primarily of dead load, was unequal between the bearings while live loads were distributed more evenly – since, as previously discussed, there was a visible difference in how heavily loaded the bearings were. In accordance

with this hypothesis, the vertical loading was altered to include doubled SLS dead load values, while increases for every loading case beyond that point were maintained constant to reflect equal distribution of additional loading between the bearings. This load case was examined using both the original design procedure, and a variant using updated provisions from the 2019 version of CHBDC, as discussed in section 3.3.2.

When examined using the original design procedure, it was found that the vertical deflection criteria which was exceeded by 1% in the original design calculations, was exceeded by a full 35% under this loading scenario. Additionally, vertical pressures at all loading cases exceeded their manufacturer-recommended limits. The total shear strain check was still satisfied under the original design procedure – however, when examined using the updated design equations from more recent design code versions, the total shear strain check was exceeded with a value of 5.32; compared to the baseline value of 4.24 and the code limitation of 5.0.

It was observed that the increase to total shear strain was controlled primarily by the increased vertical compression, which added 0.77 to the total, while the factored shear strain due to increased horizontal displacement contributed only 0.31. It is also noted that this increased horizontal displacement allowance still falls within the guideline that bridge bearings should not exceed a horizontal displacement of $0.5t_r$ under serviceability loading states.

These exceedances are generally in line with, although less extreme than, those observed under the double loading scenario previously analysed. Therefore, the previous analysis in Section 3.3.2 of how observed failures correspond to the exceedances found for that loading condition remains

consistent: conclusions drawn from that loading scenario also apply to this loading scenario. A comparison of all three loading cases is shown in Table 14.

Design Parameter (Imposed/Allowable)	*Baseline Loading Scenario*	*Proposed Loading Scenario*	*Double Loading Scenario*
Vertical Deflection	1.01	1.35	2.02
Total Shear Strain	0.65	0.82	1.07
Total Shear Strain CHBDC clause 11.6.6.3	0.85	1.06	1.25
SLS Dead Load	0.72	1.44	1.44
ULS Total Load	0.96	1.29	1.92
Reinforcement Stress	0.23	0.31	0.46
Rotation	0.30	0.23	0.15

Table 14: Bearing performance under various loading cases for key design checks.

5 Conclusions & Recommendations

5.1 Summary

U-FREI were installed as bridge bearings in two highway bridges along the 407 ETR: one at Steeles Avenue, the other at German Mills Creek. At Steeles Avenue, two bearings were installed for each of three girders at the southern end of the bridge. At German Mills Creek, a single bearing was installed for each of six girders at the eastern end of the bridge.

At the German Mills Creek site, the bearings were known from the initial design calculation stage to be inadequate for the full rotational demands of the bridge as assessed by total shear strain, among other checks. This was necessary due to geometric constraints associated with the retrofitting, in particular a height limitation of 20 mm. Furthermore, one of the bearings was noted to have been damaged upon installation due to a defect in the support. Site visits conducted in the summer of 2022, more than 14 months after installation, revealed that a small amount of unidentified black liquid appeared to be seeping from one face of the damaged bearing. This liquid was noted to be fluid in some places, and to have solidified in others. All other bearings showed no signs of degradation or unusual behavior, and no bearings experienced delamination despite the anticipated rotational exceedances: whether the bearings ever experienced their full design rotation remains unknown.

Comparative design calculations carried out for SREI and U-FREI bearings demonstrated that U-FREI offered superior rotational performance to any SREI that could have been employed instead. The overall performance of U-FREI bearings at the German Mills Creek site supports the idea that

U-FREI are viable as bridge bearings, and a preferable alternative to SREI where rotations are high and vertical space is sharply limited.

At the Steeles Avenue site, the most accurate available calculations at the time they were first conducted indicated that vertical pressure on the bearings would exceed allowable levels by approximately 1%. This could not be improved due to geometric constraints associated with the retrofitting. Inspections carried out shortly after installation found that the loading was visibly unbalanced: at two of the three girders, one of the supporting bearings was visibly bulging outward while the other appeared to be lightly loaded. Subsequent inspection reports and site visits over the next two years showed a pattern of deterioration in three of the six bearings – one at each girder. This deterioration first progressed from localized to widespread delamination, followed by the appearance of unidentified black liquid on the surface of each bearing. This liquid was sufficient in quantity to spread to and visibly stain steel elements near one bearing. At one bearing, this deterioration further progressed to splitting apart of one bearing face where the elastomer had delaminated from the carbon fibre reinforcement.

Overall, it may be concluded that the SU-FREI bearings have shown good performance in-situ. At German Mills Creek, despite high rotational demands, only a single bearing displayed any sign of degradation, which was also known to have been damaged during installation. At the Steeles Avenue location, the observed bearing degradation has been shown to be directly attributable to and fully explicable by unanticipated high vertical pressures due to uneven load distribution, pressures which the bearings were not designed for.

The observed performance of SU-FREI bearings indicates that they are particularly useful where rotations exceed what a conventional SREI bearing could provide. This is primarily due to how thin the carbon fibre reinforcement layers are relative to steel reinforcement, which allows for a greater portion of the total height of the bearing to be taken up by elastomer. That same property also makes them particularly useful in situations where clearance height is limited, such as the retrofit cases at German Mills Creek and Steeles Avenue.

No major performance disadvantages compared to SREI have yet been identified. While there remains the matter of unidentified liquid, this occurred only in already-damaged bearings. Provided modern design criteria are satisfied, and that design is conducted based on accurate information with appropriate margin for error, SU-FREI have been shown to function well as bridge bearings.

5.2 Recommendations

The problems encountered by certain bearings at Steeles Avenue and German Mills Creek point to a number of important factors, which should be considered for future implementation of SU-FREI and elastomeric bearings in general. The first and most significant is that where multiple bearings are used to support a single bridge girder, it must be ensured that load is balanced between the bearings to avoid unanticipated overloading. It is noted that separate bearing supports, as a design configuration, are highly vulnerable to such imbalances even if standard OPSS tolerances are observed. This potential configuration should therefore be avoided if possible, and if it must be employed then tighter tolerances must be used. Additionally, for SU-FREI, it is clear that supports must be properly levelled: irregular bumps on the supports lead to

stress concentrations can which damage the bearing. While SU-FREI are fairly accommodating to horizontal displacements, being originally envisioned as seismic isolation devices, they can be more sensitive to inaccurate estimates of vertical or rotational loading.

5.3 Future Work

While the ability of SU-FREI to serve as bridge bearings is supported by the findings from this research, the fact remains that the unidentified liquid observed in damaged bearings remains largely unexplored. An in-depth investigation into this behavior is called for: to conclusively determine the identity of the substance, confirm the conditions under which it appears, and determine what impacts it may have on long-term bearing performance.

Despite the aforementioned uncertainty, the unidentified liquid has only been observed on bearings that were already damaged, while concrete advantages under large rotation and in limited spaces have been confirmed. Therefore, bearing in mind the previous statements of suitability of these bearings and recommendations for their implementation, SU-FREI can be recommended for use in bridge bearing applications. Achieving large-scale deployment, from this point forwards, is largely a matter of industry awareness and confidence rather than a question of suitability or utility.

6 References

407 ETR Concession Company Limited. (2020a) *407W-to-427S Bridge over Steel Ave Bearing Monitoring & Assessment Quarterly Report #1*. Unpublished internal company document.

407 ETR Concession Company Limited. (2020b) *407W-to-427S Bridge over Steel Ave Bearing Monitoring & Assessment Quarterly Report #2*. Unpublished internal company document.

407 ETR Concession Company Limited. (2021a) *407W-to-427S Bridge over Steel Ave Bearing Monitoring & Assessment Quarterly Report #3*. Unpublished internal company document.

407 ETR Concession Company Limited. (2021b) *407W-to-427S Bridge over Steel Ave Bearing Monitoring & Assessment Quarterly Report #4*. Unpublished internal company document.

Al-Anany, Y. (2016). *Fiber Reinforced Elastomeric Isolators for Bridge Applications* [Unpublished doctoral dissertation]. McMaster University.

Al-Anany, Y., & Tait, M. J. (2017a). "Fiber reinforced elastomeric isolators for the seismic isolation of bridges". *Compos. Struct.*, 160: 300-311.

Al-Anany, Y., & Tait, M. J. (2017b). "Experimental assessment of utilizing fiber reinforced elastomeric isolators as bearings for bridge applications". *Compos. B. Eng.*, 114: 373-385.

Angeli, P., Russo, G., and Paschini, A. (2013). "Carbon fiber-reinforced rectangular isolators with compressible elastomer: Analytical solution for compression and bending." *Int. J. Solids Struct., 50(22)*, 3519–3527.

Bao, Y., Becker, T. C., Sone, T., & Hamaguchi, H. (2017). "Experimental study of the effect of restraining rim design on the extreme behavior of pendulum sliding bearings". *Earthquake Engng Struct Dyn;* 47:906–924.

bin Samsuri, A. (2010). Degradation of Natural Rubber and Synthetic Elastomers. In B. Cottis, M. Graham, R. Lindsay, S. Lyon, T. Richardson, D. Scantlebury, & H. Stott (Eds.), *Shreir's Corrosion, Fourth Edition* (vol. 3, pp. 2407-2438). Elsevier.

Brad Humphreys (2022). ConvertTDMS (v10) (https://github.com/humphreysb/ConvertTDMS), GitHub. Retrieved July 5, 2021.

Canadian Standards Association. (2014). *Canadian highway bridge design code (CAN/CSA Standard No. S6-14)*. Retrieved from https://view-csagroup-org.libaccess.lib.mcmaster.ca/yDqjaR

Canadian Standards Association. (2019). *Canadian highway bridge design code (CAN/CSA Standard No. S6-19)*. Retrieved from https://view-csagroup-org.libaccess.lib.mcmaster.ca/EmUZ42

Canam bridges. (2010). *Goodco Z-Tech - Elastomeric bearings*. Retrieved from https://www.canambridges.com/wp-content/uploads/2015/07/goodco-z-tech-elastomeric-bearings.pdf

De Raaf, M. (2009). *Experimental Study of Unbonded Fiber Reinforced Elastomeric Bearings*. [Unpublished masters thesis], McMaster University.

De Raaf, M. G. P., Tait, M. J., & Toopchi-Nezhad, H. (2011). "Stability of fiber-reinforced elastomeric bearings in an unbonded application". *Journal of Composite Materials, 45(18)*, 1873-1884.

Foster, B. (2011). *Base Isolation using Stable Unbonded Fibre Reinforced Elastomeric Isolators (SU-FREI)*. [Unpublished master's thesis]. McMaster University.

Google, Maxwell Technologies, Landsat/Copernicus. (n.d.). [Arial view of greater Toronto area]. Retrieved September 7, 2022, from Google Earth Pro.

Kelly, J. M. (1999). "Analysis of Fiber-Reinforced Elastomeric Isolators". *Journal of Seismology and Earthquake Engineering,* 2(1), 19-34.

Kelly, J. M., & Konstantinidis, D. (2009). "Effect of friction on unbonded elastomeric bearings". *Journal of Engineering Mechanics, 135(9)*, 953-960.

Kelly, J. M., & Konstantinidis, D. (2011). *Mechanics of Rubber Bearings for Seismic and Vibration Isolation.* John Wiley & Sons, Incorporated.

Kelly, J. M., & Takhirov, S. M. (2001). "Analytical and Experimental Study of Fiber-Reinforced Elastomeric Isolators". *Pacific Earthquake Engineering Research Center, Univ. of California, Berkeley*. PEER Report No. 2001/11.

Kelly, J. M., & Takhirov, S. M. (2002). "Analytical and Experimental Study of Fiber-Reinforced Strip Isolators". *Pacific Earthquake Engineering Research Center, Univ. of California, Berkeley*. PEER Rep. No. 2002/11.

Kelly, J. M., and Van Engelen, N. C. (2015a). "Single series solution for the rectangular fiber-reinforced elastomeric isolator compression modulus." *Pacific Earthquake Engineering Research Center, Univ. of California, Berkeley*. PEER Report No. 2015/03

Kelly, J. M., and Van Engelen, N. C. (2015b). "Fiber-reinforced elastomeric bearings for vibration isolation." *J. Vibr. Acoust., 138(1)*, 011015.

Mathworks. (2021). *MATLAB — Functions*. Mathworks Help Center. https://www.mathworks.com/help/matlab/referencelist.html?type=function&s_tid=CRUX_topnav.

Moon, B., Kang, G., Kang, B., & Kelly, J. M. (2002). "Design and manufacturing of fiber reinforced elastomeric isolator for seismic isolation". *Journal of Materials Processing Technology, 130-131*, 145-150. doi:10.1016/S0924-0136(02)00713-6

Nah, S. H., and Thomas, A. G (1980). "Migration and Blooming of Waxes to the Surface of Rubber Vulcanizates" *Journal of Polymer Science: Polymer Physics Edition, Vol. 18,* 511-521.

Ontario Provincial Standards Specification. (2020). *Construction Specification for Installation of Bearings* (OPSS.PROV 922). The Road Authority. https://www.roadauthority.com/Standards/

Osgooei, M. P., Tait, M. J., & Konstantinidis, D. (2013). "Three-dimensional finite element analysis of circular fiber-reinforced elastomeric bearings under compression". *Compos. Struct.*, 108 (2014), 191–204.

Ramberger G. (2002). *Structural bearings and expansion joints for bridges.* IABSE.

Russo, G., & Pauletta, M. (2012). "Sliding instability of fiber-reinforced elastomeric isolators in unbonded applications". *Engineering Structures, 48*, 70-80.

Stephen (2022). Natural-Order Filename Sort (https://www.mathworks.com/matlabcentral/fileexchange/47434-natural-order-filename-sort), MATLAB Central File Exchange. Retrieved April 16, 2022.

Tait, M. J. (2018). *Bearing Design calculations: Steeles Avenue and German Mills Creek Bridges*. Unpublished Mathcad worksheets.

Toopchi-Nerzad, H., Tait, M. J., & Drysdale, R. G. (2011). "Bonded versus unbonded strip fiber reinforced elastomeric isolators: Finite element analysis". *Compos. Struct.*, 93 (2011), 850–859.

Toopchi-Nezhad, H. (2008). *Stable Unbonded Fiber Reinforced Elastomeric Isolators*. [Unpublished doctoral thesis], McMaster University.

Toopchi-Nezhad, H., Tait, M. J., & Drysdale, R. G. (2008). "Testing and modeling of square carbon fiber-reinforced elastomeric seismic isolators". *Structural Control and Health Monitoring, 15(6)*, 876-900.

Tsai, H. C., & Kelly, J. M. (2001). "Stiffness analysis of fiber reinforced elastomeric isolators.", *Pacific Earthquake Engineering Research Center, Univ. of California, Berkeley*. PEER Rep. No. 2001/05

Tsai, H., & Kelly, J. M. (2002). "Stiffness analysis of fiber-reinforced rectangular seismic isolators". *Journal of Engineering Mechanics, 128(4)*, 462-470.

Van Engelen, N. C., & Kelly, J. M. (2014). "Correcting for the Influence of Bulk Compressibility on the Design Properties of Elastomeric Bearings". *J. Eng. Mech.*, 141(6), 04014170.

Van Engelen, N. C., Konstantinidis, D., & Tait, M. J. (2017). "Simplified approximations for critical design parameters of rectangular fiber-reinforced elastomeric isolators". *J. Eng. Mech., 143(8)*: 06017009.

Van Engelen, N. C., Tait, M. J., & Konstantinidis, D. (2012, Sept. 24-28). *Horizontal Behaviour of Stable Unbonded Fiber Reinforced Elastomeric Isolators (SU-FREIs) with Holes,* [Paper Presentation]. 15th World Conference on Earthquake Engineering, Lisbon, Portugal.

Van Engelen, N. C., Tait, M. J., & Konstantinidis, D. (2016). "Development of design code oriented formulas for elastomeric bearings including bulk compressibility and reinforcement extensibility". *Journal of Engineering Mechanics, 142(6)* doi:10.1061/(ASCE)EM.1943-7889.0001015

Van Galen, Z., Torrie, M. (2022, July 19-22). *Field Study of Stable Unbonded Fiber Reinforced Elastomeric Bearings* [Conference Presentation]. SMSB 2022, Toronto, ON, Canada.

Van Galen, Z., Torrie, M., MacDonald-Lockhart, D., Tait, M. (2022). "Field Study of Stable Unbonded Fiber Reinforced Elastomeric Isolators". [Not yet published].

Appendix A

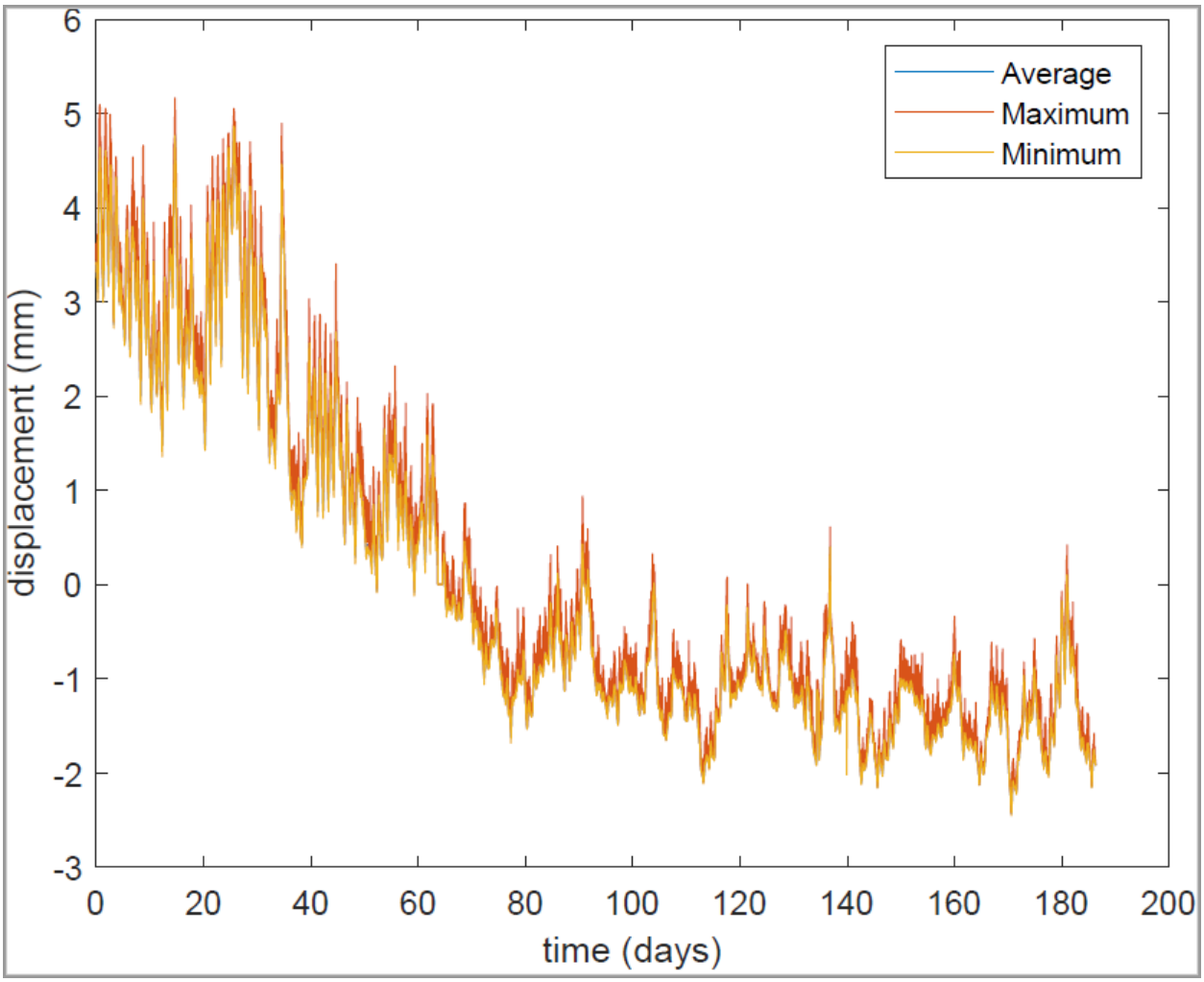

Figure A 1: Horizontal displacement at bearing J2-E from August 29, 2019 to February 28, 2020

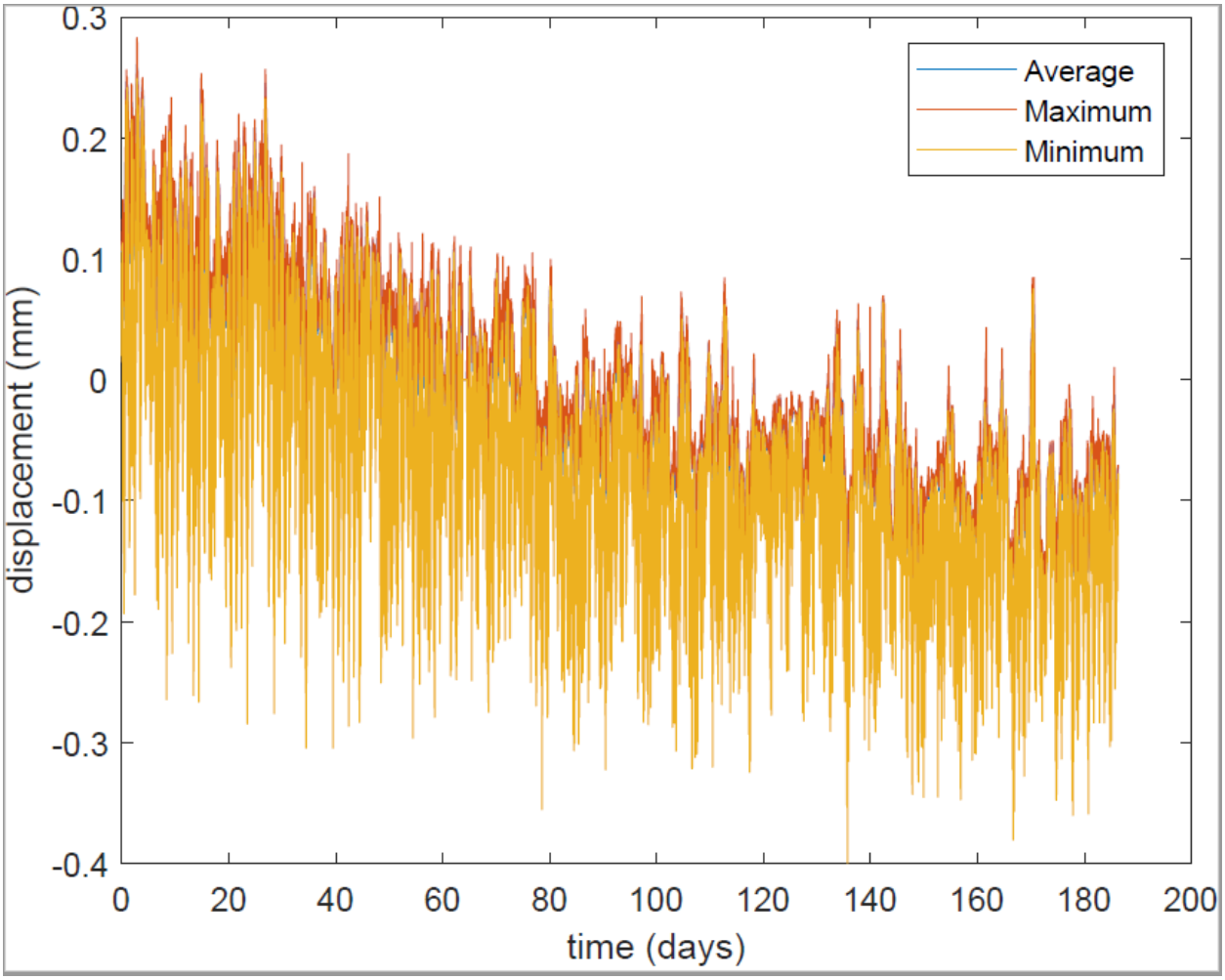

Figure A 2: Vertical displacement at bearing J2-E from August 29, 2019 to February 28, 2020

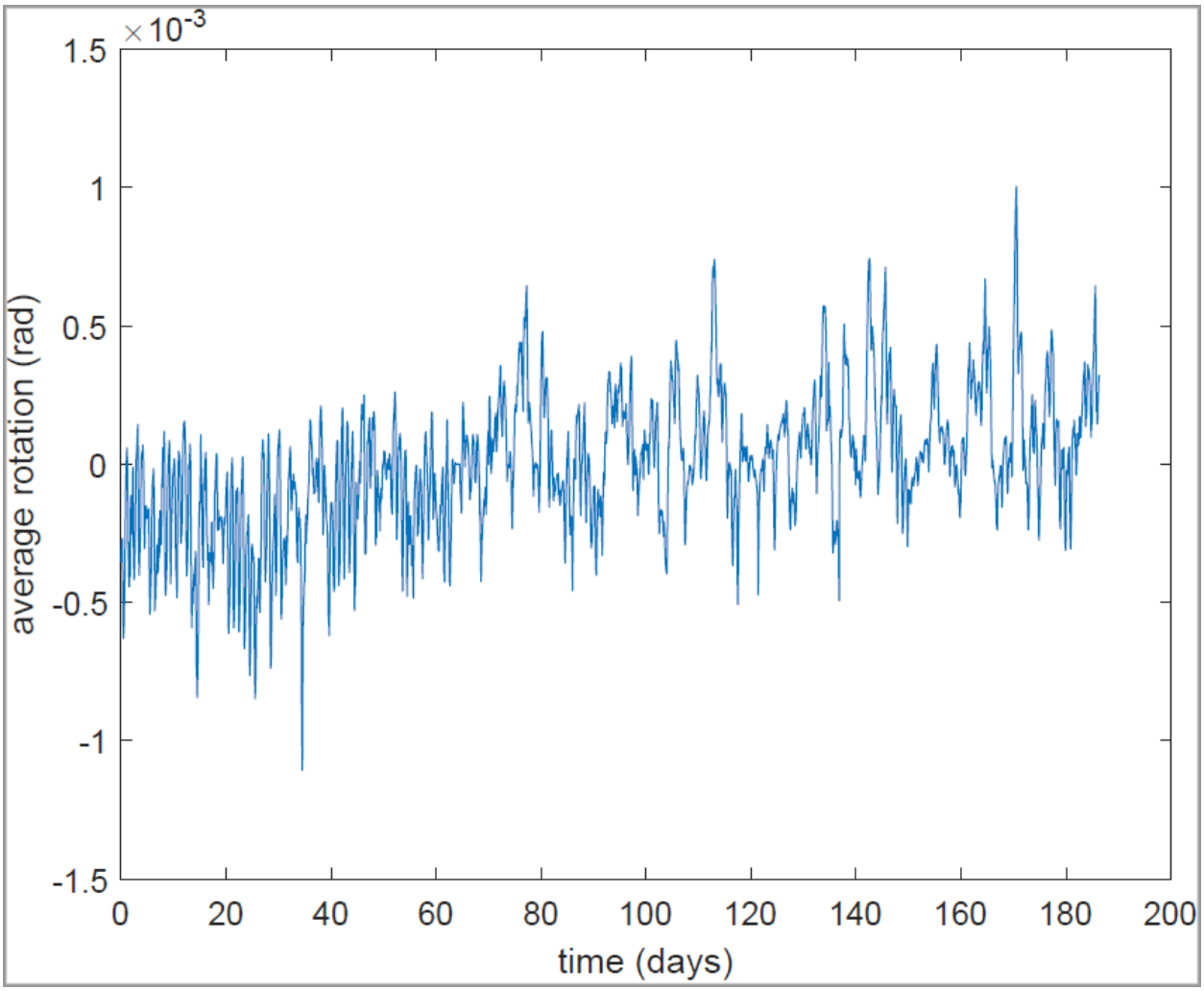

Figure A 3: Average rotation at bearing J2-E from August 29, 2019 to February 28, 2020

Appendix B

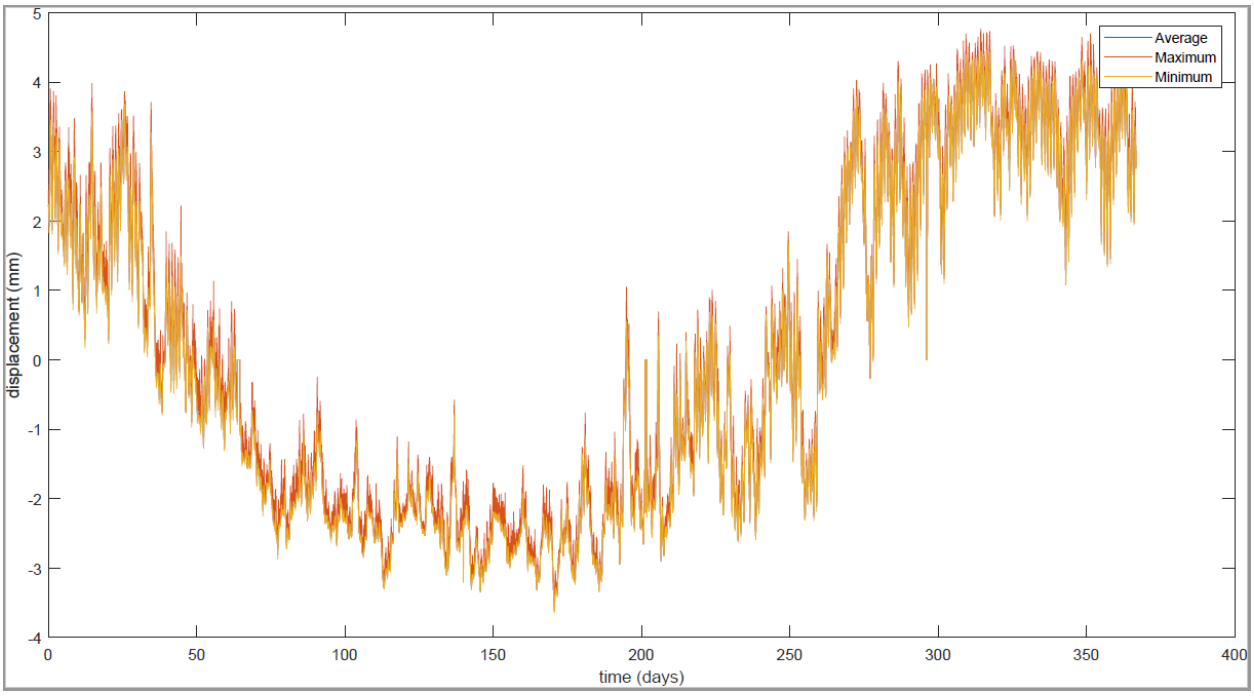

Figure B 1: Horizontal displacement at bearing J2-E from August 28, 2019 to August 28, 2020

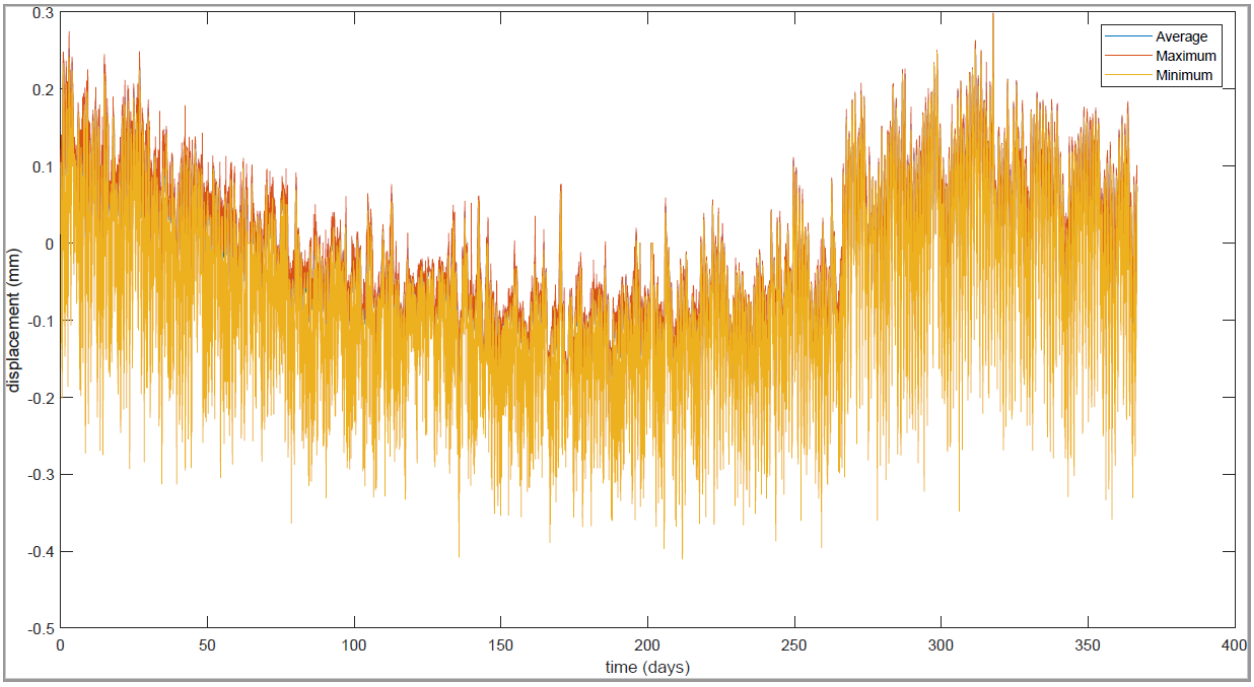

Figure B 2: Vertical displacement at bearing J2-E from August 28, 2019 to August 28, 2020

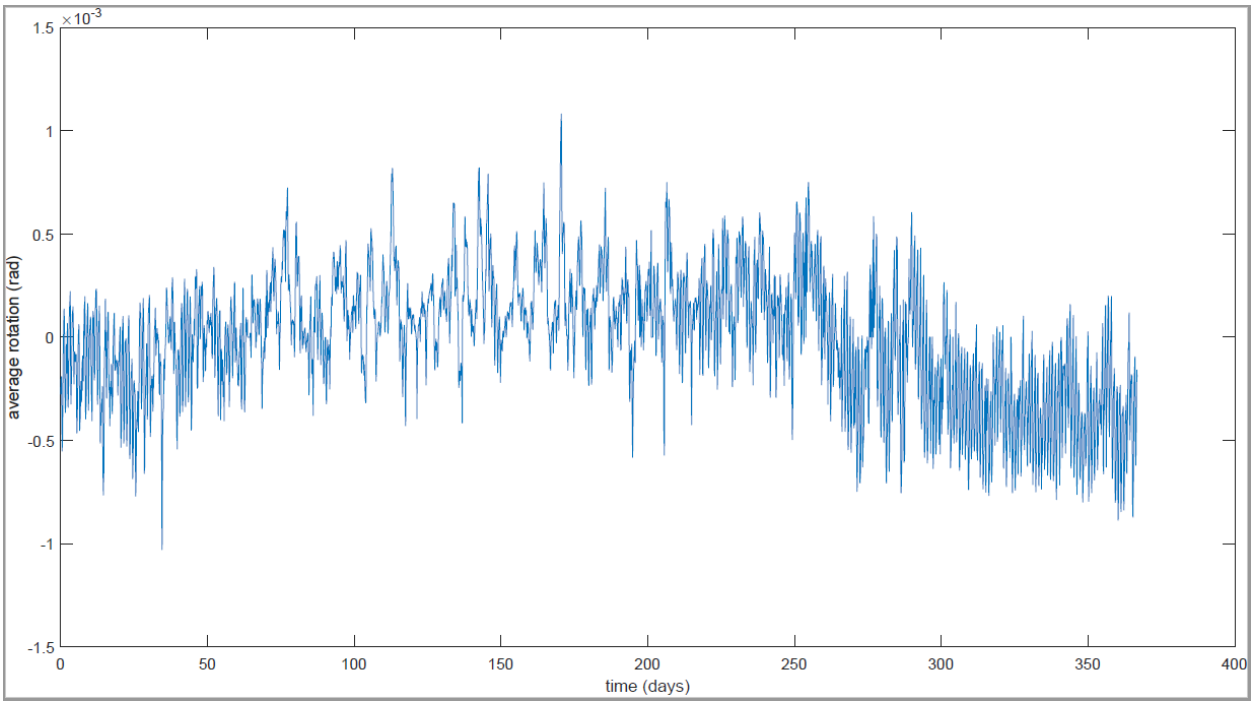

Figure B 3: Average rotation at bearing J2-E from August 28, 2019 to August 28, 2020

Appendix C

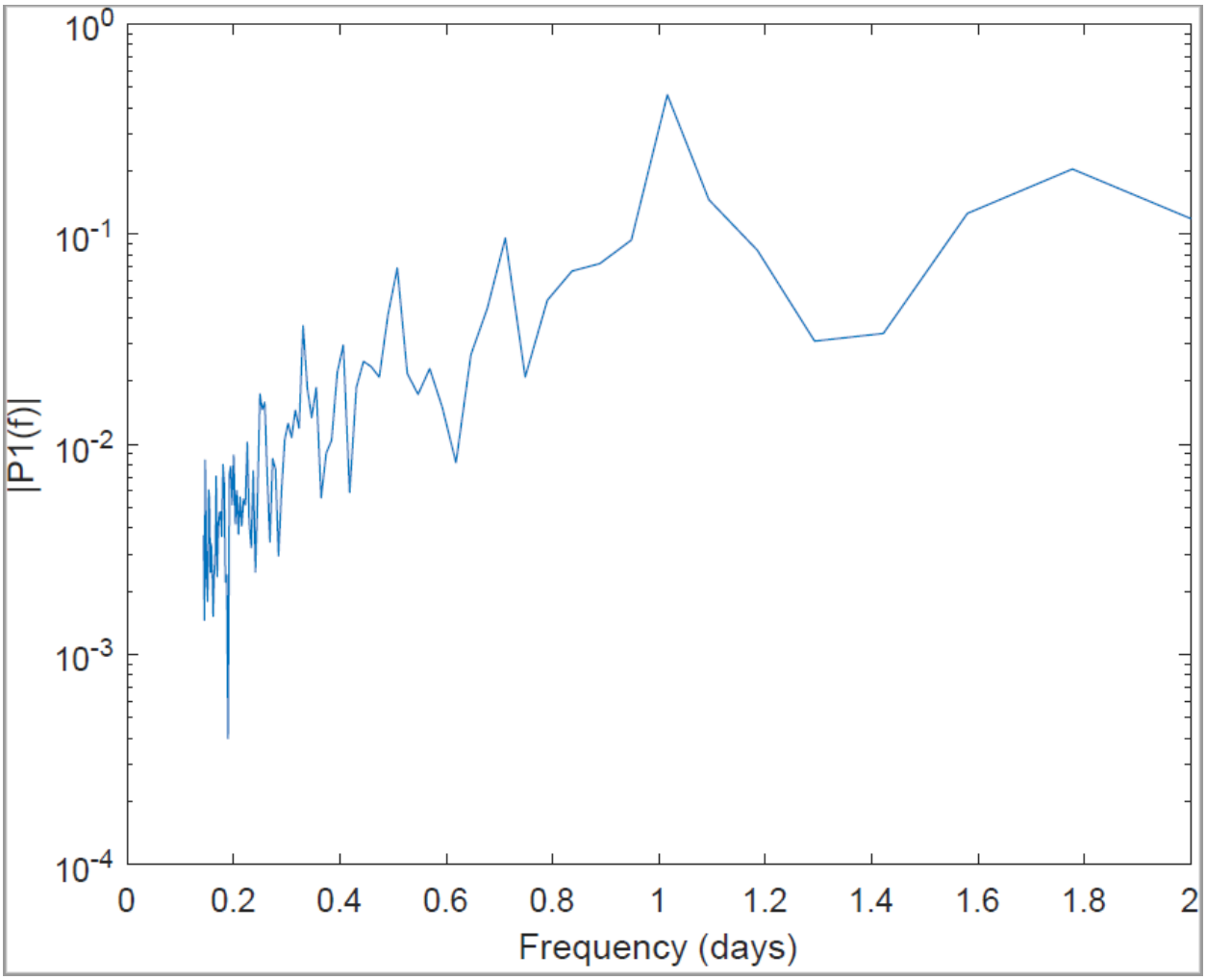

Figure C 1: FFT analysis of horizontal displacement at bearing J2-E from August 28, 2019 to August 28, 2020

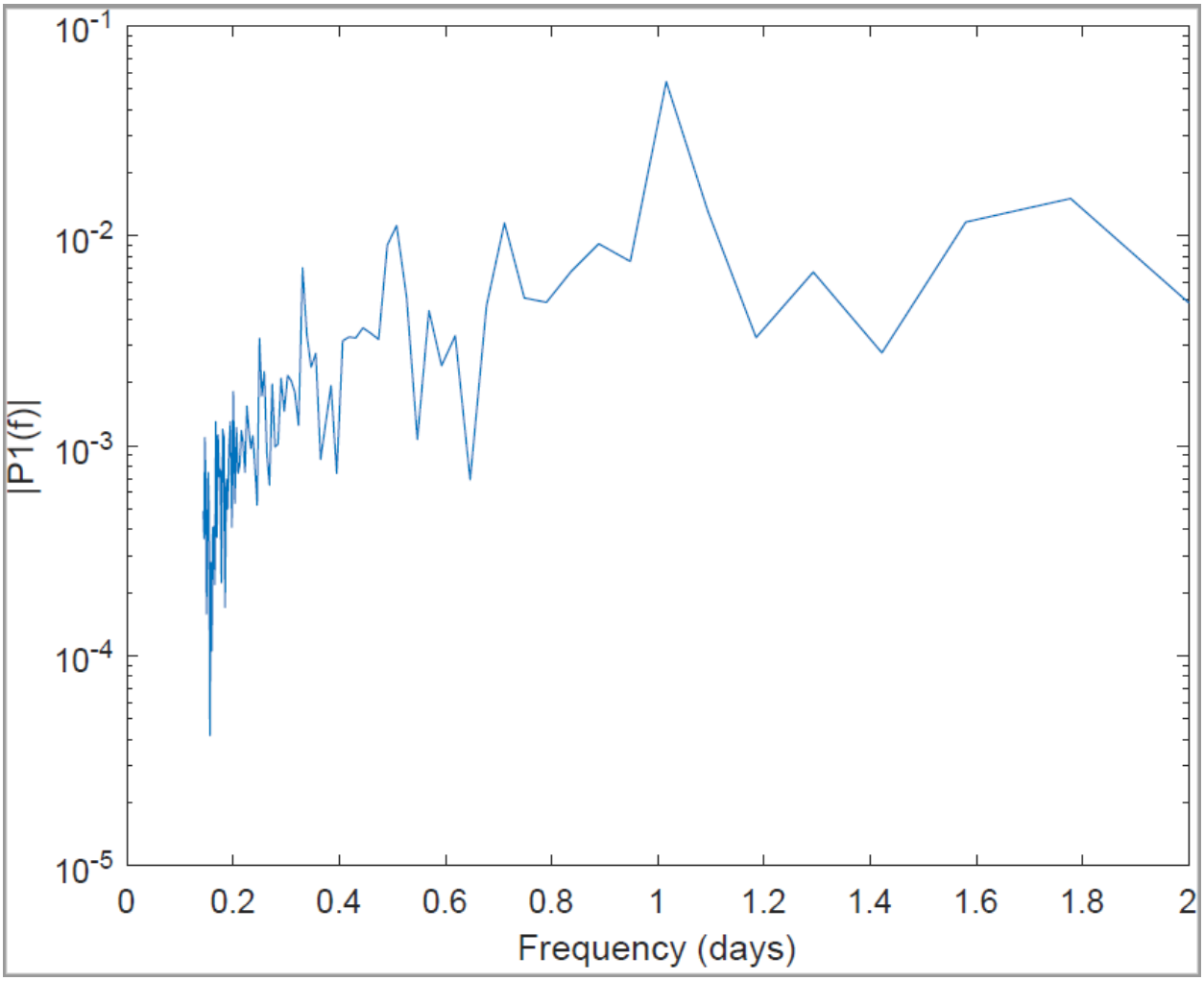

Figure C 2: FFT analysis of vertical displacement at bearing J2-E from August 28, 2019 to August 28, 2020

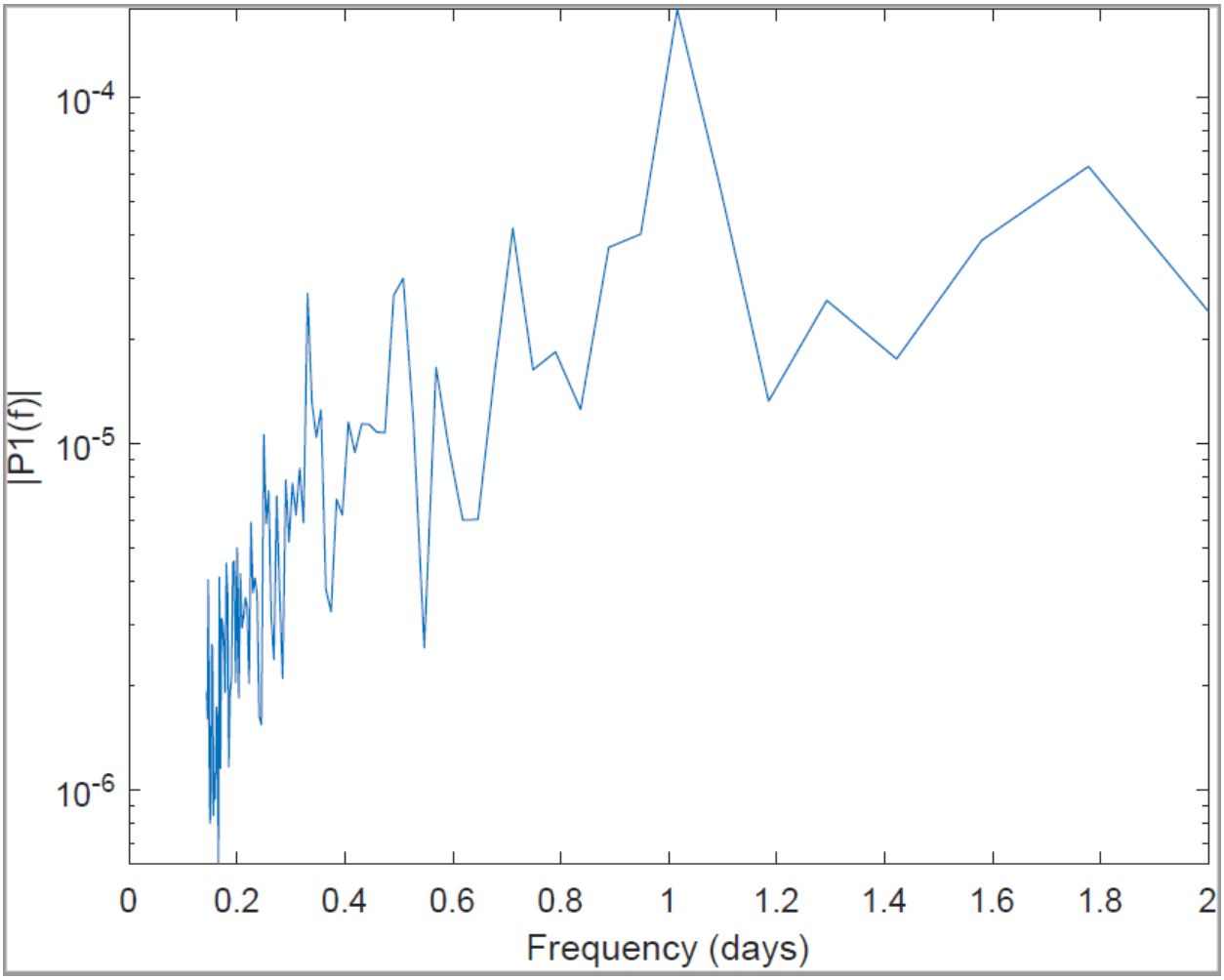

Figure C 3: FFT analysis of average rotation at bearing J2-E from August 28, 2019 to August 28, 2020

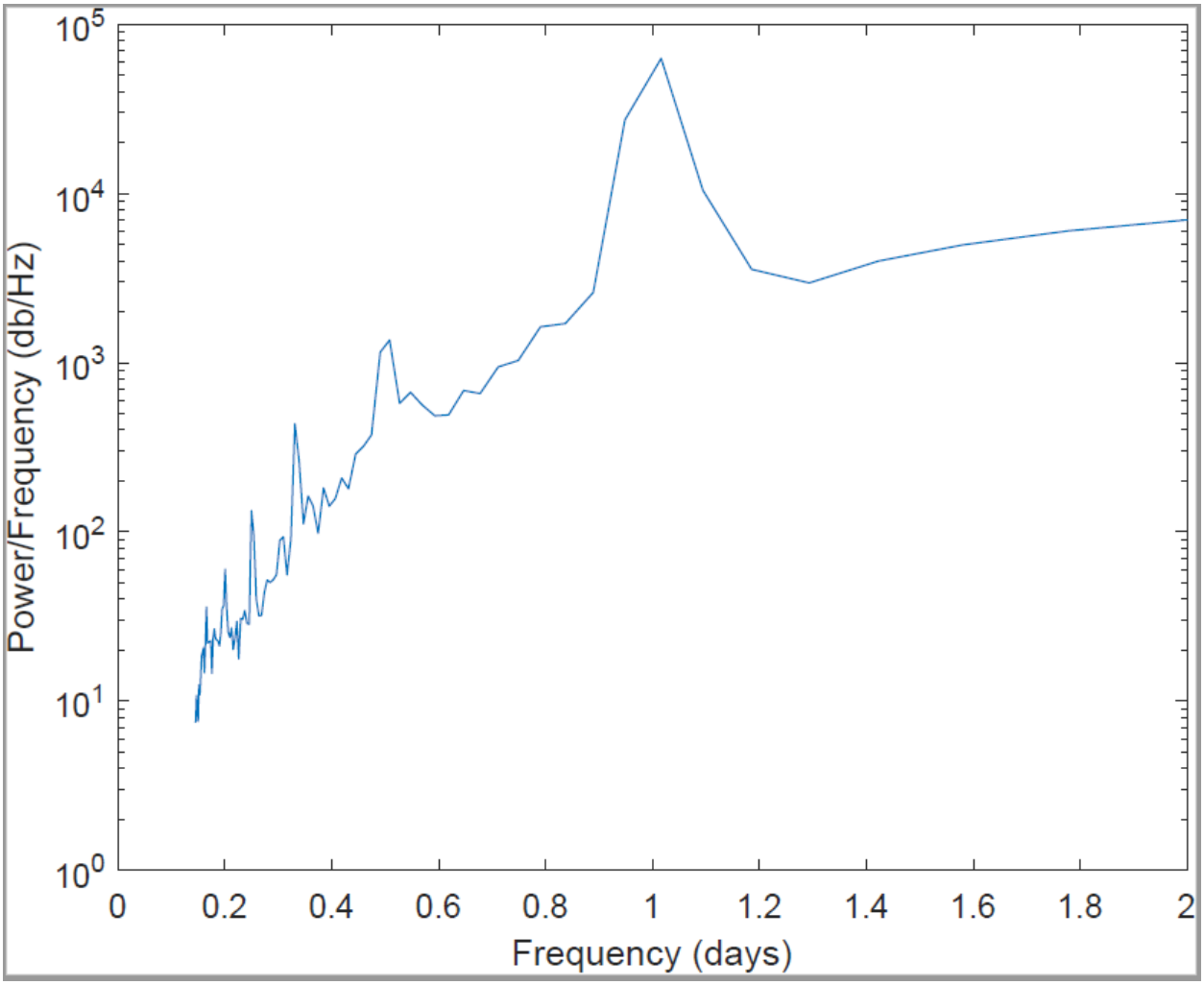

Figure C 4: PSD analysis of horizontal displacement at bearing J2-E from August 28, 2019 to August 28, 2020

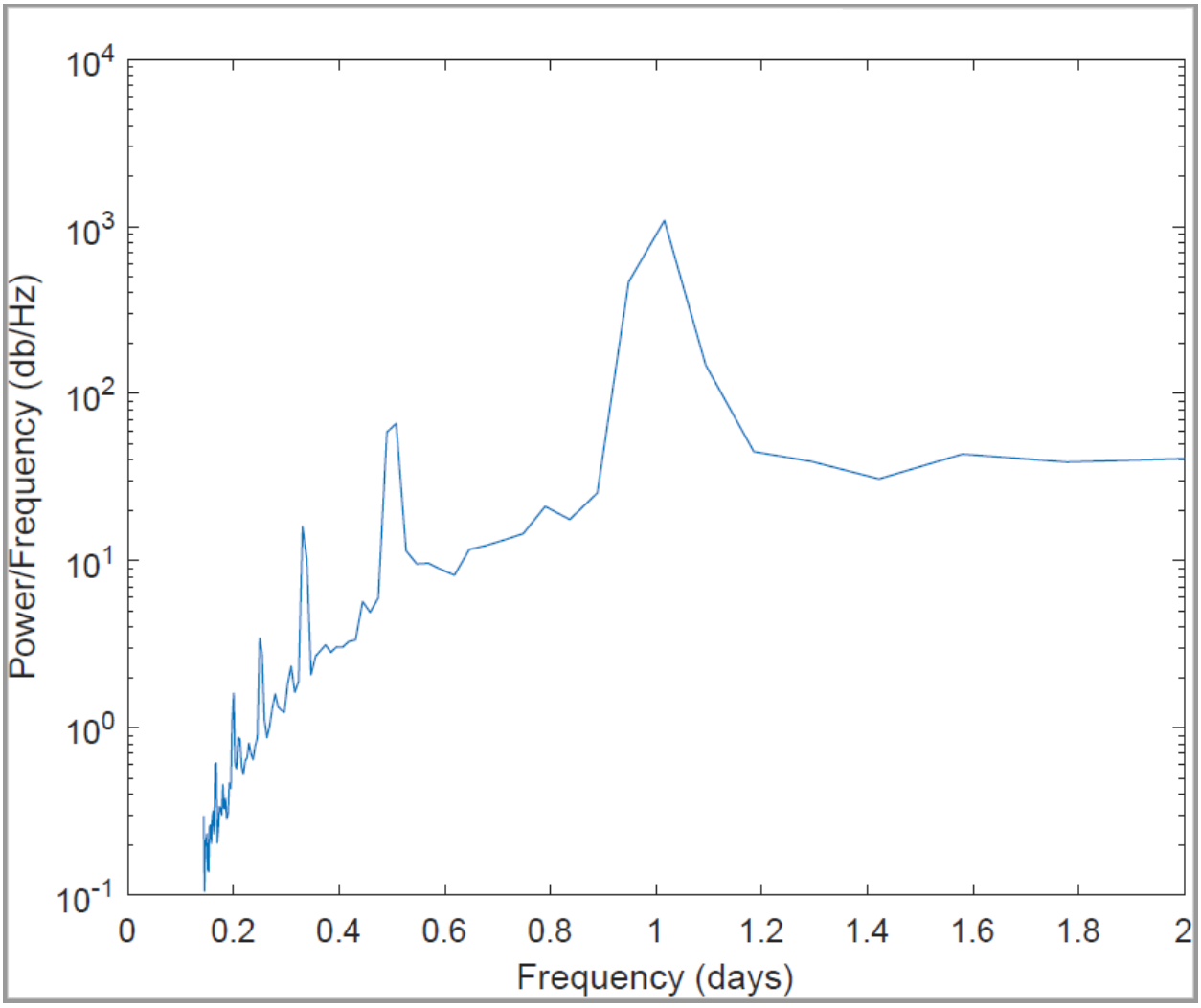

Figure C 5: PSD analysis of vertical displacement at bearing J2-E from August 28, 2019 to August 28, 2020

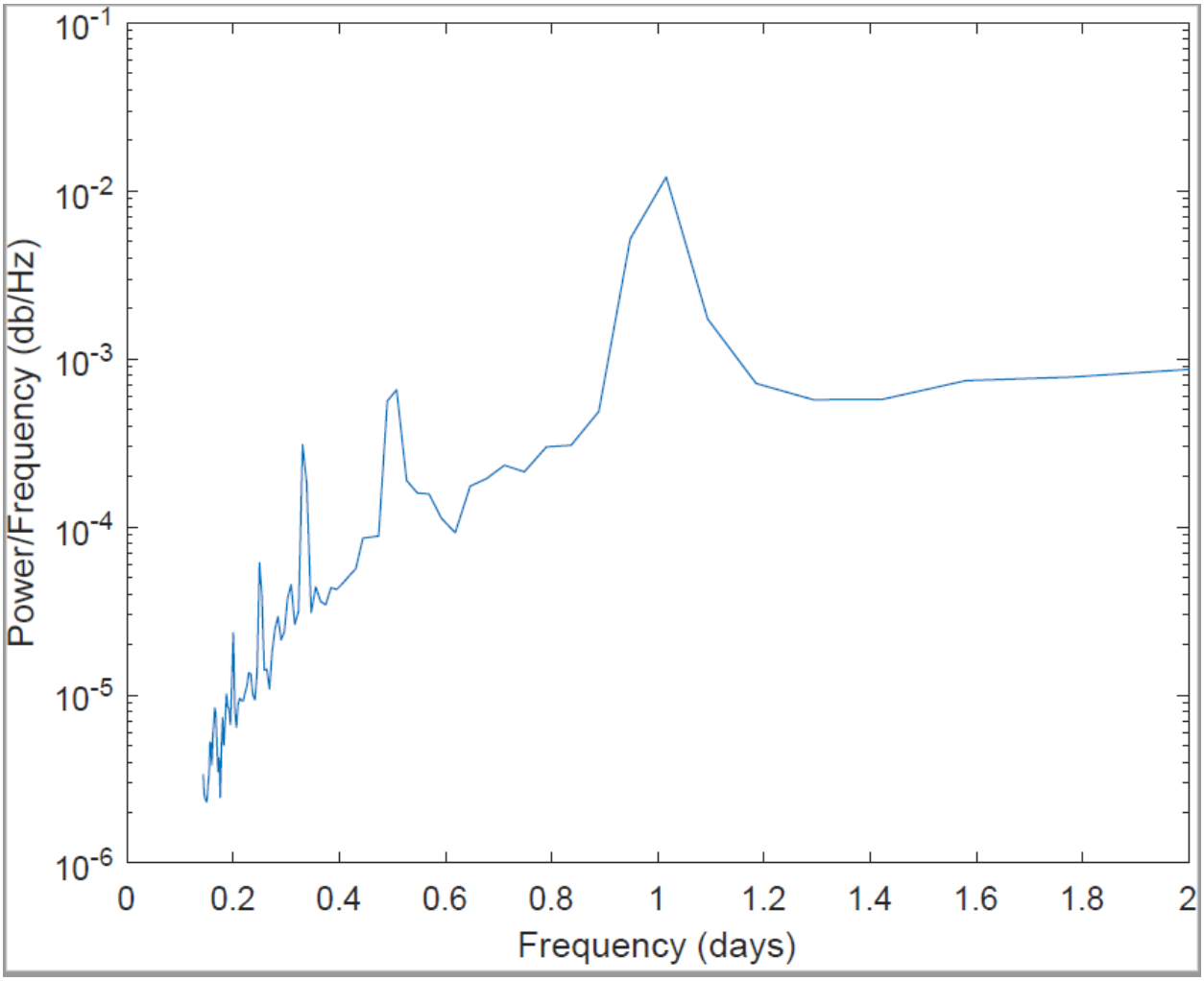

Figure C 6: PSD analysis of average rotation at bearing J2-E from August 28, 2019 to August 28, 2020